

Diss. ETH No. 21324

**ON-BOARD HYDROCARBON FUEL
PROCESSING FOR PORTABLE
SOLID OXIDE FUEL CELL POWER PLANTS**

A dissertation submitted to
ETH ZURICH

for the degree of
DOCTOR OF SCIENCES

presented by
ALEJANDRO JAVIER SANTIS ALVAREZ

Dipl. Ing. Technical Chemistry,
Graz University of Technology

born February 16, 1983
citizen of Guatemala

accepted on the recommendation of

Prof. Dr. Dimos Poulikakos, examiner
Prof. Dr. Paul Muralt, co-examiner

2013

Abstract

The present thesis addresses experimental fundamental investigations of partial and total hydrocarbon oxidation reactions for their implementation in **gas processing units** in low and intermediate temperature (350–700°C) micro-solid oxide fuel cell (SOFC) based systems (micro-power plants). Such systems are composed of three main components: a gas reforming unit, planar SOFC membranes, classically composed of anode, electrolyte and cathode, and a combustion unit for exhaust gas treatment. In this work, the fuel feed for fuel cells, i.e. the gas reforming unit, and exhaust treatment unit are subject to detailed investigation.

System requirements, an exothermic reaction behavior and simplicity in system integration justify the choice of **catalytic partial oxidation** (CPO) as gas reforming process, where apart from the fuel only air is needed for the chemical reaction. The production of syngas is investigated in a tubular reactor by using supported rhodium (Rh) nanoparticles synthesized by flame spray pyrolysis (FSP). For catalyst characterization, methane is chosen as fuel owing to its highest chemical stability of all low-chained hydrocarbons. Since Rh is a scarce and thus expensive metal, its effective usage is of vital importance in terms of cost reduction. Therefore, Rh was tested on two supports with different intrinsic characteristics, i.e. Al_2O_3 and $\text{Ce}_{0.5}\text{Zr}_{0.5}\text{O}_2$. It is demonstrated that Rh on Al_2O_3 shows significantly higher CPO yield than on $\text{Ce}_{0.5}\text{Zr}_{0.5}\text{O}_2$, especially at high oxygen concentrations at the reactor inlet and after sintering. Nonetheless, Rh supported on $\text{Ce}_{0.5}\text{Zr}_{0.5}\text{O}_2$ shows higher activity at lower temperatures and thus earlier activation of reaction, which is a major requirement for a fast and efficient SOFC based system start-up.

The advantage of syngas production for fuel cells in **external micro-reactors** lies in a considerably more efficient and precise optimization of the fuel-processing unit, leading to an enhanced overall efficiency of the system. For this purpose, a planar and compact micro-reactor filled with a foam-like, Rh/ $\text{Ce}_{0.5}\text{Zr}_{0.5}\text{O}_2$ based catalytic bed is introduced in this thesis. The size, geometry and testing modes are adapted to the demands for micro-SOFC based devices. The flow rate, required heating for reaction start-up and operation with or without an external heat source are shown to have a direct impact on CPO performance for $\text{Ce}_{0.5}\text{Zr}_{0.5}\text{O}_2$ supported Rh and overall energy consumption of micro-reactors. Significant emphasis is given to the

exothermicity of the CPO reaction, which would consequently allow the system to work in a self-sustained mode, i.e. without an external heating source. **Thermal self-sustainability of the reforming process** is achieved by the use of n-butane as fuel, which has high energy content as well as low vapor pressure and allows an easy refill in miniature portable cartridges. The results show that the self-sustained mode is the most effective operation mode for the CPO in micro-reactors. The micro-fabricated reactor itself demonstrates high fuel conversion and syngas yield and is well suited for applications in micro-SOFC based power plants.

Fuel utilization by means of electrochemical oxidation in fuel cells is less than 100%. Taking the aspect of environmental sustainability into account, unused toxic and flammable gas must be subjected to an **exhaust gas treatment** after the fuel cell unit. In order to make operation possible at intermediate temperatures, palladium (Pd) is tested on the mixed support $\text{Al}_2\text{O}_3\text{-Ce}_{0.5}\text{Zr}_{0.5}\text{O}_2$. More specifically, Pd metal is deposited selectively on either Al_2O_3 or $\text{Ce}_{0.5}\text{Zr}_{0.5}\text{O}_2$ in the mixed support $\text{Al}_2\text{O}_3\text{-Ce}_{0.5}\text{Zr}_{0.5}\text{O}_2$ by means of a two-nozzle FSP setup and its catalytic performance is compared to Pd on pure supports Al_2O_3 or $\text{Ce}_{0.5}\text{Zr}_{0.5}\text{O}_2$. The performance of the catalysts was dependent on the position of Pd on the supports, which strongly affected the oxidation state of the noble metal. It is shown that presence of Al_2O_3 in the support is beneficial for high activity at low temperatures. Also, Pd deposited selectively on Al_2O_3 in the mixed $\text{Al}_2\text{O}_3\text{-Ce}_{0.5}\text{Zr}_{0.5}\text{O}_2$ support is the catalyst system of choice for an efficient and long term catalytic activity in an exhaust gas treatment unit at moderate temperatures between 400 and 600°C.

Overall, the present dissertation makes a substantial contribution toward the realization and implementation of gas processing units in micro-SOFC-based devices. The significant impact of support materials in effective catalyst utilization in nanoparticles, the efficient implementation of the CPO reaction process in micro-reactors and the impact of selective deposition of metals on mixed substrate systems bring a novel perspective to the field of oxidative catalysis of low-chained, saturated hydrocarbons.

Zusammenfassung

In der vorliegenden Arbeit werden die partiellen und totalen Oxidationsreaktionen von Kohlenwasserstoffen, sowie ihr Einsatz in **Gasumwandlungseinheiten** in miniaturisierten Systemen basierend auf Tief- und Mitteltemperatur-Festoxidbrennstoffzellen (SOFC) ($350\text{--}700^\circ\text{C}$) experimentell untersucht. Solche Systeme bestehen aus drei Hauptkomponenten: einer Gasreformiereinheit, planaren SOFC-Membranen, bestehend aus Anode, Elektrolyt und Kathode, und einer Reinigungseinheit zur Behandlung von Abgasen. In dieser Arbeit stellen der Brennstoffzufuhr für die SOFC, d.h. die Reformiereinheit, sowie die Abgasreinigungseinheit die zentralen Punkte dar und werden entsprechend ausführlich untersucht.

Die Systemanforderungen, das exothermische Reaktionsverhalten und die einfache Integration ins System rechtfertigen die Wahl der **katalytischen partiellen Oxidation** (KPO) als Brennstoffreformierprozess, bei welcher neben dem Brennstoff nur Luft erforderlich ist. Die Produktion von Synthesegas wird in einem Rohrreaktor mit Hilfe von Rhodium (Rh)-Nanopartikeln analysiert, die in einer Flammen Spray Pyrolyse (FSP) hergestellt wurden. Methan wird aufgrund seiner vergleichsmässig hohen chemischen Stabilität unter den Kohlenwasserstoffen zur Charakterisierung der Nanopartikeln verwendet. Da Rh ein seltenes und deshalb teures Metall ist, ist dessen wirksamer Einsatz sehr wichtig um Kosten herabzusetzen. Aus diesem Grund wird Rh auf zwei Trägermaterialien mit unterschiedlichen Eigenschaften, Al_2O_3 und $\text{Ce}_{0.5}\text{Zr}_{0.5}\text{O}_2$, untersucht. Es wird gezeigt, dass Rh auf Al_2O_3 eine wesentlich höhere katalytische Aktivität als auf $\text{Ce}_{0.5}\text{Zr}_{0.5}\text{O}_2$ aufweist, vor allem bei hohen Sauerstoffkonzentrationen am Reaktoreingang und nach einem Sinterungsprozess. Nichtsdestotrotz weist Rh auf $\text{Ce}_{0.5}\text{Zr}_{0.5}\text{O}_2$ eine höhere Aktivität bei niedrigeren Temperaturen auf, was einen früheren Reaktionsstart ermöglicht, welcher eine Hauptanforderung für einen schnellen und effizienten Anlauf eines SOFC-basierenden Systems ist.

Der Vorteil der Synthesegasproduktion in einem **externen Mikroreaktor** für SOFC liegt in der effizienteren und genaueren Optimierung des Brennstoffreformierprozesses, was zu einer höheren Systemeffizienz führt. Zu diesem Zweck wird in der vorliegenden Arbeit ein planarer, kompakter Mikroreaktor vorgestellt, der mit einem aus $\text{Rh}/\text{Ce}_{0.5}\text{Zr}_{0.5}\text{O}_2$ bestehenden katalytischen schaumartigen Bett gefüllt ist. Die Grösse, Gestalt und

Charakterisierungsverfahren des Reaktors werden auf die Anforderungen von miniaturisierten SOFC-basierenden Systemen angepasst. Die verschiedenen Flussraten, das für den Reaktionsstart erforderliche Aufheizen sowie der Betrieb mit oder ohne externer Heizquelle haben einen direkten Einfluss auf die katalytische Leistung von $\text{Rh}/\text{Ce}_{0.5}\text{Zr}_{0.5}\text{O}_2$ für die partielle Oxidation sowie auf den Energieverbrauch des Mikroreaktors. Ein besonderes Augenmerk wird auf die Exothermie der KPO gelegt, welche dem System erlauben würde, in einer selbstanhaltenden Weise, d.h. ohne externe Heizquelle, zu arbeiten. Ein **thermisch-selbstanhaltender Reformierprozess** wird mit der Anwendung von n-Butangas erzielt, welches einen hohen Energiegehalt sowie einen niedrigen Dampfdruck aufweist und ein leichtes Nachfüllen in miniaturisierte, tragbare Patronen erlaubt. Die erzielten Ergebnisse zeigen, dass ein selbstanhaltender Reaktionsprozess der wirksamste Betriebsmodus für die KPO in Mikroreaktoren ist. Der mikrofabrizierte Reaktor selbst weist eine hohe Brennstoffumwandlung und Synthesegasausbeute auf und ist geeignet für den Einsatz in miniaturisierten SOFC-basierenden Systemen.

Der Verbrauch des Brennstoffes liegt bei dem in der SOFC ablaufenden elektrochemischen Prozess unter 100%. Aus Umweltverträglichkeitsgründen ist es notwendig die nach der SOFC-Einheit noch vorhandenen umweltschädlichen Gase einer **Abgasnachbehandlung** zu unterwerfen. Um den Betrieb bei verhältnismässig tiefen Temperaturen zu ermöglichen, wird Palladium (Pd) auf dem gemischten Trägermaterial $\text{Al}_2\text{O}_3\text{-Ce}_{0.5}\text{Zr}_{0.5}\text{O}_2$ eingesetzt. Genauer gesagt, Pd wird mit Hilfe einer zwei-FSP Einheit selektiv auf entweder Al_2O_3 oder $\text{Ce}_{0.5}\text{Zr}_{0.5}\text{O}_2$ im gemischten $\text{Al}_2\text{O}_3\text{-Ce}_{0.5}\text{Zr}_{0.5}\text{O}_2$ Trägermaterial präferentiell abgeschieden und dessen katalytische Aktivität mit der von Pd auf den reinen Trägermaterialien Al_2O_3 oder $\text{Ce}_{0.5}\text{Zr}_{0.5}\text{O}_2$ verglichen. Die katalytische Leistung von Pd zeigt eine Abhängigkeit von der Lage des Pd auf den Trägermaterialien, die einen starken Einfluss auf den Oxidationszustand des Edelmetalls aufwiesen. Es wird gezeigt, dass das Vorhandensein von Al_2O_3 im Trägermaterial für eine hohe Aktivität bei niedrigen Temperaturen von Vorteil ist. Ausserdem ist selektiv abgeschiedenes Pd auf Al_2O_3 im gemischten $\text{Al}_2\text{O}_3\text{-Ce}_{0.5}\text{Zr}_{0.5}\text{O}_2$ Trägermaterial das beste Katalysatorsystem für eine effiziente und langfristige katalytische Nachbehandlung von Abgasen bei Temperaturen zwischen 400 und 600°C.

Insgesamt leistet die vorliegende Dissertation einen wichtigen Beitrag zum Einsatz von Gasumwandlungseinheiten in miniaturisierten SOFC-

basierenden Systemen. Der signifikante Einfluss des Trägermaterials auf die Wirksamkeit des Katalysators in Nanopartikeln, der effiziente Einsatz des KPO-Reaktionsprozesses in Mikroreaktoren und der Einfluss der selektiven Abscheidung von Metallen auf gemischten Trägermaterialsystemen zeigen eine neue Perspektive im Bereich der oxidativen Katalyse kurzkettiger, gesättigter Kohlenwasserstoffe.

Acknowledgments

This PhD thesis would never have been possible without the help and support from many people.

First and foremost I want to express my gratitude to my advisor **Prof. Dimos Poulikakos** who gave me the opportunity to conduct this PhD thesis in his group. I would like to acknowledge him for the responsibility given to me within the multidisciplinary project ONEBAT. I am thankful for his guidance and support and his trust in me in my decisions, which allowed me to shape my research according to my interests. I profited and learned from his leadership at LTNT and the multidisciplinary research from the multifaceted group he built over the years.

I thank **Prof. Paul Muralt** from the Laboratory of Micro-engineering for Manufacturing at EPFL for accepting the task of a co-examiner and for the very useful and efficient collaboration with his research group.

I am deeply thankful to **Dr. Majid Nabavi**, who supervised this PhD thesis for more than two years and supported me scientifically and with practical guidance. I thank him for the introduction to the research topics and practical methods, fruitful discussions and also for his unlimited help to whatever problem occurred.

I am also greatly thankful to **Dr. Robert Büchel** of the Particle Technology Laboratory at ETH, who made a valuable contribution to this work during the last year of my PhD. I thank him for his valuable input and most of all unconditional support for working together. The collaboration with him helped me gain knowledge about the field of catalysis and nanoparticles.

Dr. Anja Bieberle-Hütter, the ONEBAT project leader, was a great guide during this last years. I greatly benefited from our discussions in our fields of research. I am deeply thankful to her for encouraging the interaction between the ONEBAT project contributors and thus for being a great example of a project leader.

Many thanks go to all the members of the Nonmetallic Inorganic Materials Institute at ETH and specifically to **Dr. Barbara Scherrer**, **Dr. Anna Evans**, **Dr. René Tölke**, and **Prof. Ludwig Gauckler** for their assistance and discussions in topics related to micro solid oxide fuel cells. **Dr. Michel Prestat**, also one of the ONEBAT project leaders, is gratefully acknowledged for our

discussions related to fuel cells and leadership shown when dealing with the testing of the micro-reactor–micro solid oxide fuel cell chip assembly.

Dr. Claude Muller and **Dr. Philippe Niedermann** from the Swiss Center for Electronics and Microtechnology were key persons in this project. Their effort in organizing meetings, keeping teams and co-workers informed as well as their guidance are gratefully acknowledged.

I acknowledge **Nora Hild** and **Prof. Wendelin Stark** from the Functional Materials Laboratory at ETH, whose collaboration was of great importance for this work. I thank them for the valuable suggestions and discussions, which lead to successful investigations in the present thesis.

Coming back to the field of solid oxide fuel cells, I would like to thank **Dr. Hironori Nakajima** from Kyushu University in Japan, with who I worked intensively during three months. His active support, explanations and most of all patience during our investigations is sincerely acknowledged.

The frequent meetings, discussions and collaboration carried out with **Bo Jiang** from the Laboratory of Micro-engineering for Manufacturing at EPFL were very fruitful and a key to the success of the present work. I am also very thankful to **Peter Heeb** and **Valentin Strässle** from the Interstaatliche Hochschule für Technik in Buchs SG for their input given to this work, the talks, new ideas and feedback provided during my thesis.

I highly appreciate the contribution of my master student **Yi Wang** and bachelor student **Patrick Rüdlinger**. I gained substantial knowledge from their successful and most of all unsuccessful experiments as well as their non-expected results.

I like to also sincerely thank **Jovo Vidic** for his technical support regarding my experimental setup and his friendship and **Dr. Frank Krumeich** from the Particle Technology Laboratory at ETH for his input regarding microscopy images.

I gratefully acknowledge the financial support by the **Swiss National Science Foundation** within the framework of the SINERGIA project "ONEBAT" (no. CRSI11_126830).

From the bottom of my heart, I would like to thank all members at the LTNT (you were my family during the last three years), all great **friends** outside ETH and my **family** for their support, encouragement, patience, guidance and most of all love. **Michaela Kanzian** (Lala), danke von ganzem Herzen für deine Liebe und Unterstützung.

Contents

Abstract.....	v
Acknowledgments.....	xi
1 Introduction.....	15
1.1 From high to intermediate temperature SOFC devices.....	15
1.2 Efficient partial oxidation reaction at low temperatures.....	19
1.3 Stabilization of exhaust gas treatment performance.....	22
1.4 Thesis Outline.....	23
2 A fast hybrid start-up process for thermally self-sustained catalytic n-butane reforming in micro-SOFC power plants.....	25
2.1 Introduction.....	26
2.2 Experimental methods.....	29
2.3 Results.....	34
2.4 Discussion.....	45
2.5 Conclusion.....	48
3 A nanoparticle bed micro-reactor with high syngas yield for moderate temperature micro-scale SOFC power plants.....	51
3.1 Introduction.....	52
3.3 Experimental methods.....	54
3.4 Results and discussion.....	58
3.5 Conclusion.....	71
4 A comparison of flame-made Al_2O_3 and $\text{Ce}_{0.5}\text{Zr}_{0.5}\text{O}_2$ supports on rhodium activity for the partial oxidation of methane.....	73
4.1 Introduction.....	73
4.2 Experimental methods.....	75
4.3 Results and discussion.....	77
4.4 Conclusion.....	92
5 The effect of deposition locality of flame-made Pd on a mixed Al_2O_3 - $\text{Ce}_{0.5}\text{Zr}_{0.5}\text{O}_2$ support on methane combustion.....	93
5.1 Introduction.....	93

5.2	Experimental methods	95
5.3	Results and discussion	97
5.4	Conclusion.....	110
6	Bibliography	111
	List of Publications.....	127
	Curriculum Vitae	129

1 Introduction

In recent years, the rapid increasing energy demand and cost has resulted in a growing need for alternative and more effective power generation sources in stationary as well as in portable applications. In view of this, miniaturized fuel cell power plants are becoming more attractive as an additional power source to more common batteries for portable applications. Compared to low temperature fuel cells, e.g. proton exchange membrane fuel cells (PEMFCs), solid oxide fuel cells (SOFCs) have the advantage of coupling high fuel flexibility with high efficiency and operate typically at temperatures above 800°C. A miniaturized SOFC system, such as the ONEBAT system in [1], can be composed of mainly three components: a partial oxidation unit, a planar micro-SOFC membranes unit and a combustion unit for exhaust gas treatment.

Accordingly, the focus and motivation of the present thesis lies in the development of high performance partial oxidation and combustion units by means of catalysis. For this purpose, flame-made catalytic nanoparticles consisting of supported active metals were investigated. The catalytic materials are chosen according to their thermophysical properties and intrinsic nature of the reaction in question.

In the following three sections, a short description is given about the components, composition, basic principles and properties of such catalytic systems. Starting with the operation principle of intermediate temperature (350°C–700°C) and small sized SOFC devices, the major demand of effective gas processing units and catalysts is underlined, which are extensively investigated in the present work.

1.1 From high to intermediate temperature SOFC devices

Fuel cells are the most efficient means to directly convert stored chemical energy to usable electrical energy by means of electrochemical reactions [2]. Additionally, fuel cells have the potential for both high efficiency and low emissions [3]. Whereas more common fuel cells e.g. proton-exchange membrane fuel cells (PEMFCs) require hydrogen as fuel, SOFCs use an oxygen-ion conducting electrolyte which essentially enables electrochemical

oxidation of any type of fuel that can be oxidized such as CO, H₂ and hydrocarbons [2]. In order to promote high oxygen ion mobility and low electrode resistances, SOFC usually operate at temperatures above 800°C. Significant research activity has been reported in literature with the aim of reducing operation temperature of SOFC systems [2,4-9]. In summary, operating temperatures can be essentially reduced to down to 350°C [2] by decreasing the thickness of the electrolyte in order to lower ohmic resistance and oxygen ion transport [9-12]. A reduction in operating temperature is desirable in light of various attractive SOFC applications such as micro-sized power generation for small-sized transportation systems or portable devices [13]. Some of the major benefits of low or intermediate operation temperature in SOFC systems are:

- The maximum theoretical efficiency defined as $\eta_{th} = \Delta G^0 / \Delta H^0$ increases with decreasing temperature, where ΔG^0 and ΔH^0 denote the change in Gibbs free energy and enthalpy, respectively. For example, considering CO as fuel, $\eta_{th} = 0.63$ at 900°C and 0.81 at 350°C [2].
- Lower temperatures enable faster start-up times since the time required to obtain operating temperature levels is minimized. Consequently, minimization of start-up times reduces energy costs, i.e. fuel consumption needed during activation of reaction (see chapter 3).
- Low temperature processes exhibit a lower degree of heat losses compared to high temperature operating systems and therefore, less insulation is needed. As a consequence, lower demand for insulation material reduces system size, weight and costs while increasing the energy density of the overall system.
- The hardware of the system e.g. interconnects and sealing can be built from a wider choice of materials. This advantage allows extended material lifetime and cost reduction.

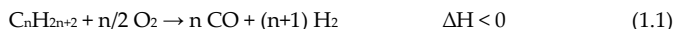
Low-chained hydrocarbons offer the advantage of high energy content per unit volume and the possibility of liquid fuel-refilling in storage tanks, which substitutes the problems associated with storage and distribution of hydrogen tanks for SOFC systems. Among hydrocarbons, n-C₄H₁₀ [1,14-16] and C₃H₈ [17] have been suggested as alternative fuels to power SOFC devices at temperatures between 500°C and 700°C. Their high energy density and low

vapor pressure are of great advantage for using them as fuel in such devices (Table 1.1).

Table 1.1: Lower heating value (LHV) per mole of fuel, energy density, vapor pressure and H₂ to carbon atom ratio for low-chained saturated hydrocarbons [18].

	H ₂ /C	Vapor pressure at 25°C [bar]	LHV [kJ mol ⁻¹]	LHV [J cm ⁻³]
CH ₄	2	NA	800	33013
C ₂ H ₆	1.5	45.0	1424	60774
C ₃ H ₈	1.33	9.3	1907	87153
n-C ₄ H ₁₀	1.25	2.4	2651	113385

Liquefied hydrocarbons can be used as fuel for SOFCs either by direct [19,20] or indirect reforming reaction [14-16]. In the first type, the gas is reformed directly in the anode compartment. Its simplicity in implementation in SOFC systems is without a doubt of great advantage in terms of engineering design. In the second type of system, the reformer is separated from the electrochemical component of the system. In this external compartment, hydrocarbon fuel is converted to more electrochemically active species e.g. H₂ and CO (syngas) by means of partial oxidation (equation 1.1).



From a thermodynamic perspective, direct utilization of hydrocarbons is more efficient in terms of current generation than indirect reforming [21] (equations 1.2-1.7). However, upon direct hydrocarbon operation at the anode, it has been shown that it is difficult to completely prevent carbonaceous deposition which deteriorates cell performance [21-23]. On the other hand, CO and H₂ rich gas produced from an external reforming unit can theoretically generate higher potentials at lower temperatures than pure hydrocarbons like methane, C₃H₈ and n-C₄H₁₀ (Figure 1.1). In the following, the differences between direct and indirect utilization is described.

The direct or internal electrochemical oxidation reaction for methane is given as



Electrochemical oxidation for methane as indirect or external partial oxidation can be written as

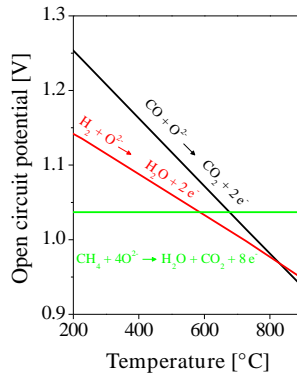
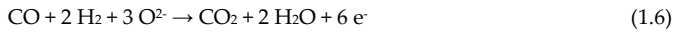
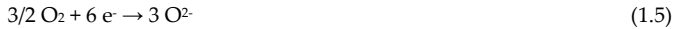


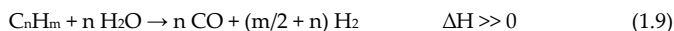
Figure 1.1: Electrochemical potential, $\Delta E = -\Delta G^0/(z \cdot F)$ as a function of temperature for different fuels.

By comparing both electrochemical pathways given in equations 1.2-1.7, the number of interacting electrons (z in equation 1.8) after external partial oxidation is decreased by 25% compared to direct electrochemical oxidation i.e. 6e^- vs. 8e^- , respectively. According to equation 1.8, current efficiency is

reduced accordingly. Here, I , \dot{n} and F denote the current, the molar flow rate of the fuel and the Faraday constant, respectively.

$$I = \dot{n} \cdot z \cdot F \quad (1.8)$$

Recently, intensive investigations of anode materials have been conducted with the aim of suppressing carbon formation on the anode [22,23], but further research is still needed for a reliable implementation in SOFC systems. The build-up of carbon on anode material can be simply circumvented by humidifying the hydrocarbon fuel stream with water. Therefore, direct reforming is generally achieved by means of the steam reforming reaction (equation 1.9), where water acts as a co-adduct of the reaction, thus enabling high H_2 production [24,25]. Apart from this, there are also benefits associated with incorporating some oxygen (or air) in the fuel stream of SOFCs, causing internal partial oxidation [26,27].



1.2 Efficient partial oxidation reaction at low temperatures

The partial oxidation in an external reforming unit has been the reaction and system of choice in the present thesis because of several reasons:

- The partial oxidation reaction is a mildly exothermic process with high reaction rates.
- The heat generated from the exothermic reaction allows both a rapid start-up and a thermal self-sustainability (self-sufficient temperature control) of the system (see chapters 3 and 4).
- Despite higher theoretical mole fractions of CO and H_2 from the steam reforming reaction according to calculated equilibrium than from partial oxidation, i.e. higher electron flow from electrochemical oxidation, steam reforming demands high energy input due to its highly endothermic reaction kinetics.
- Partial oxidation in an external unit allows smaller reactor volumes and system size due to faster reaction rates and an enhanced heat transfer

compared to steam reforming [3]. Reduction in reactor size is required for intermediate temperature SOFC systems [1], especially for planar SOFCs.

- Additionally, the partial oxidation adds to overall simplicity, where only air is needed for its implementation.

In line with the above, temperatures as high as SOFC operating temperatures are necessary for the external reforming unit. In order to allow for high fuel conversions and syngas production at intermediate temperatures, the partial oxidation reaction is carried out by means of catalysis. Here, the overall reaction performance is subjected to thermodynamic equilibrium limitations. Figure 1.2 shows the gas composition from calculated thermodynamic equilibrium at different temperatures using stoichiometric methane dilution according to equation 1.1. In the intermediate temperature region between 400°C and 600°C, fuel conversions between 31% and 64% with H₂ yields between 12% and 45% are possible when methane is used as fuel. For butane, complete conversion of the fuel is possible from a thermodynamic perspective, and H₂ yields between 5% and 52% are possible (not shown in Figure 1.2).

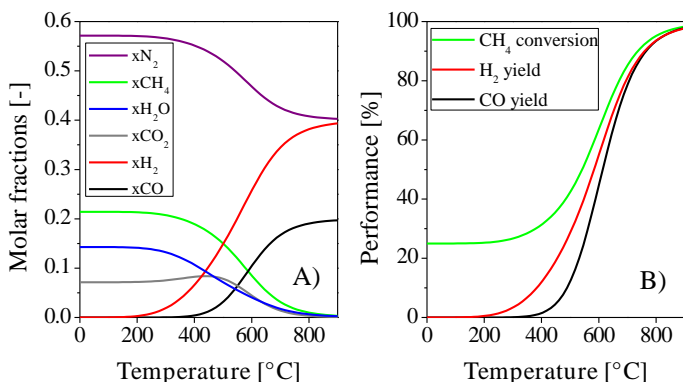


Figure 1.2: Thermodynamic equilibrium as a function of the temperature at 1 atm using CH₄/O₂ = 2.0 and air as oxidant. A) The mole fractions, x , of the components after reaction and B) the performance in terms of fuel utilization, H₂ and CO yield.

For the partial oxidation reaction, noble metals like Rh, Ru, Pt, Pd to name a few, have been investigated in literature [28,29]. Supported Rh has been shown to be the most active metal for low temperature catalytic partial oxidation (CPO) of hydrocarbons. However, Rh is a scarce metal and therefore its utilization effectiveness is of great importance for saving material and reducing costs. This topic is addressed in chapter 2 of the present thesis. Here, flame-made Rh nanoparticles are tested on two types of supports, Al_2O_3 and $\text{Ce}_{0.5}\text{Zr}_{0.5}\text{O}_2$, and its catalytic performance is compared to that calculated at equilibrium. It is shown that thermodynamic behavior can be obtained for Rh metal loadings ranging from 2 wt% to 5 wt% on these supports.

Coming back to the idea of portable power generation from an intermediate temperature micro-SOFC system, it is clear that a suitable design and adequate material choice for the partial oxidation reactor are vital when considering size reduction, thermal management, overall system efficiency and costs. When dealing with planar SOFC designs, a planar reactor geometry for the fuel processor is more convenient than common tubular reactor designs (see chapter 4). In previous studies conducted in our group, Hotz et al. [14] demonstrated the suitability of a disk-shaped micro-reactor for efficient n-butane to syngas conversion at a temperature of 550°C. The increase in cross sectional area along the radial flow direction leads to a significant increase in syngas production compared to tubular reactor geometry because of higher contact between gaseous reactants and solid catalytic material. In their study, the catalytic bed consisted of loose nanoparticles. Obviously, because of this fact, such type of catalytic bed cannot be taken into consideration for SOFC systems because of possible nanoparticle leakage to other system components but also potential environmental and health-related issues provoked by nanoparticles directly.

In this thesis, the reactor design, catalytic bed stability and reliability are adapted to individual system requirements. As such, a novel compact and planar micro-reactor is implemented and fabricated by standard micro-fabrication procedures. The challenge of avoiding loose nanoparticles in the catalytic bed is solved by filling the micro-reactor with a foam-like catalytic bed as introduced in [30]. In the subsequent micro-reactor characterization, two different heating modes, the continuous heating mode and the thermally self-sustained mode, are considered to evaluate operation conditions and micro-reactor performance.

1.3 Stabilization of exhaust gas treatment performance

After passing the partial oxidation unit, a mixture of oxidizable and inert components, i.e. C_nH_{2n+2} , CH_4 , H_2 , CO in H_2O , CO_2 and N_2 , flow through the anodic electrodes of the micro-SOFC membranes for electrochemical oxidation and power generation. Figure 1.3 shows the typical I-V (current-voltage) curve of a fuel cell. In this graph, the potential, power density and fuel utilization are given as a function of the current density of the system. According to equation 1.8, current density is maximized for high n values. At maximum power densities, where the fuel cell operates most efficiently, fuel utilization shows less than 100% resulting in unused fuel exiting the cell.

However, some of the exhaust gases are detrimental to environment and health. For example, CO is toxic, H_2 is highly flammable and CH_4 is a 20 times more efficient greenhouse gas than CO_2 [31]. Consequently, SOFC systems should be subjected to exhaust gas treatment in an external post-combustion unit.

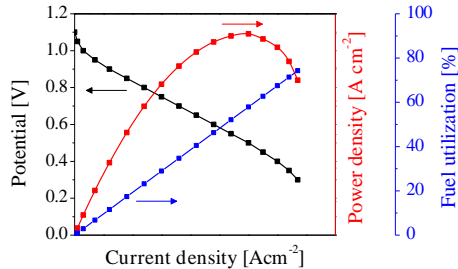


Figure 1.3: Example of a typical fuel cell polarization curve. The values for fuel utilization vary depending on testing conditions e.g. temperature, flow rate, material choice to name a few.

From the available fuels in the gas mixture CO and H_2 are the most active towards electrochemical oxidation, whereas C_nH_{2n+2} and CH_4 are more stable due to strong C-H bonds. As a result, the exhaust gas is expected to have primarily highly diluted C_nH_{2n+2} and CH_4 in inert gases. Between CH_4 and C_nH_{2n+2} , CH_4 is the more stable hydrocarbon and thus the limiting factor for efficient and complete fuel oxidation in our SOFC-system. Therefore, chapter 5 focuses on oxidation of CH_4 under lean conditions.

At temperatures above 1300°C, efficient homogenous oxidation of methane is possible. However, in order to allow the exhaust unit to operate at the same temperatures as the overall SOFC system (350°C–700°C), the use of a catalyst is essential. Among all metals, palladium has shown to be the most active metal for oxidation of methane under lean conditions at low temperatures [32,33]. So far, the stabilization in performance over time is one of the drawbacks for Pd-based catalysts and still remains one of the biggest challenges in the field of catalysis [32,34]. The activity of Pd based catalysts on the mixed support $\text{Al}_2\text{O}_3\text{-Ce}_{0.5}\text{Zr}_{0.5}\text{O}_2$ as well as their stability over time at constant temperature between 450°C and 530°C are addressed herein.

1.4 Thesis Outline

The outline of the thesis is given in the following. Chapters 2, 3 and 4 focus on the fuel partial oxidation process and chapter 5 describes the post-combustion process.

First, the concept of thermal self-sustainability of the partial oxidation reaction with n-butane as fuel is introduced in **chapter 2** and investigated in terms of start-up time and energy consumption during start-up as well as gas composition under operating conditions. The hybrid start-up method used for reaction activation consists of an electrical (resistive heating) and a chemical (exothermic reaction) heat generating component.

Subsequently, a compact catalytic micro-fabricated reactor is introduced in **chapter 3** and tested for n-butane and propane as fuel for the partial oxidation reaction process. The performance of this novel nanoparticle bed micro-reactor is shown to be highly dependent on the testing mode chosen: 1) continuous heating mode and 2) thermally self-sustained mode.

The catalytic partial oxidation of methane has been a highly investigated field of research in the last century and activity over noble metals has been investigated on many support systems with the aim of improving reaction efficiency and effective usage of noble metal. In **chapter 4** of this thesis, Rh is investigated on two different supports i.e. Al_2O_3 and $\text{Ce}_{0.5}\text{Zr}_{0.5}\text{O}_2$ with the aim of increasing reaction effectiveness and reducing usage of scarce and highly active noble metal.

In the **final chapter**, supported palladium nanoparticles are investigated in terms of catalytic oxidation of methane under lean burn conditions, similar to those expected for exhaust gas treatment of micro-SOFC systems like the

one presented in this thesis. This chapter describes the influence of Al_2O_3 and $\text{Ce}_{0.5}\text{Zr}_{0.5}\text{O}_2$ supports on Pd activity and stability for the CH_4 combustion reaction in mixed support $\text{Al}_2\text{O}_3\text{-Ce}_{0.5}\text{Zr}_{0.5}\text{O}_2$. By varying operation temperatures between 200°C and 900°C , the behavior of such catalytic systems is compared to that of Pd on pure Al_2O_3 and $\text{Ce}_{0.5}\text{Zr}_{0.5}\text{O}_2$ supports.

2 A fast hybrid start-up process for thermally self-sustained catalytic n-butane reforming in micro-SOFC power plants

Parts of this chapter are published in:

A. J. Santis-Alvarez, M. Nabavi, N. Hild, D. Poulikakos, and W. J. Stark, "A fast hybrid start-up process for thermally self-sustained catalytic n-butane reforming in micro-SOFC power plants," *Energy & Environmental Science*, vol. 4, pp. 3041-3050, 2011.

Abstract

This work aims at the investigation and optimization of a hybrid start-up process for a self-sustained reactor for n-butane to syngas conversion in intermediate temperature, micro-solid oxide fuel cell (micro-SOFC) power plants. The catalytic reaction is carried out in the presence of Rh-doped $\text{Ce}_{0.5}\text{Zr}_{0.5}\text{O}_2$ nanoparticles in a disk-shaped reactor. For the start-up, a resistance heater is embedded inside the catalytic bed and is activated until the exothermic oxidative reaction is initiated. The self-sustained temperature and reforming performance are demonstrated to be highly dependent on the fuel to oxygen (C/O) ratio and the catalytic activity at different space times. It is shown that a C/O ratio of 0.8 is a very good choice in terms of achieved steady-state temperature, syngas yield and start-up time. At a reactor inlet temperature of 809°C for a C/O ratio of 0.8 and a space time as low as 8 ms, a syngas yield of 69.6% and a temperature of 529°C at the simulated micro-SOFC membrane are demonstrated. After only 15 s from ignition, a temperature of 600°C at the reactor inlet is reached. The hybrid start-up process is optimized with respect to a specific setup as an example, but is of general nature and utility to similar systems.

2.1 Introduction

Due to the increasing energy demand and cost, fuel cell power plants are becoming more attractive as an alternative power source [35]. With low emissions of pollutants, fuel cell power plants are less harmful to the environment than conventional energy sources e.g. fossil fuel and coal. Recently, significant interest has emerged for the development of micro-solid oxide fuel cell (micro-SOFC) and other fuel cell systems fueled with hydrocarbons for battery replacement in small portable devices [1,36,37]. Such systems combine the high energetic efficiency of fuel cells with the easy storage and high availability of hydrocarbon fuels. As representative example of such novel micro-scale system, is ONEBAT a micro-SOFC power plant capable of replacing conventional batteries for small portable electronic equipment [1]. A factor of two to four higher energy density, geographical independence and immediate charging are some advantages of this system over state-of-the-art Li-ion batteries. Some of the challenges for developing micro-SOFC devices are geometrical compactness [38], thin film electrode material preparation [39,40], fuel cell integration, fast start-up and self-sustainability at the small-scale.

The system layout of ONEBAT is shown schematically in Figure 2.1. The different components of the ONEBAT system are fuel cell membrane, gas processing unit consisting of micro-reformer and post-combustor, fuel tank, heat exchanger and an electrochemical capacitor for the start-up.

The main working principle of systems such as the ONEBAT is based on the on-board syngas ($\text{CO} + \text{H}_2$) generation from hydrocarbons on the anode membrane of the SOFC (internal reforming) [17,41-47] or in a separate reactor (external reforming) [1,14,16,48] to provide the fuel and heat required to sustain the SOFC at intermediate working temperatures ranging between 500°C and 700°C.

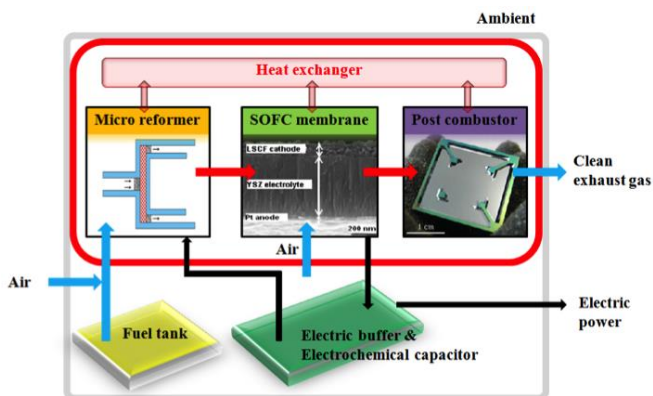
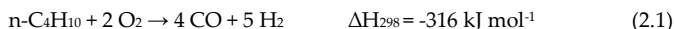


Figure 2.1: Layout of the ONEBAT system.

As an alternative fuel for micro-fuel cells, $n\text{-C}_4\text{H}_{10}$ has high energy density and can be easily refilled in miniature portable cartridges [36]. We have recently shown that a high syngas yield can be achieved by means of catalytic partial oxidation (CPO) of $n\text{-C}_4\text{H}_{10}$ on rhodium doped ceria-zirconia nanoparticles in small-scale reactors [14,30,48].

To achieve steady-state conditions, ignition of the exothermic partial oxidation (POX) reaction is necessary:



where ΔH_{298} is the standard enthalpy of reaction at 298 K [18]. The catalytic reaction ignition is often accomplished by heating the inlet gas feed or reactor with an oven or an external flame [14,30,48-51]. Seyed-Reihani et al. [16,52] focused their investigation on the influence of thermal conditions of insulated and non-insulated tubular reactors as well as the reactor length on the transient and steady-state behavior of CPO of $n\text{-C}_4\text{H}_{10}$ on rhodium-doped monolithic foams. For reaction ignition, the reactor and the gas feed were heated up by a furnace to $\geq 300^\circ\text{C}$. Additionally, prior reduction of the catalyst was required. Their experiments were performed on more than 10 times larger reactor volumes than in the present study. Furthermore, a simple and easy to implement start-up method should be developed since the use of a

furnace or similar heating devices cannot be implemented in real small-scale applications.

Schmidt and coworkers [53,54] achieved a fast lightoff using an ignition spark in a separate chamber, which activated the total oxidation (TOX) reaction:



In order to avoid any catalyst damage due to the very high temperature increase, the TOX ratio was switched to POX ratio after 5 to 15 s from ignition. The very fast heat release from the oxidation reaction makes this start-up process unsuitable for micro-SOFC systems.

Triggering of oxidative reforming of n-C₄H₁₀ was accomplished at ambient temperature over reduced CeO_{2-x} substrates doped with Ni- and Rh-catalysts by Sato and coworkers [55,56]. Here, H₂ was used as reducing agent, which makes it difficult to integrate the reformer into micro-systems due to complex H₂ purification from in-situ production and storage. The high temperatures required for the time consuming reduction process are among the disadvantages of this start-up system.

In a recent study conducted in our group, the hybrid start-up method for fast and energy efficient start-up for micro-SOFC systems was introduced [57]. In that study, the performance of platinum and rhodium as catalysts for TOX reaction of n-butane was investigated in an electrically heated tubular reactor. The final working temperature at steady-state, switching the TOX ratio to the POX ratio and the possible deactivation of the Rh-catalyst due to the very high temperatures produced by the TOX reaction were not investigated. The present study builds on the knowledge gained in [57].

The novelty of the present study is to implement a compact disk-shaped small reactor to achieve a thermally self-sustained CPO reaction using a hybrid start-up heating method in order to achieve intermediate operation temperature levels for micro-SOFC membranes ranging from 500°C to 550°C. Its button-shape makes this reactor suitable for a micro-SOFC system where geometrical compactness is of great importance [58]. The CPO reaction of n-butane is catalyzed by ceria-zirconia nanoparticles with a 2 wt% rhodium doping. In addition to their fast and easy one-step fabrication by flame spray pyrolysis, catalytic nanoparticles allow a low reactor volume which increases the compactness of the micro-SOFC portable system [59].

In the present study, optimization of high syngas production and steady-state operating temperatures are achieved by varying the gas flow rates and composition. The objective of the hybrid start-up method is to bring the micro-SOFC to its nominal temperature in a fast and energy efficient manner. We optimize the hybrid start-up process by varying the temperature level at which electrical heating is turned off (stop temperature, T_{stop}). The important factors in real applications including the start-up time and the required electrical energy are thoroughly investigated. In order to reduce unnecessary complexities, the post-combustion unit was not included in the setup.

The present study brings us a step closer to the goal of producing a very first self-sustained portable micro-SOFC power plant powered by external n-butane oxidative reforming.

2.2 Experimental methods

Catalyst preparation

The catalytic $\text{Ce}_{0.5}\text{Zr}_{0.5}\text{O}_2$ nanoparticles with 2.0 wt% Rh-doping were prepared in a one-step process by flame spray synthesis described in more detail in the previous studies [14,48,60,61]. As precursors for the $\text{Ce}_{0.5}\text{Zr}_{0.5}\text{O}_2$ substrate, cerium(III) 2-ethylhexanoate (13 wt% Ce, S.C. Soctech S.A.) and zirconium 2-ethylhexanoate (25 wt% Zr, ABCR GmbH & Co. KG) were mixed at metal molar ratio Ce/Zr of 1:1 and then diluted with xylene to a total metal concentration of $0.8 \text{ mol}\cdot\text{L}^{-1}$. Rhodium(III) 2-ethylhexanoate (UMICORE AG & Co.) was added to the Ce/Zr-precursor such that the calculated rhodium content in the ternary system Rh/ceria/zirconia ($\text{Rh}/\text{Ce}_{0.5}\text{Zr}_{0.5}\text{O}_2$) was 2.0 wt%.

Catalyst characterization

To determine the Rh-content in the catalyst, powders were dissolved in aqua Regia ($\text{HNO}_3 : \text{HCl} = 1:3$) and analyzed by inductively coupled plasma optical emission spectrometry (ICP-OES) (Ultima 2, Horiba Jobin Yvon S.A.S.). The specific surface area of the nanoparticles was measured by nitrogen adsorption utilizing a Tristar 3000 Micrometrics (Norcross, GA, USA). X-ray powder diffraction (XRD) patterns were collected on an X'Pert PRO-MPD (Cu $K\alpha$ radiation, X'Celerator linear detector system, step size of 0.033° , ambient

conditions). Transmission electron microscope pictures were recorded on a Tecnai F30 (FEI) with field emission gun operated at 300 kV.

Experimental apparatus

A sketch of the disk-shaped reactor used in this study is depicted in Figure 2.2. This radial flow small reactor has proven advantages compared to a tubular reactor at the same experimental conditions in terms of H_2 and CO yield as well as low pressure drop [14].

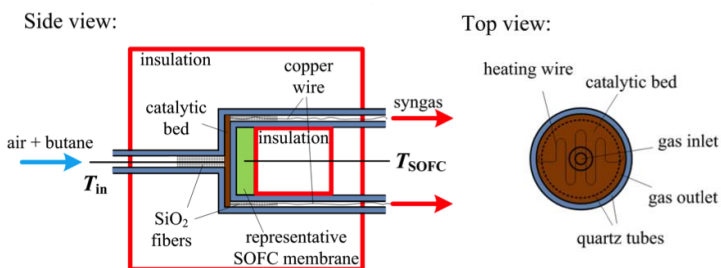


Figure 2.2: Schematic diagram of the reactor and the thermally representative micro-SOFC membrane.

The catalytic reactor bed consisted of 20 mg of Rh-doped $Ce_{0.5}Zr_{0.5}O_2$ nanoparticles and 60 mg of washed and calcined SiO_2 -sand (Riedel-deHaën, average diameter: 0.2 mm) with diameter and thickness of 10 mm and 1 mm, respectively. Glass wool fibers served as plugging and insulation material to prevent heat losses in axial direction at the gas inlet and outlet. The overall length and thickness of the walls were 10.0 cm and 1.0 mm, respectively. The inner quartz tube allowed for a radial distribution of the reactants from the inlet to the outlet ring of the catalytic bed. The thermal behavior of the fuel cell membrane was represented using a 2.0 mm thick SiO_2 -sand packed bed located just behind the 0.5 mm thick quartz glass wall of the inner tube.

A short heating wire (ferrite alloy, 73.2% Fe, 22.0% Cr, 4.8% Al, Kanthal D, diameter: 0.2 mm, length: 30 mm, Sandvik AB) was used to generate the heat required for triggering the exothermic reaction. The wire was bent several times to form a compact meander geometry, as shown in Figure 2.2, and was located at the backside of the reactor between the catalytic packed bed and the

glass wall of the inner tube. The heating wire was connected to a power source by two enameled copper wires (0.2 mm, Rowan Products Ltd.). The power source was controlled manually and turned off at the specified stop temperatures (T_{stop}).

The temperature profile during start-up and at steady-state conditions was recorded every 0.5 s at two different points using two K-type thermocouples as shown in Figure 2.2. The tip of one thermocouple (T_{in} , 250 μm thick) was placed at the inlet surface of the packed bed reactor whereas a second thermocouple (T_{SOFC} , 500 μm thick) was used to measure the temperature in the SiO_2 -packed bed.

The reactor was insulated by a cubical insulation block (WDS®Ultra, 7 cm \times 7 cm \times 7 cm, thermal conductivity = 0.018 $\text{Wm}^{-1}\text{K}^{-1}$ at 50°C varying to 0.031 $\text{Wm}^{-1}\text{K}^{-1}$ at 600°C, Porextherm Daemmstoffe GmbH). In addition, WDS®Ultra-powder was packed behind the SiO_2 -bed to form a 4 cm thick insulation layer to minimize heat loss from the thermally representative micro-SOFC membrane.

In the experiments, synthetic air (80 vol% N_2 , 20 vol% O_2 , PanGas, 5.6, 99.9996%) and $n\text{-C}_4\text{H}_{10}$ (PanGas, 3.5, 99.95%) were mixed at specified ratios at room temperature (30°C) before entering the reactor. The air and $n\text{-C}_4\text{H}_{10}$ gas flows were controlled by two flow controllers (Bronkhorst) with an accuracy of $\pm 0.1\%$ for synthetic air and $\pm 1.0\%$ for $n\text{-C}_4\text{H}_{10}$. These flow controllers allowed for operation of the reactor slightly above ambient pressure. The product gases leaving the reactor were maintained at around 115°C to avoid water condensation. All measurements were carried out under steady flow conditions and repeated at least twice.

An online automated gas chromatograph (GC) (6890 GC, with a HP-MOLSIV and a HP-PlotQ column, Agilent) was used to measure the sample effluent composition at steady-state after 30, 60 and 90 min from the beginning of the reaction. Helium (PanGas, 5.6, 99.9996%) was used as internal standard for GC calibration and as carrier gas for the product gases. The molar product gas balances for C, H and O atoms closed within 5%.

After 90 min of ignition, the reaction was terminated by simply stopping the $n\text{-C}_4\text{H}_{10}$ flow. The air flow was left open in order to cool down the reactor to room temperature.

Varying C/O ratio and flow rates

The inlet gas composition and flow rate were varied in order to identify the desired syngas yield at optimal intermediate operating temperature range of 500–550°C on the representative fuel cell membrane.

The ratio of n-C₄H₁₀ to O₂ is based on the stoichiometric POX reaction and reads

$$C / O = 2 \cdot \frac{\dot{n}_{C_4H_{10},in}}{\dot{n}_{O_2,in}} \quad (2.3)$$

The total inlet flow rates $V_{gas,in}$ for the different investigated C/O ratios were 150 standard cubic centimeters per minute (sccm), 170 sccm and 190 sccm. The space time t_{space} for the reactants in the catalytic bed is defined as

$$t_{space} = \frac{V_{reactor}}{V_{gas,reactor}} \quad (2.4)$$

where $V_{gas,reactor}$ is the volumetric flow of reactants in the reactor. This parameter follows the ideal gas law and is calculated using averaged temperatures between T_{in} and T_{SOFC} .

For reaction ignition, the reactor was electrically heated at a constant power of 6.75 W until T_{SOFC} reached 300°C under constant air/n-butane flow. This power was chosen according to [57]. At this high temperature level, the reaction ignition in the catalytic bed was ensured.

Varying the stop temperature

To better understand the influence of the applied energy input on the start-up time, the electrical heater was turned off at different temperature levels of the SiO₂-packed bed. One reference measurement was performed without any gas feed in order to test the influence of the heat released by the oxidation reactions on the hybrid start-up time. For this purpose, the heating meander was left on at the same constant power of 6.75 W until a steady temperature was achieved. The influence of all the materials used for the experiments (heating wire, Cu-wires, thermocouples and the quartz glass walls) on the gas effluent composition was also tested in an oven as described in [48] at temperatures ranging from 300–700°C. No meaningful influence was detected in this test.

Analysis

The experimental results were quantified using the following characteristic values:

The n-C₄H₁₀ conversion is defined as:

$$\eta = 1 - \frac{\dot{n}_{\text{C}_4\text{H}_{10},\text{out}}}{\dot{n}_{\text{C}_4\text{H}_{10},\text{in}}} \quad (2.5)$$

The yields of syngas (H₂ and CO) and TOX (H₂O and CO₂) species are defined as:

$$\psi_{\text{H}_2/\text{H}_2\text{O}} = \frac{\dot{n}_{\text{H}_2/\text{H}_2\text{O}}}{5 \cdot \dot{n}_{\text{C}_4\text{H}_{10},\text{in}}} \quad (2.6)$$

$$\psi_{\text{CO}/\text{CO}_2} = \frac{\dot{n}_{\text{CO}/\text{CO}_2}}{4 \cdot \dot{n}_{\text{C}_4\text{H}_{10},\text{in}}} \quad (2.7)$$

The yield of CH₄ is calculated as:

$$\psi_{\text{CH}_4} = \frac{2 \cdot \dot{n}_{\text{CH}_4,\text{out}}}{5 \cdot \dot{n}_{\text{C}_4\text{H}_{10},\text{in}}} \quad (2.8)$$

The selectivities for H₂ and CO read:

$$S_{\text{H}_2/\text{CO}} = \frac{\dot{n}_{\text{H}_2/\text{CO}}}{\dot{n}_{\text{H}_2/\text{CO}} + \dot{n}_{\text{H}_2\text{O}/\text{CO}_2}} \quad (2.9)$$

We define syngas yield as the maximum possible amount of partial oxidation according to (3.1) as:

$$\psi_{\text{syn}} = \frac{\dot{n}_{\text{H}_2} + \dot{n}_{\text{CO}}}{9 \cdot \dot{n}_{\text{C}_4\text{H}_{10},\text{in}}} \quad (2.10)$$

Also, yield of TOX reaction (3.2) is given as:

$$\psi_{\text{TOX}} = \frac{\dot{n}_{\text{H}_2\text{O}} + \dot{n}_{\text{CO}_2}}{9 \cdot \dot{n}_{\text{C}_4\text{H}_{10},\text{in}}} \quad (2.11)$$

2.3 Results

Catalyst characterization

The Rh-content of the as-prepared catalyst was measured with ICP-OES and is 1.9 wt%, which confirms a satisfactory low level of Rh-loss during synthesis. The average diameter is calculated as 12 nm using the Brunauer-Emmett-Teller (BET) method, which determined a specific surface area for the as-prepared nanoparticles of $76 \pm 1 \text{ m}^2\text{g}^{-1}$. The X-ray diffraction pattern of as-prepared catalyst depicted in Figure 2.3 is similar to XRDs obtained for $\text{Ce}_{0.5}\text{Zr}_{0.5}\text{O}_2$ in [48] and [60], and shows no additional reflection despite a 1.9 wt% Rh-doping.

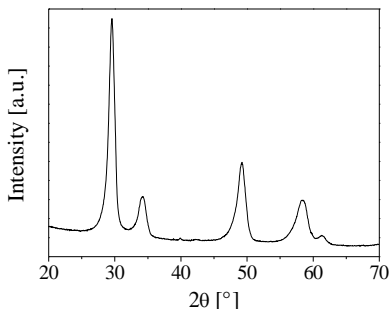


Figure 2.3: Powder X-ray diffraction pattern of flame-made 1.9 wt% Rh/ $\text{Ce}_{0.5}\text{Zr}_{0.5}\text{O}_2$ nanoparticles.

Figure 2.4 depicts the transmission electron micrographs of the as-prepared nanoparticles (Figure 2.4a and b) and of powder samples after measurements at the inlet (Figure 2.4c) and at the outlet of the reactor (Figure 2.4d). The figures show a narrow particle-size distribution and similar particle sizes as the one calculated using the BET method. Powders after measurements show slightly rounded corners compared to the well angular structures of the as-prepared catalyst. In addition, no carbon deposition can be seen on the used catalyst.

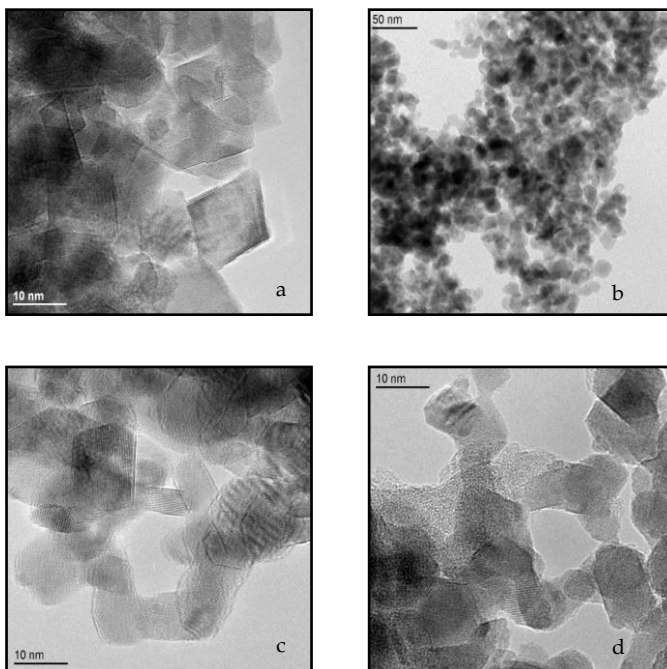


Figure 2.4: Transmission electron micrographs of as-prepared 1.9 wt% Rh/Ce_{0.5}Zr_{0.5}O₂ (a,b), and of used catalytic powders for which samples were taken at the inlet (c) and at the outlet of the reactor (d) after measurements.

Effect of the gas composition (C/O ratio) and the total inlet flow

The C/O ratio was varied between 1.0 and 0.7 in 0.1 steps, leading to molar fractions of $X_{C_4H_{10}} = 9.09\%$ to 6.54% , $X_{O_2} = 18.18\%$ to 18.69% and $X_{N_2} = 72.73\%$ to 74.77% for n-C₄H₁₀, O₂ and inert N₂, respectively. For reaction ignition, a power of 6.75 W by the power source was supplied until T_{SOFC} reached 300°C. From that point on, the heat released by the oxidative CPO reaction was sufficient to achieve self-sustainability. The variation of electrical power input during heat-up was below 4% for all experiments and negligible. This variation was due to the change in the heater resistance caused by the temperature change. Steady temperature conditions were achieved after 5–10

min of start at T_{in} , and after 10–15 min for T_{SOFC} . The delay of steady conditions was caused by the slow heat transfer from the back face of the catalytic reactor through the glass wall and the sand where the thermocouple was inserted.

The steady-state temperatures at the inlet of the catalytic bed (T_{in} , higher temperatures) and at the representative micro-SOFC membrane (T_{SOFC} , lower temperatures) versus C/O for different flow rates are depicted in Figure 2.5. The values of molar oxygen to fuel ratio (O/C ratio) corresponding to the different gas compositions are also plotted. A temperature difference between T_{in} and T_{SOFC} of as much as a few hundreds of degrees can be observed. The temperatures at the simulated micro-SOFC membrane ranging between the desired range of 500–550°C were obtained in only 5 cases (between the two horizontal lines in Figure 2.5). Nevertheless, for analysis and comparison purposes, all outlet gases are analyzed in terms of molar outlet flow rate, yield and selectivity values, since their relevance is important as higher temperature levels at other C/O ratios can be reached by only adjusting the inlet flow rates.

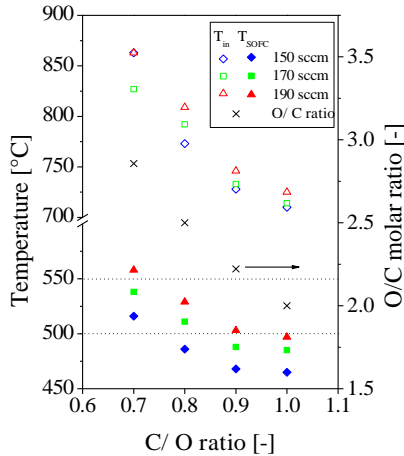


Figure 2.5: Steady-state temperatures at reactor inlet (T_{in} , empty symbols) and at the thermal representative micro-SOFC (T_{SOFC} , full symbols) after 90 min from reaction start along with the O/C molar ratio as a function of C/O ratio.

Figure 2.6 depicts the temperature profile for $C/O = 0.8$ at all investigated gas flow rates during 90 min from ignition, and Figure 2.6b shows the fast increase in T_{in} for $V_{gas,in} = 190$ sccm at different C/O ratios during the first 60 s after ignition of reaction. From these two figures it can be deduced that larger increase in temperature is achieved at higher flow rates i.e. more heat releases from the POX reaction and that a decrease of C/O ratio results in a faster start-up. A slight temperature decrease after turn-off of the electric heating at T_{stop} can be observed in Figure 2.6a (see section “Dependency on the stop temperature”) for T_{SOFC} . This is due to the higher amount of heat supplied by the heating wire compared to the heat of transient CPO reaction at the time when the heater is turned off.

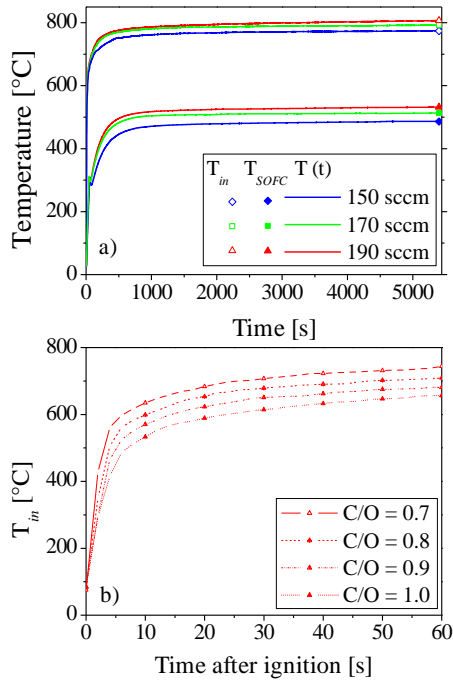


Figure 2.6: **a)** The temperature profiles for all flow rates investigated at $C/O = 0.8$ during 90 min of reaction. Empty and filled symbols show T_{in} and T_{SOFC} after 90 min of experiment. **b)** The first 60 s of the temperature profile at T_{in} after reaction ignition for all C/O ratios at $V_{gas,in} = 190$ sccm.

The results of the gas analysis at steady-state are shown in Figure 2.7 a-f. A total oxygen conversion is achieved for all experiments. The fuel conversion increases with increasing temperature and decreasing C/O ratio, reaching maximum level of 95.0% at C/O = 0.7 and $V_{\text{gas,in}} = 190$ sccm (Figure 2.7a). The yields of H₂, CO₂ and CH₄ are maximum at C/O = 0.7 (79.1%, 35.0% and 3.9%, respectively). The selectivity of H₂ and yield of CO increase by lowering the C/O ratio from 1.0 to 0.8 and reach a maximum at C/O = 0.8 for all investigated flow rates (Figure 2.7c and d). CO selectivity, on the other hand, shows decreasing monotonic behavior with minimum at C/O = 0.7 and maximum at C/O = 1.0. H₂ selectivity reaches values above 80% for all investigated conditions. As in the previous studies [14,30,48] no significant amounts of lower hydrocarbons can be detected in the product gas with the only exception of CH₄, with yields ranging between 1.1 and 3.9%. From all effluent species, only CO₂, H₂O gas and CH₄ yields decrease by decreasing t_{space} . Water vapor has its highest yield of 11% at C/O = 0.7. The molar fractions measured after 30 min and 60 min from reaction-start deviate $\pm 3\%$ depending on the species (-3% for n-butane conversion, -3% for H₂ yield, -2% for CO and +2% for CO₂, +3% for H₂O and +3% for CH₄). The results for all molar fractions measured for C/O = 0.8 after 90 min from reaction ignition are summarized in Table 2.1.

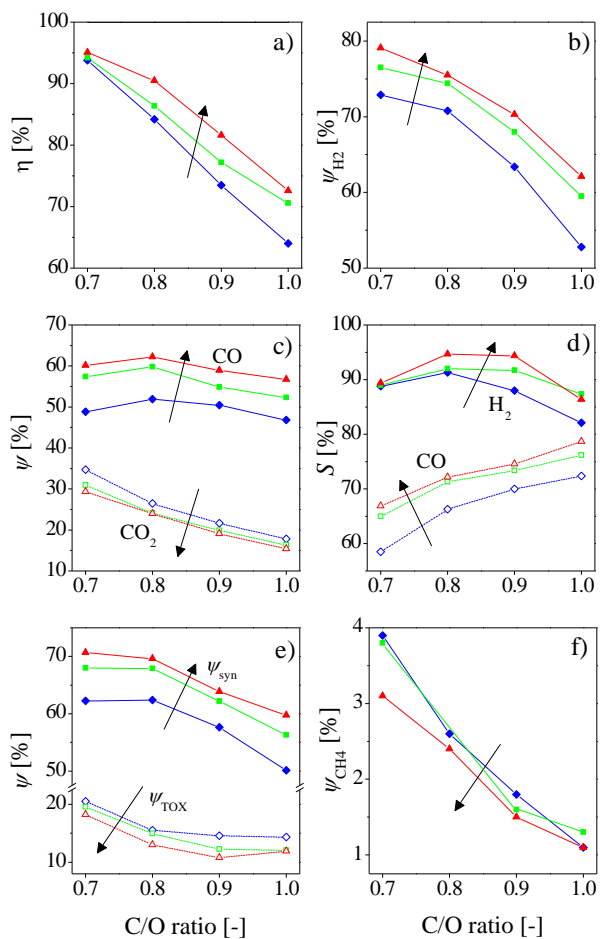


Figure 2.7: Gas analysis results at steady-state conditions measured 90 min after reaction start. The arrows represent the gas inlet flow rate increase from 150 sccm (blue, diamond) to 170 sccm (green, square) and 190 sccm (red, triangle). **a)** The $n\text{-C}_4\text{H}_{10}$ conversion as a function of C/O ratio. **b)** The H_2 yield. **c)** The yields of CO and CO_2 . **d)** The H_2 and CO selectivities. **e)** The yield of catalytic reaction for POX and TOX reactions. **f)** The CH_4 yield.

Table 2.1: Molar fractions of effluent species for C/O = 0.8 at all investigated flow rates.

Flow rate [sccm]	150	170	190
Species [$\mu\text{mol s}^{-1}$]			
n - C ₄ H ₁₀	1.188	1.166	0.899
H ₂	26.624	31.708	35.983
H ₂ O	2.550	3.267	2.001
CO	15.622	20.394	23.723
CO ₂	7.955	8.221	9.155
CH ₄	0.489	1.135	0.572

The yield for POX and TOX reactions increases by decreasing C/O ratio (Figure 2.7e). The POX yield increases while the TOX yield decreases by increasing the flow rate.

The maximum power that an ideal fuel cell could deliver (P_{SYN}) is depicted in Figure 2.8. This parameter reaches its maximum for $V_{\text{gas,in}} = 190$ sccm at C/O = 1.0. This can be simply explained by the higher amount of input fuel at this ratio. A deeper insight into the relevance of this maximum power output level is achieved by introducing an energetic efficiency factor for CPO defined as

$$E_{ff,\text{CPO}} = \frac{P_{\text{SYN}}}{\dot{n}_{\text{C}_4\text{H}_{10},\text{in}} \cdot \text{LHV}_{\text{C}_4\text{H}_{10}}} = \frac{\dot{n}_{\text{H}_2} \cdot \text{LHV}_{\text{H}_2} + \dot{n}_{\text{CO}} \cdot \text{HV}_{\text{CO}}}{\dot{n}_{\text{C}_4\text{H}_{10},\text{in}} \cdot \text{LHV}_{\text{C}_4\text{H}_{10}}} \quad (2.12)$$

where LHV is the lower heating value (2657 kJmol^{-1} and 242 kJmol^{-1} for n-C₄H₁₀ and H₂, respectively) and HV_{CO} the heating value of CO₂ (283 kJmol^{-1}) at 298 K [18].

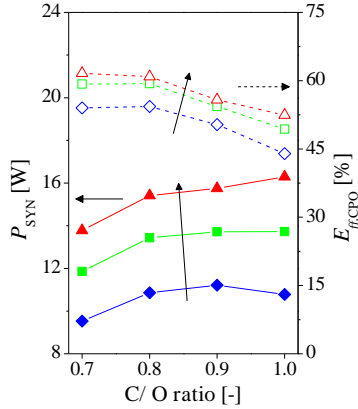


Figure 2.8: Power contained in the produced syngas species at different flow rates (filled symbols) and overall energetic efficiency of the catalytic partial oxidation reaction (empty symbols). The arrows (solid lines) signify the increase of inlet flow rates.

The energetic efficiencies of the reactions are also depicted in Figure 2.8. The trend is identical to the trend of syngas yield, and reaches 61.6% and 60.9% for the highest inlet feeds at $C/O = 0.7$ and 0.8 , respectively. In addition, as with the syngas yield and H_2 selectivity, a plateau starts developing at $C/O = 0.8$ moving towards lower efficiency levels at higher C/O ratio. The power delivered by the syngas products, the energetic efficiency and corresponding T_{in} for all flow conditions at $C/O = 0.8$ are summarized in Table 2.2.

Table 2.2: Power and energetic efficiency of POX for all three investigated flow rates at $C/O = 0.8$.

Flow rate [sccm]	150	170	190
T_{in} [°C]	773	792	809
Power [W]			
P_{H_2}	6.44	7.67	8.70
P_{SYN}	10.86	13.44	15.42
Efficiency [%]			
$E_{eff,CPO}$	54.3	59.3	60.9

Dependency on the stop temperature

In the following measurements the dependency of the steady-state temperature and the start-up time on the stop temperature T_{stop} at which the electrical heating is turned is investigated. For this purpose, a feed gas mixture containing n-C₄H₁₀/air = 14.1 sccm and 175.9 sccm (C/O = 0.8) is used for three different T_{stop} values: 400°C, 500°C and 550°C, as well as a stop point just when the oxidation reaction is ignited. At these temperature levels, the heater is turned off and the reaction left to reach steady conditions. The variation of electrical power input due to an increase in temperature during the hybrid start-up is up to 9% for 550°C and only around 1% for the lowest T_{stop} . The profiles of T_{SOFC} for all investigated stop points during the first 20 min of the experiments are depicted in Figure 2.9. Note that before the heater is turned off, the slope of the hybrid start-up is almost the same for all measurements. T_{SOFC} slightly decreases right after the electrical heater is turned off. All temperature profiles show a convergence towards steady conditions after around 500 s from the start of the experiments, regardless of the time when the heater is turned off.

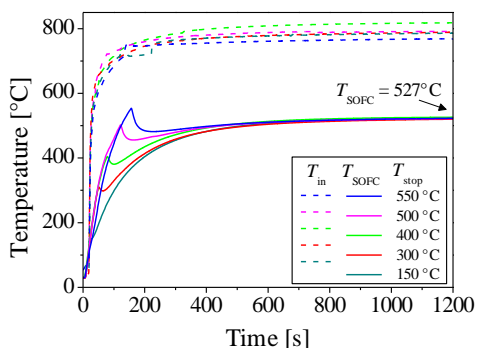


Figure 2.9: Temperature profiles for T_{in} (dashed lines) and T_{SOFC} (solid lines) at different stop temperatures (T_{stop}).

The transient experimental studies on the same catalyst as used in this study and similar rhodium-doped catalysts have shown high syngas production at much lower temperatures during heat-up or ignition of reaction in a heated

catalytic bed [48,52]. We define the start-up time ($t_{\text{POX,start-up}}$) as the time where the transient temperature reaches 95% of the steady-state temperature (in K).

The results of the measured start-up times and the reference measurement (see section “Varying the stop temperature”) are shown in Table 2.3. The heat input $E_{\text{heater,hybrid}}$ is defined as the input electrical power during hybrid start-up time ($t_{\text{heater,hybrid}}$), which is the time needed to reach the desired T_{stop} . $E_{\text{POX,start-up}}$ is the energy input for the POX reaction and is equal to the inlet mass flow of n-butane times its LHV times $t_{\text{POX,start-up}}$. E_{tot} signifies the sum of the hybrid total energy $E_{\text{heater,hybrid}}$ and $E_{\text{POX,start-up}}$. The electric start-up measurements are performed by heating only electrically without any gases flowing into the system.

The fastest start-up (286 s) is achieved after hybrid heating until 550°C and is at the same time the most costly one from an energetic point of view. The start-up case consuming the least amount of electrical energy (only 101.3 J) is the one in which the hybrid heating is stopped just when ignition of reaction is achieved (at $T_{\text{SOFC}} = 150^\circ\text{C}$), saving up to 938 J during hybrid heating. This energy saving, however, comes at the price of 139 s increase in the start-up time compared to the least energetically efficient start-up case. Table 3 also clearly shows that the hybrid start-up is faster and much more energetically efficient compared to the electric heating alone. The reference measurement reaches maximum temperature of 501°C after 624 s. Compared to electric heating alone, the time to reach 300°C and 500°C could be lowered by 45 s and 503 s, respectively. This means that 300 J and 3392 J less electrical input energy are required to reach both temperature levels, respectively.

Table 2.3: Energies and times required to achieve reaction ignition and different stop temperature levels (T_{stop}) for hybrid and non-hybrid conditions.

T_{stop} [°C]	550	500	400	300	150
Hybrid start-up					
$t_{\text{heater,hybrid}}$ [s]	154.0	120.0	76.5	48.0	15.0
$E_{\text{heater,hybrid}}$ [J]	1039.5	810.0	516.4	324.0	101.3
$t_{\text{POX,start-up}}$ [s]	286.0	337.0	385.0	411.0	425.0
$E_{\text{POX,start-up}}$ [J]	7239.5	8530.5	9745.5	10403.6	10758.0
E_{tot} [J]	8279.0	9340.5	10261.9	10727.6	10859.2
Electric start-up					
t_{electric} [s]	-	622.5	208	92.5	40.8
E_{electric} [J]	-	4201.9	1404.0	624.4	275.4

Figure 2.10 shows the heater hybrid time, the start-up time and the required start-up energy as functions of T_{SOFC} . It is important to mention that T_{in} is not affected substantially by the chosen stop temperature for all measurements.

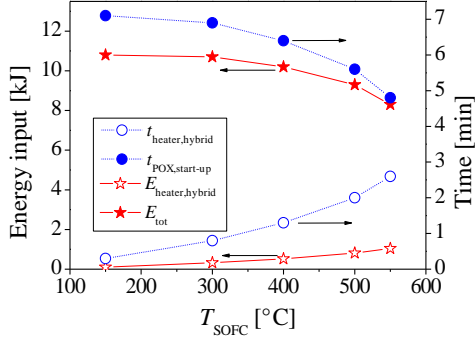


Figure 2.10: The input energy ($E_{heater,hybrid}$) for different temperature levels at the micro-SOFC membrane (T_{SOFC}) as well as total energy (E_{tot}) required to reach 95% of steady-state temperature (in K), together with the start-up time ($t_{POX,start-up}$) and heater hybrid time ($t_{heater,hybrid}$).

2.4 Discussion

The results of the experiments by varying C/O ratios and flow rates show that syngas production in the presence of 1.9 wt% Rh-doped $Ce_{0.5}Zr_{0.5}O_2$ nanoparticles is possible for a wide range of gas inlet feeds close to and with stoichiometric reforming conditions at t_{space} as low as 8 ms.

All temperatures at steady conditions show an exponential increase similar to the O/C ratio (Figure 2.5), which provides us with a better understanding of the stoichiometry of the reaction for this type of measurements than the linear C/O ratio. Exact temperature readings at the inlet of the reactor are possible up to a certain degree, since incoming cold gases can have a cooling effect on the thermocouple, which seems to be the case for the steady-state temperatures achieved at the inlet of the reactor using C/O = 0.7. The values of T_{SOFC} are more stable and reproducible than the ones at T_{in} . Temperatures within the desired range of 500°C to 550°C at the micro-SOFC can be achieved for only 5 out of 12 cases. However, higher temperature levels can be achieved by only varying the inlet flow rate at the desired C/O ratio.

A slight temperature decrease after turn-off of the electric heating at T_{stop} can be observed in Figure 2.6a. This is caused by the higher amount of heat supplied by the heating wire compared to the heat of POX reaction and only affected T_{SOFC} . The fast temperature increase at T_{in} after reaction ignition (Figure 2.6b) is comparable to the results obtained by Katsutoshi et al., who triggered n-butane reforming at room temperature after initial H_2 -reduction of the CeO_2 substrate doped with nickel [55] and rhodium [56].

While n- C_4H_{10} conversion, effluent species yields and selectivities are not directly comparable due to differences in temperatures, general comparisons can be made because all reactions are carried out on identical total gas feeds and relatively similar space times ($t_{\text{space}} = 11.0\text{--}7.7$ ms). The results shown in Figure 2.7 demonstrate that shorter space times (higher flow rates) lead to increase in the n-butane conversion, which is in contrast with our expectations [14]. The two main factors expected to influence high n-butane conversion, the temperature in the catalytic bed and the space time in which the reactants are exposed to the catalytic surface, act inversely towards a high conversion. By reducing the space time of the reactants, the available time for the reaction to take place is decreased and leads to lower reaction rates whereas a high temperature level enhances conversion of the fuel. It is clear from our results that the increase in temperature has a greater influence on the fuel conversion as well as on the H_2 and CO yields than the slight difference in space times. Furthermore, similar experimental studies by Seyed-Reihani [52] and Hotz et al. [14] demonstrated that the highest amount of POX reaction occurs rapidly within the first few mm of the reactor, so that low space times enhanced syngas production.

The maximum H_2 yield is 79% for $\text{C/O} = 0.7$ and is comparable to the results obtained by Nagaoka et al. [56] where CPO of n-butane on rhodium-coated ceria nanoparticles showed a H_2 yield as high as 83% at temperatures above 900°C in the reactor at steady-state conditions. The highest syngas yield is found to be around 70% for both $\text{C/O} = 0.7$ and 0.8. The lower temperature developed by the C/O ratio closer to stoichiometric POX conditions has similar or equal H_2 yield and synthesis gas yield. This leads to the conclusion that a turning point at $\text{C/O} = 0.8$ is expected, which starts developing already for low flow rates. This stands in accordance with the simulation study based on the CPO of CH_4 on Rh-surfaces by Chaniotis et al. [62] who identified $\text{C/O} = 0.8$ as the best choice for high CPO rates.

The production of CH₄ at low space times is proved once again to be mainly caused by mass transfer limitation [14,54,63]. The maximum outlet flow rate is 1.1 μmol s⁻¹ accounting to a mole fraction of only 1.5% for the simplest hydrocarbon in the outlet gas mixture. Other lower hydrocarbons could not be detected in the off-gases compared to other studies where low quantities of C₂ - C₃ species on rhodium, nickel and platinum coated monoliths were found [16,64,65]. As in other studies, the use of ceria supported Rh-nanoparticles suppressed lower hydrocarbon formation [14,30,56].

The steady-state temperature within our range of interest, the maximum point at C/O = 0.8 in terms of energetic efficiency and syngas yield as well as a higher maximum power in the outlet syngas species than at C/O = 0.7 at constant flow rates, are the main reasons to continue the investigation of optimization of the hybrid start-up time at C/O = 0.8.

The results of the influence of the stop temperature on the start-up time summarized in Figure 2.10 clearly show a tradeoff between a fast start-up at the price of high input electrical energy and a slow start-up with the advantage of less input energy. Notably, the hybrid start-up is the best choice for both fast and energy efficient start-up, as shown in Table 2. In the hybrid start-up, an electric energy input and heating time reduction by 3392 J and 503 s, respectively, compared to electric heating alone are possible. For the hybrid start-up method, a time reduction by 139 s is achieved by a 10x higher input electrical energy. If the start-up time is not a concern, the slower but more energetic efficient start-up is recommended. A slow transient H₂ and CO production would also signify a transient behavior of the micro-SOFC in terms of power generation and temperature increase, as well as exposure of the membranes to unburned n-butane, which could deactivate the fuel cell by carbon deposition [66]. On the other hand, if the goal is to achieve a faster start-up, higher energy input is required. Nevertheless, a very fast start-up could lead to a decrease of performance of the fuel cell [67]. Micro-SOFC membrane materials should be capable of withstanding high temperature increase rate of even 60°Cs⁻¹, as shown in this study.

Temperature measurements at T_{in} and T_{SOFC} as low as 75°C and 150°C for reaction ignition, respectively, are very low and stand in contrast with studies regarding catalytic ignition of light hydrocarbons that show that temperatures above 200°C are needed for triggering of butane catalytic oxidation reaction [68]. The main reason for this discrepancy is the higher temperature in the

catalytic bed compared to the one measured at T_{in} and T_{SOFC} . It is also probable that the contact of the reacting gas mixture with the much hotter heating wire at the back face of the catalytic bed help trigger the reaction. The latter would suggest that a positioning of the heating wire at the front face of the catalytic bed could be of advantage towards a faster lightoff but of disadvantage for the micro-SOFC membrane, since the heating wire would lie farther away from the micro-SOFC membrane. In this case, heating of the fuel cells would be enhanced by heat conduction from the inlet to the back face of the micro-reactor. Other tunable parameters for achieving shorter start-up times are catalytic bed volume and especially the chosen material, not only for the micro-reactor but most importantly for the whole micro-SOFC system. A micro-fabricated-silicon-based micro-SOFC power plant would for example enhance heat transport and isothermal conditions not only in the reactor, but also throughout the whole system. Better heat distribution in a micro-reactor would enhance syngas yield in the regions where especially endothermic and weak exothermic reactions would dominate.

2.5 Conclusion

The n-C₄H₁₀ catalytic partial oxidation over 1.9 wt% Rh/Ce_{0.5}Zr_{0.5}O₂-supported nanoparticles at different flow rates and gas compositions was successfully ignited by means of a hybrid-start-up method consisting of an electrical heater made of a resistance wire and the exothermic oxidative catalytic reaction. The use of Rh as catalytic material has shown again to be of advantage for high syngas yield in small and compact micro-reactors and resistant to carbon deposition, as TEM pictures revealed.

Experiments showed a syngas yield of over 50% for all investigated gas inlet compositions. A C/O ratio of 0.8 and a total inlet flow rate $V_{gas,in} = 190$ sccm were identified as very good parameters for the short-time reaction ($t_{space} = 8$ ms) due to the high H₂ and CO yields (75.5% and 62.2%, respectively), a syngas yield of 70%, an energetic efficiency of CPO reaction of 60.9%, and finally due to the steady-state temperature developed on the simulated micro-SOFC membrane of around 530°C.

A hybrid start-up process was proven to be faster and energetically more efficient than electrical heating alone. By varying the stop time of the electrical heating from ignition point to 550°C, a tradeoff was found between a fast

energy consuming and an energetic efficient but slow start-up. For the hybrid start-up method, a time reduction of 139 s was achieved by a 10x higher electrical energy input. Important for a fast start-up was the thermal cycling characteristics of micro-SOFC membranes, which should be able to withstand high temperature ramps of as high as $60^{\circ}\text{C}\text{s}^{-1}$, as presented in this study. For the sake of simplicity, we assumed the absence of a post-combustor unit for the effluent gases of the micro-SOFC. By implementation of this unit, an even faster start-up is feasible due to strong exothermic catalytic combustion reactions. Additionally, this unit allows a clean exhaust without flammable or toxic gases, allowing the use of the ONEBAT system in a safe environment.

3 A nanoparticle bed micro-reactor with high syngas yield for moderate temperature micro-scale SOFC power plants

Parts of this chapter are published in:

A. J. Santis-Alvarez, M. Nabavi, B. Jiang, T. Maeder, P. Muralt, and D. Poulikakos, "A nanoparticle bed micro-reactor with high syngas yield for moderate temperature micro-scale SOFC power plants," *Chemical Engineering Science*, vol. 84, pp. 469-478, 2012.

Abstract

This work introduces and investigates a novel compact catalytic nanoparticle bed micro-fabricated reactor suitable for utilization in small-scale intermediate-temperature SOFC systems. It is shown that the presented micro-reactor is able to produce syngas ($\text{CO} + \text{H}_2$) efficiently from n-butane and propane at temperatures between 550–620°C by means of catalytic partial oxidation (CPO) using Rh-doped nanoparticles embedded in a foam-like porous ceramic bed as a catalyst. The micro-reactor is tested using a carrier specially designed for heating the reactor as well as feeding the fuel and receiving the reaction product gases. The performance of the micro-reactor was investigated in two modes: (1) Continuous heating mode, in which two built-in heaters underneath the carrier are kept on throughout the reforming reaction. This simulates the operating state of a micro-SOFC system where the post-combustor provides heat to the micro-reactor continuously. (2) Thermally self-sustained mode, in which the heaters are turned off after the CPO has been ignited. An estimation of the heat losses of both testing modes is also given. The present micro-reactor is able to achieve syngas yield as high as 60% for n-butane and 50% for propane in the continuous heating mode, which is a substantial improvement to state-of-the-art micro-reactors.

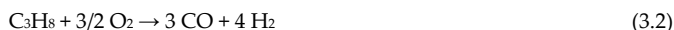
3.1 Introduction

Micro-scale fuel cell devices are being investigated intensively, due to their potential to deliver higher energy density than common Li-ion-batteries [39,40,69,70] combined with the inherent fuel cell features in power generation. Among all fuel cell types, solid oxide fuel cells (SOFC) have the advantage of coupling high fuel flexibility with high efficiency and long-term stability. Due to the high operating temperature of SOFCs, a wide variety of hydrocarbons can be reformed to generate syngas fuel ($\text{CO} + \text{H}_2$) either directly on the anode (internal reforming) [42,47,71-74] or in a separate reactor (external reforming) [75]. The decoupling of syngas generation from the SOFC-membranes has the advantage of allowing an easier and more precise optimization of the fuel-processing unit, leading to an increase in the overall efficiency of such a system.

Studies on micro-scale fuel processors for small-scale fuel cell devices have been primarily focused on steam reforming of hydrocarbons and alcohols [76-81] mostly at temperatures below 350°C . Tanaka et al. [82] introduced a micro-fuel reformer system able to reform methanol at temperatures as low as 180°C . The heat in the system was provided by either a micro-heater or by an integrated micro-combustor, in which n-butane was oxidized in order to produce enough heat for the endothermic reforming reaction.

Micro-fabricating reactors with a needed broad palette of materials becomes challenging as the operating temperature requirements increase. High temperature micro-structured reactors have been investigated primarily for hydrocarbon-to-hydrogen-conversion [83-86]. Pennemann et al. [87] studied a micro-structured reactor for the partial oxidation of propane at temperatures between 700 and 850°C . For this purpose, novel metals like palladium, platinum and rhodium on alumina were wash-coated onto the micro-structured channels of their reactors. The high temperatures were obtained from an external heating source. Younes-Metzler et al. [88] introduced a micro-fabricated silicon-reactor setup for the partial oxidation of methane at high-temperatures. In their study, the reaction is catalyzed on a palladium-coated channel and activated using an external resistive heating device placed on top of the reactor chip. The fabrication procedures of such metal coated micro-reactors are complicated and time consuming. There is a need for cost-effective, simple fabrication techniques for such devices.

The novelty of the present work is the introduction of a feasible, compact, micro-fabricated reactor/catalyst concept and the study of its suitability to produce syngas efficiently at intermediate temperatures (between 550–620°C) for micro-SOFC applications. The syngas is generated from n-butane and propane:



These hydrocarbons are selected because of their high energy content (45.7 MJ kg⁻¹ and 26.2 MJ L⁻¹ at 25°C for n- C₄H₁₀ and 46.4 MJ kg⁻¹ and 22.8 MJ L⁻¹ at 25°C for C₃H₈, respectively), feasible portability due to relatively low vapor pressure (243 kPa and 952 kPa at 25°C for n-C₄H₁₀ and C₃H₈, respectively), their high availability and their wide societal acceptance.

Rhodium metal on ceria-zirconia support (Ce_{0.5}Zr_{0.5}O₂) nanoparticles is used as catalytic material due to its proven ability to deliver high syngas yield at different intermediate temperatures and fuel dilutions [89-91]. The Rh-catalyst is embedded in the micro-reactor by a one-step sol-gelation process [30], which allows filling of nanoparticles in different reactor shapes, thus avoiding expensive and cumbersome deposition procedures or other complex coating or impregnation steps. This simple process has proven to be reliable for small size reactors, as the one reported in this study.

For reactor heating, two built-in screen-printed resistive heaters on a specially fabricated micro-reactor carrier unit were employed. This carrier unity was fabricated by a thin film deposition process utilizing standard thin-film procedures and also served as support for gas transport to and from the micro-reactor.

The micro-reformer presented here can be integrated directly in a micro-SOFC power plant and is shown to be capable of producing enough syngas and serve as a gas processing unit for such a device.

3.3 Experimental methods

The micro-reactor and the carrier testing platform

The micro-reactor used in this study was fabricated by standard micro-fabrication techniques on a 1000 μm thick Si-substrate (Figure 3.1a). The substrate was etched to a depth of 500 μm using potassium hydroxide (KOH). Masks with compensation structures for the pins and the walls were used in order to obtain the desired 1.5 mm \times 1.5 mm quadratic pins (needed for structural integrity) and the 5 mm \times 0.5 mm rectangular structures (at the walls, for mechanical stability at the borders) during KOH-etching. A 1000 μm thick borosilicate glass 3.3 with two drilled holes of 2 mm in diameter was subsequently anodically bonded onto the Si-substrate. The dimensions of the catalytic bed and the micro-reactor are 11.0 mm \times 11.5 mm \times 0.5 mm and 12.7 mm \times 12.7 mm \times 2.0 mm, respectively. The catalytic bed volume (V_{reactor}) is 58.5 mm³.

The optimization of the reactor design was accomplished by standard numerical simulations (not presented for brevity) of gas flow in a porous layer simulating the catalyst bed, performed using the CFX package (version 12.1) for ten different reactor geometries. The numerical study showed that the present design with two square pins in the micro-reactor enhanced flow uniformity and distribution and minimized dead volumes.

The 1.9 wt% Rh on Ce_{0.5}Zr_{0.5}O₂ catalytic nanoparticles with an average diameter of 12 nm were synthesized in a one-step process by flame spray synthesis as described in [89]. The catalytic ceramic foam was prepared by a one-step sol gelation process as described and characterized by Hotz et al. [30]. As in previous studies [14,30,48,89], we kept the same nanoparticle to sand weight ratio to 1:3. For preparation of the ceramic foam, 24.1 wt% catalytic nanoparticles, 72.2 wt% washed and calcined SiO₂-sand (Riedel-deHaën, average diameter: 200 μm , puriss p.a.), 0.9 wt% gelation agent (triammonium citrate, Riedel-deHaën, purity \geq 97%) and 2.8 wt% ceramic binder (sodium metasilicate pentahydrate, Riedel-deHaën, purity \geq 97%) were mixed with the same mass of deionized water (18 M Ω). The mixture was manually stirred and then placed in an ultrasonic bath for 5 min. These steps resulted in a highly viscous suspension which was then introduced inside the micro-reactor through the openings. The reactor was shaken regularly during the filling process in order to avoid empty areas that could result in unused or

dead volumes. The water in the reactor was removed by thermal treatment after heating up to 100°C with a heating rate of 2.5°Cmin⁻¹ and by keeping this temperature for 60 min. The reactor was heated up to 650°C for 20 min with a heating rate of 10°Cmin⁻¹. This step was necessary in order to ensure that the catalytic bed could sustain such high temperature levels without any crack formation (Figure 3.1a).

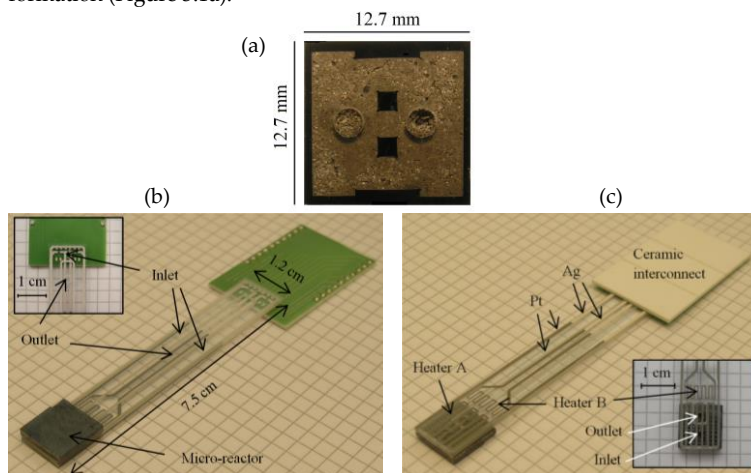


Figure 3.1: (a): The micro-fabricated reactor filled with dried catalytic material.

Top (b) and bottom (c) views of the assembled micro-reactor and carrier unit. The symmetric fluidic channels and built-in heaters on the carrier testing-platform are also shown.

In order to be able to characterize the micro-reactor, a specially-designed carrier unit was fabricated using standard thin film fabrication techniques (Figure 3.1b and c). The carrier has two important functionalities: First, it allows the gas transport to and from the micro-reactor at the intermediate temperatures needed for this study and second, it provides the necessary activation temperature of the reaction by means of two resistive heaters.

The carrier was made of two layers of Schott AF 32® Eco Glass which tolerates high operating temperatures (thermal expansion coefficient = $3.2 \times 10^{-6} \text{ K}^{-1}$, transformation temperature = 717°C, Schott AG). As material for the carrier, we chose glass instead of silicon to prevent heat transfer from the reaction zone through the carrier to the inlet and outlet connections. Glass also provides much better thermal insulation for the micro-reactor, which is

desirable when high operating temperatures are needed. The micro-channels were fabricated between two glass layers (Figure 3.1b and c). For this purpose, a glass frit powder (Ferro IP 760c, Ferro Corporation) was formulated with a vehicle consisting of ethyl cellulose binder (EC-300-48, Sigma-Aldrich), plasticized with triethylene glycol bis(2-ethylhexanoate) and dissolved in a terpineol-dibutyl carbitol solvent mix. The paste was screen-printed onto both glass plates. The assembly was accomplished by heating up to 700°C under a load of 150 g to ensure tightness of glass frit walls between the micro-channels. The average thickness of the glass frit layer (height of micro-channels) was 150 μm. The dimensions of the carrier were 75 mm × 12 mm × 1.75 mm.

The micro-reactor was also assembled on top of the carrier using the same technique. Two heating tracks made of silver and platinum were also screen printed onto the carrier glass with a thickness 2.5 ± 0.4 μm and two widths of 0.4 mm and 0.6 mm, respectively. A ceramic interconnect allowed the power supply to the heating tracks. In a final step, the mechanical interconnects were made by simply attaching two stainless steel connections using epoxy (STYCAST 2741 W1–Catalyst 15, Emerson & Cuming) on top of the carrier inlet and outlet holes (Figure 3.1b).

Test setup and procedures

The specified hydrocarbon fuel (PanGas, purity of both hydrocarbons: 99.95%) was diluted with synthetic air (80 vol% N₂, 20 vol% O₂, PanGas, 99.9996%) at room temperature (20°C) at specified fuel to oxygen ratios before the inlet of the testing platform. The different feed compositions are represented by

$$C / O = \frac{x}{2} \cdot \frac{\dot{n}_{C_xH_y,in}}{\dot{n}_{O_2,in}} \quad (3.3)$$

and their values are defined by the molar oxygen to fuel ratios in the proximity to stoichiometric CPO reaction:



The micro-reactor testing platform was insulated with two insulation blocks (WDS@Ultra, 5 cm × 10 cm × 10 cm each, of thermal conductivity = 0.018 Wm

$^1\text{K}^{-1}$ at 50°C varying to $0.031 \text{ Wm}^{-1}\text{K}^{-1}$ at 600°C , Porextherm Daemmstoffe GmbH). The temperature on top of the micro-reactor was measured by two K-type thermocouples.

For the noble metal rhodium, reactions (4.1) and (4.2) are activated at temperatures above 300°C [90,92]. For this purpose, two screen printed resistive heaters on the carrier were powered by a power supply in order to activate the reaction at different temperatures.

The exhaust gas composition was monitored by a gas chromatograph (6890 GC, with a HP-PlotQ column, Agilent) every 25 min until the micro-reactor reached steady state conditions. We defined steady conditions when fuel utilization (conversion) and syngas yield showed no significance variation with time (standard deviation, $\sigma \leq 0.8\%$) and the temperature rise remained within 1°C during 10 to 15 min. We defined T_{op} as the operation temperature at which steady conditions were obtained. In the case of successful reaction ignition, these conditions were achieved after approximately 95 and 120 min of reaction time. After this time the reaction was terminated by stopping the gas flow. The molar product gas balances for C, H and O atoms closed within 5% for all experiments.

The results of the gas analysis were quantified primarily by means of fuel conversion, H_2 and syngas yield and molar CH_4 to inlet fuel ratio (see Table 3.1).

Table 3.1: Characteristic parameters for gas composition analysis.

Fuel conversion:	$\eta = \frac{\dot{n}_{\text{C}_x\text{H}_y,\text{in}} - \dot{n}_{\text{C}_x\text{H}_y,\text{out}}}{\dot{n}_{\text{C}_x\text{H}_y,\text{in}}}$
Yield of H_2 and CO :	$\psi_{\text{H}_2} = 2 \cdot \frac{\dot{n}_{\text{H}_2}}{y \cdot \dot{n}_{\text{C}_x\text{H}_y,\text{in}}}, \psi_{\text{CO}} = \frac{\dot{n}_{\text{CO}}}{x \cdot \dot{n}_{\text{C}_x\text{H}_y,\text{in}}}$
Yield of syngas:	$\psi_{\text{syngas}} = \frac{\dot{n}_{\text{H}_2} + \dot{n}_{\text{CO}}}{\left(\frac{y}{2} + x\right) \cdot \dot{n}_{\text{C}_x\text{H}_y,\text{in}}}$
Molar methane to inlet fuel ratio:	$x_{\text{CH}_4} = \frac{\dot{n}_{\text{CH}_4}}{\dot{n}_{\text{C}_x\text{H}_y,\text{in}}}$
Selectivity of H_2 and CO :	$S_{\text{H}_2} = \frac{\dot{n}_{\text{H}_2}}{\dot{n}_{\text{H}_2} + \dot{n}_{\text{H}_2\text{O}}}, S_{\text{CO}} = \frac{\dot{n}_{\text{CO}}}{\dot{n}_{\text{CO}} + \dot{n}_{\text{CO}_2}}$

3.4 Results and discussion

We investigated the performance of the micro-reactor in two different testing modes: (1) The continuous heating mode, in which the heaters underneath the carrier are kept on throughout the reforming reactions. The continuous heat source simulates an additional unit in the system such as a post-combustor device [82,93], providing constant heat to the reactor during its operation,. The continuous heating mode is also advantageous as it helps achieving adjustable temperatures in the micro-reactor in order to characterize its performance in a systematic manner. (2) The thermally self-sustained mode, which simulates the case where the post-combustor is not present or is not thermally connected to the micro-reactor. It also simulates a possible startup scenario, with a limited, initial activation electrical heating. After activation of the thermally self-sustained reaction, the power supplied to the heaters for reaction start-up was turned off. The start of the reaction was indicated by a sudden temperature increase caused by the energy released from exothermic reaction.

In order to have comparable conditions for the abovementioned constant heating and self-sustained scenarios, we targeted temperatures at steady state between 550 and 620°C. To accomplish this, we selected low gas flow rates, which resulted in space times, t_{space} , (4.5) of the reactants in the catalytic bed in the range of several ms. The total inlet flow rate ($V_{\text{gas,reactor}}$) for the experiments under constant resistive heating was 30 standard cubic centiliters per minute (sccm) and for the experiments on the thermally self-sustained reaction was 60 sccm.

$$t_{\text{space}} = \frac{V_{\text{reactor}}}{V_{\text{gas,reactor}}} \quad (3.5)$$

Effect of fuel dilutions and set temperature on product composition

In the first set of experiments, a continuous heat source was used during all experiments to obtain the desirable temperatures at the top of the micro-reactor. We defined T_{set} as the temperature at the top of the micro-reactor when no gas was flowing through it, controlled by the power input to the heaters. In order to investigate and optimize the performance of the micro-reactor, we varied the carbon to oxygen (C/O) ratios of the inlet gas mixture and T_{set} . For both fuels we used the C/O values of 1.0, 0.8, 0.7 and 0.6 for a

total inlet flow of 30 sccm. Stoichiometric conditions ($C/O = 1.0$) were tested as reference values, while the other values were chosen to determine C/O at which the maximum CPO performance in terms of syngas yield can be achieved.

Once the temperature on top of the micro-reactor reached the desired T_{set} , the reacting gas mixture was fed through the catalytic bed until T_{op} was obtained. Figure 3.2 shows the characteristic temperature increase behavior from T_{set} to T_{op} observed during these experiments.

As shown in Figure 3.2, for $T_{set} < 300^\circ\text{C}$, no significant change in temperature was obtained. At $T_{set} = 300^\circ\text{C}$, the temperature rose only to a small extent, whereas for $T_{set} \geq 350^\circ\text{C}$, the temperature rise was significant.

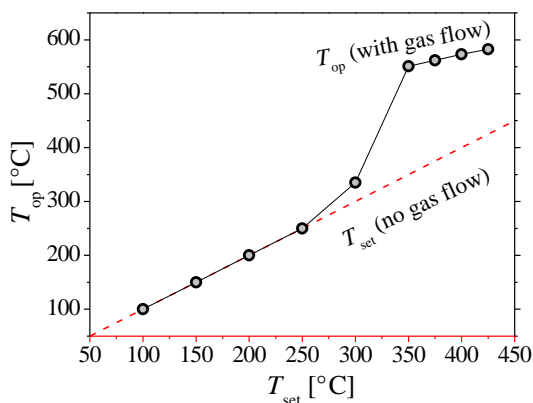


Figure 3.2: Characteristic temperature behavior during testing. T_{set} (dashed red line) denotes the set temperature at the micro-reactor without any gas flow and T_{op} (circles) represents the micro-reactor temperature with a total inlet flow rate of 30 sccm at steady state conditions.

Gas composition analysis showed that for $T_{set} < 300^\circ\text{C}$, the diluted hydrocarbon-air mixture did not undergo any change inside the micro-reactor and that no thermal decomposition at these temperature levels occurred. At $T_{set} = 300^\circ\text{C}$, fuel conversions below 15 percent were obtained and consequently the thermal decomposition products, CO_2 and H_2O vapor, were identified in the outlet gas stream. For $T_{set} \geq 350^\circ\text{C}$, higher fuel conversions, H_2 and CO among other gases were detected, confirming the successful activation of the CPO reaction. Also characteristic for the ignition of the CPO

reaction was the total consumption of oxygen, which could not be detected at any point in time during the gas measurements after the CPO reactions were initiated.

The effects of T_{set} and dilution ratio on T_{op} for n-C₄H₁₀ and C₃H₈ are depicted in Figure 3.3. As in [89], the final temperature follows the same trend as the oxygen to inlet fuel ratio, increasing from 550°C to almost 620°C from higher to lower C/O ratios i.e. when diluting towards stoichiometric total oxidation ratio (C/O = 0.31 for n-C₄H₁₀ and C/O = 0.30 for C₃H₈). At these values of T_{op} , the calculated residence time, t_{space} , was in the range of 40 to 44 ms for all reactions. As shown in Figure 3.3, the increase in T_{op} is lower than that in T_{set} , mainly due to the heat losses at these intermediate temperatures.

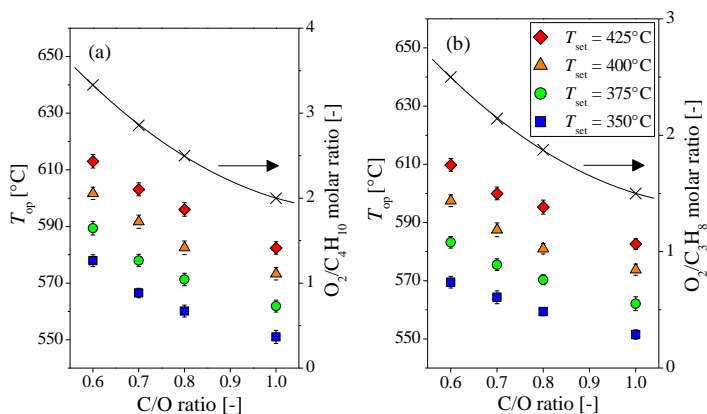


Figure 3.3: Effect of T_{set} and fuel dilution on T_{op} for (a) n-C₄H₁₀ and (b) C₃H₈ CPO. From C/O = 1.0 to 0.6, T_{op} follows a similar trend as the O₂/C_xH_y molar ratio.

The CPO performance of the catalytic bed varied depending on the utilized fuel, fuel dilution and heating temperature. For all reactions, the outlet gas mixture contained unconverted fuel, inert N₂, H₂O vapor and CO₂, as well as CH₄ and syngas species. No traces of other gases such as C₂ or C₃ components were found in any case.

Figure 3.4 and Figure 3.5 depict gas analysis results obtained for both fuels at steady conditions. As shown here, for higher T_{set} , higher values of η were obtained (Figure 3.4a and Figure 3.5a). For both fuels η becomes highly

temperature dependent for lower dilutions. At $C/O = 1.0$, the difference in fuel conversion ratio values is maximum between $T_{set} = 350^\circ\text{C}$ and $T_{set} = 425^\circ\text{C}$.

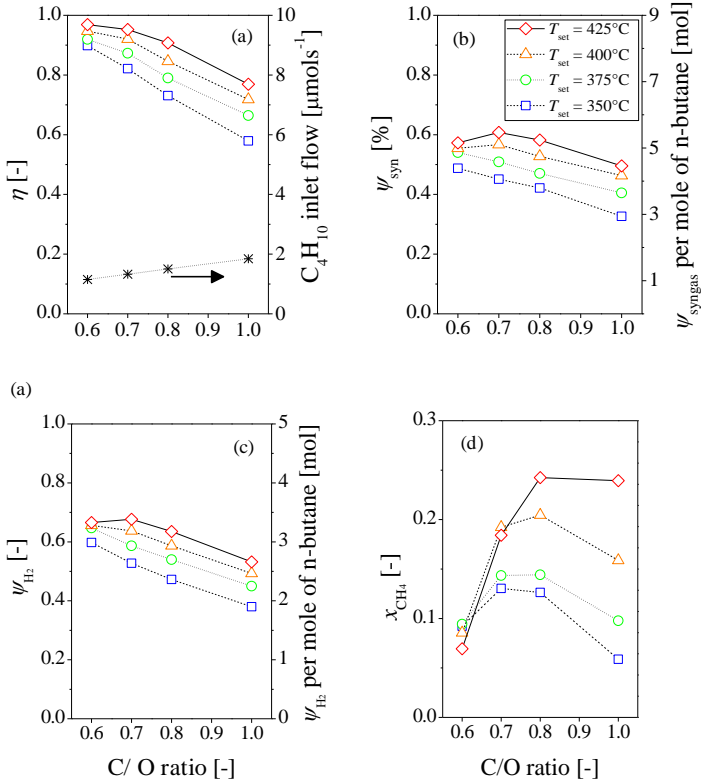


Figure 3.4: Gas analysis results for n-butane for different fuel dilutions; (a) fuel conversion, (b) syngas yield, (c) H₂ yield and (d) CH₄ to inlet n- C₄H₁₀ ratio. The symbols represent different T_{set} : squares (350°C), circles (375°C), triangles (400°C) and diamonds (425°C).

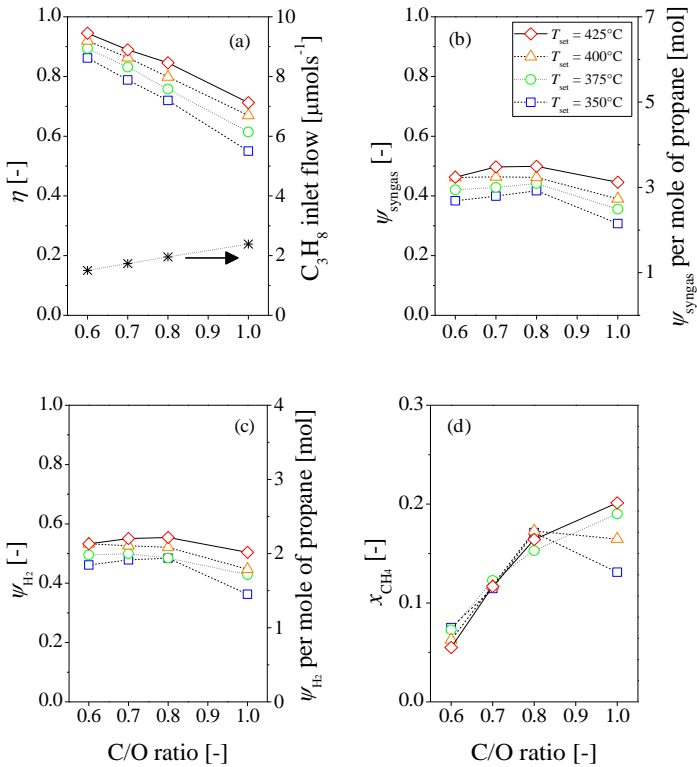


Figure 3.5: Gas analysis results for C₃H₈ for different fuel dilutions; (a) fuel conversion, (b) syngas yield, (c) H₂ yield and (d) CH₄ to inlet fuel ratio. The symbols represent different T_{set}: squares (350°C), circles (375°C), triangles (400°C) and diamonds (425°C).

In contrast to fuel utilization behavior, the syngas production (Figure 3.4b and Figure 3.5b) shows a non-monotonic behavior for different C/O values. This parameter, as well as the H₂ yield and other parameters like CH₄ production, has a stronger dependency on the fuel dilution ratio and has its maximum within the chosen dilution range (C/O = 0.8 - 0.6). For both fuels, maximum syngas values were found between C/O = 0.8 and 0.7.

CH₄ production was highest at 0.24 moles per mole of n- C₄H₁₀ and at 0.20 moles per mole of C₃H₈ for C/O = 0.8 and 1.0, respectively. As shown in Figure

3.5d, the CH_4 production is T_{set} insensitive at the values of C/O where the highest syngas production is obtained ($C/O = 0.8 - 0.7$, Figure 3.5b). Hence, a methanation process as CH_4 synthesis pathway is improbable. The fact that the highest CH_4 production per unit mole of fuel is increased at higher C/O values should be mainly caused by hydrocarbon decomposition of the higher concentrated inlet gas mixtures.

When compared to the results obtained for n-butane, lower values were obtained with respect to syngas and H_2 production for C_3H_8 for all investigated conditions (Figure 3.4b,c and Figure 3.5b,c). Due to the very similar dependence of ψ_{H_2} and ψ_{syn} of both fuels and thermodynamic behavior to C/O , we conclude that the effect of lower syngas generation is simply related to the lower efficiency of the catalytic nanoparticles towards C_3H_8 conversion. As explained by Hohn et al. [68] and Vesper et al. [94], the strength in carbon-to-hydrogen (C-H) bonds increases as the number of carbon atoms increases, therefore making it energetically more demanding for the lower chained hydrocarbons (in this case C_3H_8) to be converted by the reaction. Lower C_3H_8 conversion in comparison with n-butane are also supported by Huff et al. [49,64] who investigated various low-chained hydrocarbon fuels demonstrating the same trend of higher conversion values by increasing the number of carbon atoms in the hydrocarbon fuel. The overall lower fuel utilization values for C_3H_8 had also a direct influence on T_{op} (Figure 3.3b). Huff and Schmidt [49] also obtained lower final CPO reaction temperatures for the lower chained hydrocarbons.

In order to determine the best fuel dilution ratio in terms of optimal fuel conversion and syngas yield, the operating temperature at the top of the micro-reactor (T_{op}) should be also taken into account, since for higher T_{op} or T_{set} , syngas production rate is enhanced (Figure 3.6). For n- C_4H_{10} (Figure 3.6a) the trend in syngas yield for $C/O = 0.8$ and 0.7 are almost the same, while for C_3H_8 (Figure 3.6b), a fuel dilution of 0.8 shows higher syngas yield. The maximum ψ_{syn} achieved was 60% at $C/O = 0.7$ for n- C_4H_{10} and 50% at $C/O = 0.8$ for C_3H_8 .

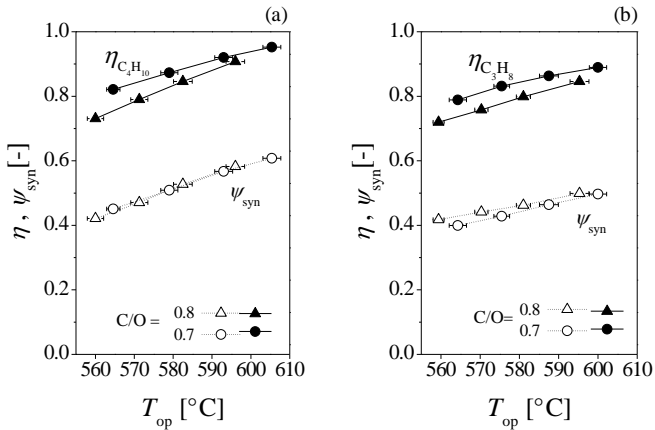


Figure 3.6: Temperature effect on η and ψ_{syn} for (a) $n\text{-C}_4\text{H}_{10}$ and (b) C_3H_8 . The lines for constant C/O ratio through the data points are curve fits.

As shown in Figure 3.7, our experimental results indicate that for n -butane at t_{space} of approximately 40–44 ms, the obtained ψ_{syn} and ψ_{H_2} at the corresponding T_{op} on top of the micro-reactor are similar to those predicted by thermodynamic equilibrium calculations. For C_3H_8 (Figure 3.7e-h), thermodynamic values lie higher than our experimental results, with the exception at stoichiometric CPO conditions, where higher experimental syngas production is obtained. Despite similarities, thermodynamic equilibrium calculations only serve as reference for our system, since they do not take into consideration catalytic activities like non ideal (complete) fuel conversion and other complex aspects of reactant behavior along the reaction path. For example, different reaction pathways towards H_2 generation run simultaneously in different regions inside the reactor [95,96]. To this end, at reactor inlet, partial oxidation competes primarily with total oxidation reaction. Due to the above described behavior of lower syngas or H_2 generation (Figure 3.7) compared to thermodynamic equilibrium towards lower C/O ratios, we conclude that with the use of rhodium catalyst, total oxidation is enhanced due to high availability of O_2 on the catalytic surface and overcomes the thermodynamic limit for fuel-lean gas mixtures. A second catalytic effect not considered by thermodynamic equilibrium is the so called sticking effect of the reacting gases, which describes the alkane vs. O_2

competition for catalyst surface sites. As described by Vesper et al. [94], a decrease in fuel concentration in the gas mixture (lower C/O ratios) leads to a stronger site blocking by oxygen on the catalyst surface, hindering the fuel utilization.

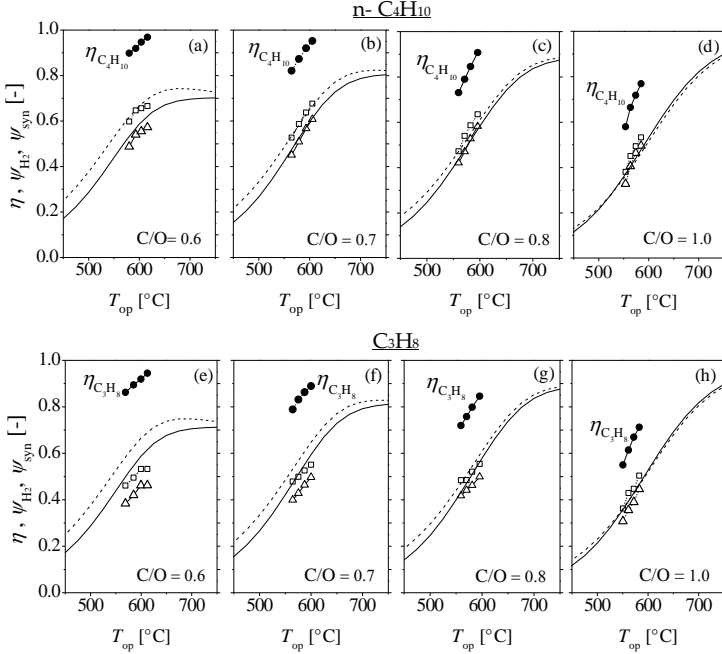


Figure 3.7: Experimental results for both fuels (symbols) compared to thermodynamic equilibrium (dashed lines: ψ_{H_2} ; solid lines: ψ_{syn}) for n-C₄H₁₀, (a)–(d), and C₃H₈, (e)–(h). Fuel conversion is complete at equilibrium.

Table 3.2 summarizes the results obtained at optimal C/O ratios at which syngas yield is the highest for n-C₄H₁₀ and C₃H₈. As tabulated here, the maximum syngas flow generated was 7.17 $\mu\text{mol s}^{-1}$. This amount of the produced syngas corresponds to a power of 1.85 W which is suitable for a micro-SOFC power plant. This power is defined as the outlet mass flow of syngas specie times its lower heating value [97].

Table 3.2: Summary of the gas analysis results and the outlet flow rates of the species of interest at optimal C/O ratio.

			C _x H _y -species		Syngas-species		
n- C ₄ H ₁₀ at C/O = 0.7	Outlet flow rate [$\mu\text{mol s}^{-1}$]		C ₄ H ₁₀	CH ₄	H ₂	CO	syngas
			0.06	0.24	4.43	2.74	7.17
		± 0.01	± 0.01	± 0.14	± 0.11	± 0.13	
Average $\pm \sigma$ [%]		η	X_{CH_4}	ψ_{H_2}	ψ_{CO}	ψ_{syn}	
		95.2	0.18	66.7	51.7	60.0	
		± 0.1	± 0.0	± 0.4	± 0.5	± 0.5	
C ₃ H ₈ at C/O = 0.8	Outlet flow rate [$\mu\text{mol s}^{-1}$]		C ₃ H ₈	CH ₄	H ₂	CO	syngas
			0.31	0.32	4.33	2.50	6.83
		± 0.01	± 0.01	± 0.01	± 0.01	± 0.01	
Average $\pm \sigma$ [%]		η	X_{CH_4}	ψ_{H_2}	ψ_{CO}	ψ_{syn}	
		84.3	0.16	55.4	42.5	49.8	
		± 0.4	± 0.0	± 0.1	± 0.1	± 0.1	

Compared to previous studies on micro-structured reactors, the micro-reactor presented in this study showed very high syngas production at the intermediate temperatures investigated. The partial oxidation of C₃H₈ on micro-structured reactors was studied by Aartun et al. [98,99] and Gjervan et al. [100], where rhodium-alumina catalysts were impregnated on Fecrallow-micro-channeled reactors. Aartun et al. [98] reported C₃H₈ conversion values below 40% and a H₂ and CO volume content in the exhaust gas of < 2% and < 3%, respectively, at a reaction temperature of 600°C. For the same fuel dilution ratio (C/O = 0.8), our results show double C₃H₈ utilization and a H₂ volume content of $17.2 \pm 0.1\%$ and CO volume content of $9.9 \pm 0.2\%$ in the reformed gas. For stoichiometric C₃H₈ CPO conditions, Pennemann et al. [87] achieved almost complete C₃H₈ conversion and H₂ and CO selectivities (S_{H_2} , S_{CO}) of approximately 70% at 700°C on Rh surfaces as well. In the present study at markedly lower temperatures (below 600°C), despite incomplete C₃H₈ utilization, S_{H_2} and S_{CO} values reached $88.9 \pm 0.1\%$ and $63.8 \pm 0.5\%$, respectively. These comparisons confirm the substantial benefits of our

catalytic ceramic-foam filled micro-reactor for syngas production at intermediate temperatures.

Self-sufficient reaction and its effect on syngas yield

In previous section, the performance of the micro-reactor in terms of fuel conversion and syngas yield at different temperatures under continuous heat input was investigated. In this section, the capability of the micro-reactor to sustain a thermally self-sufficient CPO reaction is tested for a volumetric total flow of 60 sccm and C/O = 0.7.

For the exothermic reaction to achieve thermal self-sustainability, we first heated the reactive gas mixture with the two built-in heaters fabricated at the bottom of the carrier (Heater A is located underneath the micro-reactor and heater B is placed prior to reactor inlet, Figure 3.1c). The function of Heater B is mainly to heat up the incoming gas mixture. We used a total power input of 9.4 W and a power distribution of heaters A and B of nearly 1:1. Once the reaction was initiated, which occurred at a reactor temperature between 460 and 475°C, the heaters were turned off (at 485°C). The time lapse between the temperature raise at the entrance of the reactor and the temperature readings at the thermocouples on top of the micro-reactor during the rapid heating phase was the reason for the higher ignition temperature range obtained between these start-up experiments and those in the previous section "Effect of fuel dilutions and set temperature on product composition" (Figure 3.2). The start-up heating method and the resulting temperature are depicted in Figure 3.8, where $T_{carrier}$ represents the temperature at the top of heater B.

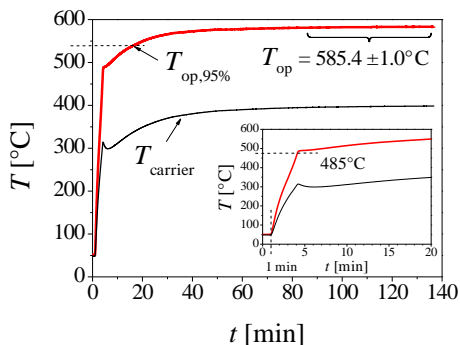


Figure 3.8: Temperature vs. time behavior during reaction activation (from $t = 1$ min until $T = 485^\circ\text{C}$) and thermally self-sustained conditions. $T_{carrier}$ represents the temperature at the top of heater B.

For calculation of the power consumption during start-up, the lower heating value of C_4H_{10} , the $n\text{-C}_4\text{H}_{10}$ inlet flow, the power supplied to reach 485°C and the time spent to achieve 95% of T_{op} were taken into consideration. For our experiment, a total power of 8.5 W was consumed in order to achieve 95% of steady state temperature in Kelvin ($T_{op} = 585.4 \pm 1.0^\circ\text{C}$, $T_{op,95\%} = 542.5^\circ\text{C}$). When compared to [89], where heating times were in the order of 400 s, the heating element in our setup could be substantially improved. For instance, a thin-film heater deposited on the silicon wafer itself would have the potential of being not only faster but also more energy efficient. That in turn makes the fabrication process more difficult.

The gas analysis results for both self-sustained reaction experiments are tabulated in Table 3.3. The exhaust gas was analyzed after 60, 85, 110 and 135 min of reaction. The temperatures of the micro-reactor at which these samples were taken were in the range 581.1°C and 586.4°C .

Table 3.3: Average gas analysis results from runs 1 and 2 after 60, 85, 110 and 135 min of reaction.

	C _x H _y -species		Syngas-species		
	C ₄ H ₁₀	CH ₄	H ₂	CO	syngas
Outlet flow rate [$\mu\text{mol s}^{-1}$]	1.03 \pm 0.01	0.18 \pm 0.01	6.09 \pm 0.03	3.25 \pm 0.03	9.34 \pm 0.03
Average $\pm\sigma$ [%]	η	X_{CH_4}	ψ_{H_2}	ψ_{CO}	ψ_{syn}
	60.9 \pm 0.6	0.07 \pm 0.0	46.1 \pm 0.6	30.7 \pm 0.4	39.1 \pm 0.5

When comparing the results tabulated in Table 3.3 with those obtained during constant heating (section “Effect of fuel dilutions and set temperature on product composition”), the fuel utilization is reduced from over 90% to nearly 60%. Also, ψ_{H_2} , ψ_{CO} and consequently ψ_{syn} decreased by approximately 20%. One reason for the reduced ψ_{syn} was the insufficient heat at the micro-reactor where H₂ generation pathways like steam reforming take place. The strong endothermic steam reforming reaction is known to contribute to higher H₂ and CO production [14,96]. Also, compared to the experiments in section “Effect of fuel dilutions and set temperature on product composition”, no preheating of the inlet gases was possible, which is known to reduce fuel utilization and CO production rate [101]. The second factor affecting the results is t_{space} , which was approximately 21 ms, compared to 40–44 ms in the experiments in section “Effect of fuel dilutions and set temperature on product composition”. As explained in [90], low space times result in lower fuel utilization, as the reactants have less time to be converted.

Because of the very small size of the system, heat losses have been shown to play an important role in the fuel utilization and in the partial oxidation of small-size reactors [101]. We estimate here the heat loss of reaction ($Q_{\text{loss, reaction}}$) at steady state in both testing modes (at C/O = 0.7) from

$$Q_{\text{loss, reaction}} = \sum n_{\text{outlet}} \cdot h_{\text{outlet}}(T_{\text{op}}) - \sum n_{\text{inlet}} \cdot h_{\text{inlet}}(T_{\text{op}}) \quad (3.6)$$

where n_{inlet} and n_{outlet} are the inlet and outlet mole flow rates and $h_{\text{inlet}}(T_{\text{op}})$ and $h_{\text{outlet}}(T_{\text{op}})$ denote the inlet and outlet molar enthalpies at an assumed constant temperature T_{op} . For the continuous heating mode, two different T_{op} values are close to that obtained by the self-sustained mode. The calculated values of

$Q_{\text{loss, reaction}}$ are shown in Table 3.4. In the cases studied here, approximately 4 times more heat is lost in the self-sustained mode. As a consequence, lower fuel utilization and a lower syngas production were obtained. However, in order to determine the optimal operation mode for a steady state reaction, the power supplied from the screen-printed heaters has to be taken into account. For the continuous heating mode at steady state at $T_{\text{op}} = 579^{\circ}\text{C}$ and $T_{\text{op}} = 593^{\circ}\text{C}$, a heating power of 1.9 W and 2.1 W (for $T_{\text{set}} = 375^{\circ}\text{C}$ and $T_{\text{set}} = 400^{\circ}\text{C}$), respectively, was necessary. Employing

$$Q_{\text{loss, total}} = Q_{\text{loss, reaction}} + P_{\text{heater}} \quad (3.7)$$

where P_{heater} is the heating power provided by the built-in heaters, total heat losses $Q_{\text{loss, total}}$ of 2.88 J s^{-1} and 3.06 J s^{-1} are obtained for the continuous heating mode at 579°C and 593°C , respectively. For the self-sustained mode, $Q_{\text{loss, total}}$ equals 1.90 J s^{-1} , which implies a better performance in terms of total heat losses for the reactor system.

Table 3.4: Calculated heat loss for the two testing modes used in this study at $\text{C/O} = 0.7$. $Q_{\text{loss, reaction}}$ is given in J per mole of inlet n-C₄H₁₀ and J per gram of the feed gas, while $Q_{\text{loss, total}}$ is given in total values.

	T_{op} [$^{\circ}\text{C}$]	$Q_{\text{loss, reaction}}$ [$\text{J mol}^{-1}\text{C}_4\text{H}_{10}$]	$Q_{\text{loss, reaction}}$ [$\text{J g}^{-1}\text{feed gas}$]	P_{heater} [J s^{-1}]	$Q_{\text{loss, total}}$ [J s^{-1}]
Continuous heating mode	579	-1.298	-609.8	1.9	-2.877
	593	-1.272	-597.4	2.1	-3.057
Self-sustained mode	585	-5.051	-2371.0	-	-1.900

An important aspect of such a reaction is the controlled production of CH₄. For the self-sustained reaction, production of CH₄ per inlet molar fuel flow was more than halved compared to our results obtained in section “Effect of fuel dilutions and set temperature on product composition” (Table 3.3). Obviously, the lower n-C₄H₁₀ conversion contributed to this drop. Control

over CH₄ production could be possible by enhancing e.g. steam reforming reaction, as discussed previously. In a system where fuel may not be entirely utilized from SOFC membranes for power generation, unconverted gases like CH₄ would need to be consumed completely in a post-combustor in order to avoid exhausting flammable gases to the environment [93]. Combustion of CH₄ may be energy demanding as its concentration in the exhaust gas increases, especially at our intermediate temperature range of interest [102]. According to our results, realizing the CPO reaction at low C/O ratios would be necessary in order to avoid high concentration of CH₄ in the exhaust gas, enhancing at the same time the fuel conversion.

After 280 hours of operation combined, no cracks or other kind of deformations were noticed on neither the micro-reactor bed nor the micro-reactor structure itself, underpinning the very good mechanical stability and reliability of the reactor.

3.5 Conclusion

In this study, the capability of a novel micro-fabricated reactor concept to deliver high syngas yield was investigated by means of partial oxidation of n-butane and propane. The CPO reaction was accomplished by the use of a rhodium doped catalyst embedded inside a foam-like ceramic bed inside the micro-reactor.

Under continuous heating conditions and at $t_{\text{space}} = 40\text{--}44$ ms, the micro-reactor was able to deliver syngas yield as high as 60% for n-butane and 50% for propane for an optimal C/O ratio of 0.7 and 0.8, respectively. Enough syngas (7.2 and 6.8 $\mu\text{mol s}^{-1}$ equivalent to 1.85 W and 1.76 W for n-butane and propane, respectively) was produced to power a micro-SOFC device. These experimental results were shown to be close to thermodynamic equilibrium behavior, especially for the gas mixtures close to stoichiometric partial oxidation conditions.

It was also shown that the micro-reactor is able to reach steady state temperature and syngas production in a thermally self-sustained mode. In this case, however, the syngas yield dropped to 39% for n-butane, due to the insufficient heat through the entire reactor, the higher heat loss by the reactants and the lower residence time. Despite its higher reaction heat loss,

the self-sufficient reaction is proven to be the most efficient heating mode when the total heat loss of the reactor system is taken into account.

The presented micro-reactor bed demonstrated a good thermal and catalytic stability through all experiments. Overall, the catalytic results of this study prove the suitability of this novel micro-reactor for delivering high conversion of fuel and high syngas yields. In addition to its generic value, the present micro-reactor was fabricated and investigated with the additional aim of being integrated with a micro-SOFC membrane and a post-combustor to piece together a first of its kind portable micro-SOFC power plant.

4 Comparison of flame-made rhodium on Al_2O_3 or $\text{Ce}_{0.5}\text{Zr}_{0.5}\text{O}_2$ supports for the partial oxidation of methane

Parts of this chapter have been submitted for publication:

A. J. Santis-Alvarez, R. Büchel, N. Hild, W. Stark, and D. Poulidakos, "Comparison of flame-made rhodium on Al_2O_3 or $\text{Ce}_{0.5}\text{Zr}_{0.5}\text{O}_2$ supports for the partial oxidation of methane," *submitted for publication*, 2013.

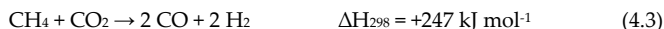
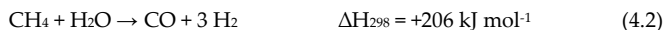
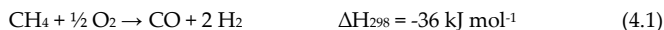
Abstract

Catalytic partial oxidation of methane (CPOM) was investigated for rhodium supported on Al_2O_3 and on $\text{Ce}_{0.5}\text{Zr}_{0.5}\text{O}_2$. The catalysts were synthesized by flame spray pyrolysis and characterized by nitrogen adsorption, transmission electron microscopy and X-ray diffraction. The $\text{Rh}/\text{Al}_2\text{O}_3$ catalysts exhibited an enhanced and stable CPOM activity compared to $\text{Rh}/\text{Ce}_{0.5}\text{Zr}_{0.5}\text{O}_2$. Syngas formation was promoted for 0.5 wt% Rh on Al_2O_3 close to the calculated thermodynamic equilibrium, outperforming 1 wt% $\text{Rh}/\text{Ce}_{0.5}\text{Zr}_{0.5}\text{O}_2$ in the temperature range 525–750°C. A proposed mechanism of the effect of support on Rh activity is discussed in terms of oxygen transport capacity of the support materials. Further, high oxygen concentrations showed that Al_2O_3 is a better support compared to $\text{Ce}_{0.5}\text{Zr}_{0.5}\text{O}_2$. This is attributed to the fact that the Al_2O_3 support inhibits Rh oxidation and therefore allows the presence of Rh in its metallic state, which is preferable for high syngas formation. After thermal treatment of the catalysts, the catalytic effectiveness of Rh was more than 5 times higher for Al_2O_3 than for $\text{Ce}_{0.5}\text{Zr}_{0.5}\text{O}_2$ supports.

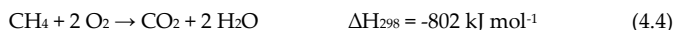
4.1 Introduction

Catalytic hydrocarbon-to-syngas conversion by exothermic partial oxidation (equation 4.1) is superior from the standpoint of energy efficiency, compared to endothermic steam reforming (equation 4.2) and dry reforming (equation 4.3) [28,103]. Among all hydrocarbons and according to reaction route

(equation 4.1) and thermodynamic equilibrium [28], methane delivers the highest possible H₂/CO ratio and the highest concentration of H₂, which are important for syngas applications like the Fischer-Tropsch process [103-106] and other applications such as e.g. solid oxide fuel cells [11,54,107].



Rhodium has been described as the most efficient noble metal for the catalytic partial oxidation of methane (CPOM) [28]. During CPOM it is currently assumed that Rh undergoes a redox process [108,109], following an indirect syngas formation route through reactions (1)–(4): The oxidized metallic phase enhances total oxidation (equation 4.4) at the reactor inlet, while the metallic state facilitates downstream reactions such as (1,2,3) [83,110].



Therefore, the formation and presence of reduced supported Rh metal seems to be preferable for high H₂ and CO production during CPOM. Reduced noble metal can be formed and stabilized by the choice of the support [111,112], enhancing the catalytic performance.

For Rh, commonly Al₂O₃, CeO₂ and Ce_{0.5}Zr_{0.5}O₂ are used as supports for CPOM [29]. By doping CeO₂ with ZrO₂, a thermally resistant structure with high oxygen storage and transport properties is obtained [113-115]. While Al₂O₃ showed low lattice oxygen mobility [116,117], the high oxygen mobility of CeO₂ and especially Ce_{0.5}Zr_{0.5}O₂ enabled the exchange of lattice oxygen ions with the reactive gases [118,119] and supported noble metals [117]. Because of the intrinsic oxygen transport capacity, CeO₂ [120] and Ce_{0.5}Zr_{0.5}O₂ [121-125] have proved to be adequate supports for Rh for steam reforming (see equation 4.2). Similarly, CeO₂ [126] and Ce_{0.5}Zr_{0.5}O₂ [127] enhanced catalytic dry reforming of CH₄ (see equation 4.3). Both steam and dry reforming are known to promote syngas formation during CPOM [83].

The catalytic performance of Rh/Al₂O₃, its metallic dispersion and thermal stability were enhanced by doping with CeO₂ (20%) [128] and especially

$\text{Ce}_{0.5}\text{Zr}_{0.5}\text{O}_2$ (5%) [129]. Eriksson et al. [130] showed that Rh on $\text{Ce}_{0.5}\text{Zr}_{0.5}\text{O}_2$ was more effective for CPOM compared to Al_2O_3 supports. Recently, CPOM activity was promoted by the much higher redox potential of the $\text{Ce}_{0.5}\text{Zr}_{0.5}\text{O}_2$ support with and without Rh compared to Al_2O_3 [131]. In contrast to these studies, Ruckenstein and Wang [116] showed that Al_2O_3 was a more adequate support for Rh for CPOM compared to CeO_2 or ZrO_2 supports. It was suggested that the number of active Rh sites decreased on CeO_2 and ZrO_2 due to oxygen migration from the support to Rh metal, causing a decrease in catalytic activity. In the same study however, much lower specific surface areas (SSA) were obtained for both ceria and zirconia supports compared to alumina support.

To date, no definitive agreement has been reached as to which support material is more suitable for effective Rh activity during CPOM. Therefore, we investigate and compare the role of the supports Al_2O_3 and $\text{Ce}_{0.5}\text{Zr}_{0.5}\text{O}_2$ on the activity of Rh for CPOM. For this, the catalysts are synthesized by means of flame spray pyrolysis (FSP) method, a one-step synthesis technique of catalytic materials which allows high metal dispersions on the support at the nanoscale [132,133]. By varying the Rh metal loading from 0.5 wt% to 5 wt%, operation temperatures (from 250°C to up to 750°C) and fuel dilution from 28.6% to 13.8%, the activity for CPOM and the performance stability of Rh are investigated and definitive findings are presented on the effects of the Al_2O_3 and $\text{Ce}_{0.5}\text{Zr}_{0.5}\text{O}_2$ supports.

4.2 Experimental methods

Preparation

With a flame spray pyrolysis (FSP) unit, catalysts with 0.5–5 wt% Rh on either Al_2O_3 or $\text{Ce}_{0.5}\text{Zr}_{0.5}\text{O}_2$ support were prepared in a single synthesis step. A combustible precursor containing the metals in the desired ratios were pumped through a capillary (Hamilton 0.41 mm inner diameter) at 5 mL min⁻¹ and dispersed into a fine spray with an oxygen flow of 5 L min⁻¹. The pressure drop of the oxygen over the nozzle was 2 bar. To ignite the spray a premixed CH_4/O_2 flame at a volume ratio of 1/2 was used [134]. For the precursor with Al, aluminum-tri-*sec*-butoxide (Fluka, 95%) was dissolved in a 2:1 vol. ratio of diethylene glycol monobutyl ether (Fluka, 98%) and acetic anhydride (Riedel-

de Haën, 99%). The aluminum concentration was kept constant at 0.5 mol L⁻¹. For the CeZr-precursor solution, Ce 2-ethylhexanoate (Strem, 98%) and Zr 2-ethylhexanoate (Strem, 98%) were dissolved with a Ce to Zr ratio of 1 in xylene (Riedel-de Haën, 95%) resulting in a metal concentration of 0.5 mol L⁻¹. Similarly, Rh(III)-acetylacetonate (Sigma-Aldrich, 99.99%) was added to the Al- or CeZr-precursor. Note that the flame-made catalysts were not subjected to an additional temperature pretreatment as usually applied for conventionally prepared catalysts. However, for some experiments sintering effects during conventional post-treatment steps on our samples were simulated for all catalysts by adding a sintering step in air at 800°C for 4 h.

In the notation used here, the Rh content is given as mass percentage of the catalyst and is denoted prior to its elemental symbol. The Al₂O₃ and Ce_{0.5}Zr_{0.5}O₂ supports are abbreviated as Al and CeZr, respectively. Therefore, a catalyst with a Rh loading of 1 wt% on the support Al₂O₃ or Ce_{0.5}Zr_{0.5}O₂ is written as 1RhAl or 1RhCeZr, respectively.

Characterization

Nitrogen adsorption–desorption isotherms were measured at 77 K using a Micromeritics Tristar instrument. The BET method was used to determine the specific surface area (SSA) by a 5-point nitrogen adsorption isotherm. The estimated accuracy is ± 3%. X-ray diffraction (XRD) patterns were recorded with a Bruker D8 Advance instrument (40 kV, 40 mA, $\lambda = 0.154$ nm). Crystallite sizes were calculated using the fundamental parameter approach and the Rietveld method with the TOPAS 3 software at ± 10% accuracy [135].

For scanning transmission electron microscopy (STEM), the catalyst material was dispersed in ethanol and deposited onto a perforated carbon foil supported on a copper grid (Okenshoji Co. Ltd.). The STEM images were obtained with a high-angle annular dark-field (HAADF) detector attached to a Tecnai 30F microscope (FEI; field emission cathode, operated at 300 kV), showing the metal particles with bright contrast (Z contrast).

Activity measurements

The CPOM process was investigated in a fixed-bed flow micro-reactor at atmospheric pressure. The reactor, a quartz tube of 5 mm inner diameter, was placed in an electric furnace (MTF 12/38/250, Carbolite). The catalyst (5 mg) was mixed with calcined sand (200 mg, Riedel-de Haën, average diameter: 200

μm) and fixed in position in the reactor with quartz glass wool. A total volumetric flow of 21 mL min^{-1} was used. The transient activity behavior was measured between 200°C and 750°C , using a stoichiometric mixture for the CPOM reaction. The fuel dilution was calculated according to equation 4.1 and the relationship $C/O = 0.5 \cdot x_{\text{CH}_4} \cdot x_{\text{O}_2}^{-1}$, with x_i representing the molar fraction of CH_4 and oxygen, and $C/O = 1.0$ referring to stoichiometric partial oxidation ratio (28.6% CH_4 , 14.3% O_2 in N_2). The ignition of the CPOM reaction was accompanied by a sudden temperature jump ($\pm 10^\circ\text{C}$) due to the exothermic reaction and was measured by a thermocouple inserted in the middle of the reactor at $\pm 3^\circ\text{C}$ accuracy. The effluent gas stream composition was measured by gas chromatograph equipped with a thermal conductivity detector (6890 GC, with a HP-PlotQ column, Agilent). The carbon mass balance always closed higher than 97%. The standard deviations and errors derived from repeated measurements were less than 4% and are therefore not shown explicitly in the figures.

The CPOM performance was measured in terms of CH_4 conversion, syngas yield and molar fractions of CH_4 , H_2 and CO in the outlet gas stream. The syngas yield was defined as $\psi_{\text{syn}} = 100 \cdot (n_{\text{H}_2} + n_{\text{CO}})/3$, where n is the total amount of moles of a substance.

4.3 Results and discussion

Characterization

Flame spray pyrolysis of the precursor mixture yielded nanoparticles in the nm size range. BET measurements (Table 4.1) revealed high specific surface areas (SSA) for the support materials and Rh-containing samples between $182 \text{ m}^2 \text{ g}^{-1}$ and $132 \text{ m}^2 \text{ g}^{-1}$. Sintering the samples at 800°C for 4 h resulted in lower SSA values for all samples. The loss in SSA was more pronounced for Rh supported on CeZr than on Al. In Figure 4.1, STEM pictures of the flame-made catalysts 2RhAl and 2RhCeZr are shown. In Figure 4.1A and B, the Rh clusters are discernible as bright, spherical dots on the spherical Al support. The CeZr support in the 2RhCeZr sample (Figure 4.1C and D) exhibits a highly regular, crystalline, sharp-edged structure. No metallic rhodium particles were visible on CeZr because of the high contrast of Ce ($Z_{\text{Ce}} = 58$) compared to Rh ($Z_{\text{Rh}} = 45$).

Table 4.1: Specific surface area of reference supports and Pd-catalysts after preparation (as-prepared) and cycling in air (sintered).

Catalyst or support	BET [$\text{m}^2 \text{g}^{-1}$], as-prepared	BET [$\text{m}^2 \text{g}^{-1}$], sintered
Al	168	153
0.5RhAl	154	149
1RhAl	180	154
2RhAl	182	158
CeZr	132	79
1RhCeZr	149	91
2RhCeZr	129	89
5RhCeZr	145	90

The XRD pattern of all as-prepared catalysts and sintered 2RhAl and 2RhCeZr is shown in Figure 4.2. The loading and the cluster size of Rh are too small and therefore only the support materials could be detected. The Rh loading did not change the support characteristics and a crystal size of 6 nm for Al_2O_3 and 6 nm for $\text{Ce}_{0.5}\text{Zr}_{0.5}\text{O}_2$ was measured. After sintering the samples at 800°C in air for 4 h, the crystal structure did not change significantly (sintered crystal size 6.4 nm) and again no Rh clusters were detected. Only for sintered 2RhAl, the Al(220) plane grew from 6 nm to 23 nm.

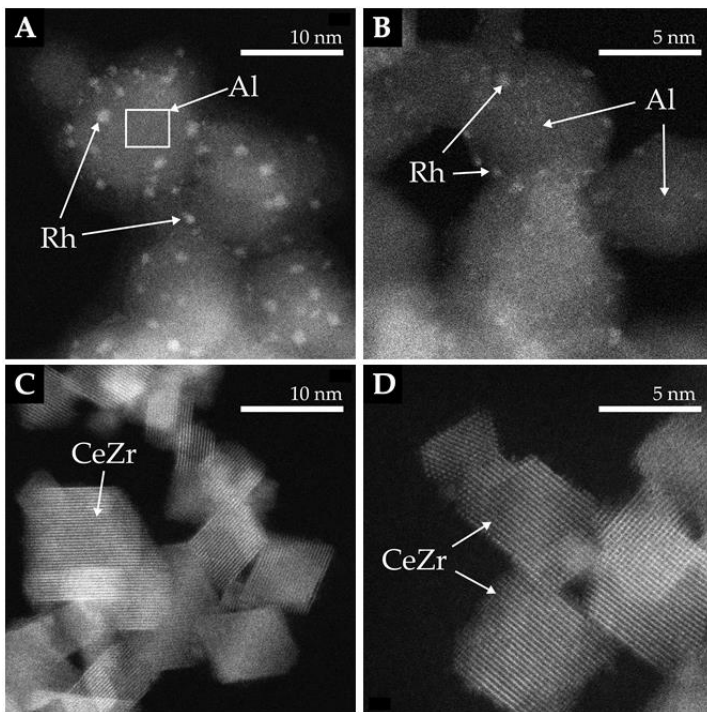


Figure 4.1: STEM images of 2RhAl and 2RhCeZr. A: as-prepared 2RhAl; B: sintered 2RhAl at 800°C for 4 h; C: as-prepared 2RhCeZr; D: magnification of as-prepared 2RhCeZr.

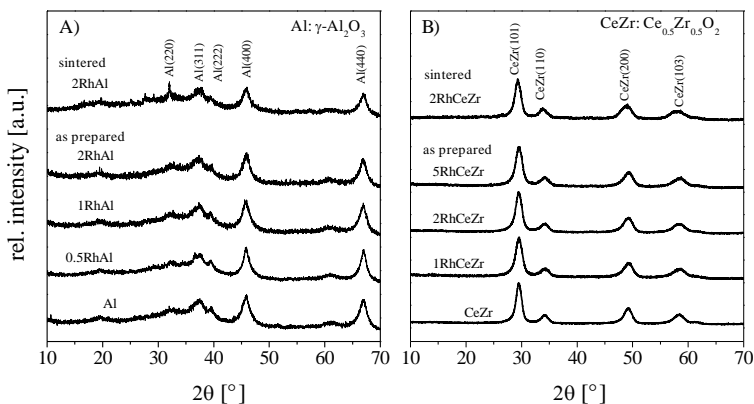


Figure 4.2: XRD pattern of as-prepared and sintered catalysts with Rh loadings from 0 to 5.0 wt%. The characteristic reflections of the support are indicated in A) for Al₂O₃ (ICSD: 39014) and in B) Ce_{0.5}Zr_{0.5}O₂ (ICSD: 164608).

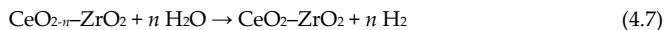
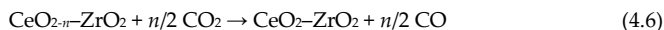
Ignition and hysteresis behavior of the CPOM

The ignition and extinction characteristics during CPOM between 250°C and 450°C for 2RhAl and 2RhCeZr are shown in Figure 4.3. With the ignition, simultaneous H₂ and CO formation and also complete oxygen conversion is observed in the product stream. For 2RhCeZr and 2RhAl, CPOM ignition occurred at 357°C and 401°C, respectively. Therefore, CeZr support promoted syngas production at lower temperatures than Al. The ignition temperature was similar to that of C₃H₆ for a flame-made Pt/CeO₂ catalyst [136]. The CeZr and the Al catalysts showed a hysteresis upon cooling, leading to extinction around 320°C and 330°C for 2RhCeZr and 2RhAl, respectively.

Prior to ignition and after extinction, only small amounts of CH₄ and oxygen were consumed and CO₂ and H₂O were formed for both catalysts (data not shown). Conversion of CH₄ (Figure 4.3, see below) and formation of CO₂ and H₂O prior to CPOM reaction ignition is expected from thermodynamic equilibrium calculations [28] and was slightly higher for 2RhCeZr than for 2RhAl.

Ignition and extinction temperatures were correlated to the oxidation state of Rh. Grundwaldt et al. [108] and Hannemann et al. [109] showed that

oxidized Rh promoted formation of CO₂ and H₂O prior to reaction ignition and after reaction extinction. After reaction ignition on partially reduced Rh, formation of CO₂ and H₂O was obtained on oxidized Rh within the reactor entrance region, whereas syngas formed on reduced Rh further downstream of the reactor [108,109]. In the present study, H₂ and simultaneous CO formation on RhCeZr at lower temperatures than on RhAl can be explained with a combination of two mechanisms: First, CeZr promotes oxygen transport to and from the Rh surface enabling an oxidation-reduction process of the metal at lower temperatures compared to Al. Thus, formation of reduced Rh sites on the surface is facilitated contributing to lower temperature CPOM ignition. Second, CeZr formed H₂ and CO directly through redox reactions as shown in Table 4.2, where Rh-free CeZr support formed syngas at 675°C and 750°C. The redox reactions mechanisms involved during the CPOM on CeZr are similar to [128,137,138] and [118] as follows:



where the reduced form of Ce in the CeZr support is represented by Ce³⁺ ($n = 0.5$) or as mixed oxide as in [60] by Ce^{3+/Ce⁴⁺} ($n < 0.5$). Support Al (Table 4.2) did not form syngas and was practically inactive in terms of CH₄ conversion when compared to results from the homogenous reaction i.e. without support material.

Table 4.2: Conversion of CH₄ (Conv.CH₄) and volumetric content of H₂ at the exit of the reactor for Rh-free supports CeZr and Al. The CPOM was conducted at stoichiometric condition.

Support	600°C		675°C		750°C	
	Conv.CH ₄ , %	%H ₂ ^a	Conv.CH ₄ , %	%H ₂	Conv.CH ₄ , %	%H ₂
Al	5.0	0.0	5.7	0.0	8.7	0.0
CeZr	8.3	0.0	14.5	1.2	18.7	3.1
None ^b	4.8	0.0	5.3	0.0	8.0	0.0

^a $x\text{H}_2 \cdot 100\%$.

^b Homogenous reaction.

Figure 4.3 shows that at temperatures higher than 400°C, once reaction was ignited on 2RhAl, H₂ and CO concentrations exceeded those obtained from 2RhCeZr. This higher performance indicates that RhAl is more effective towards CPOM despite higher oxygen-exchange rates by the CeZr support, as suggested by equations 4.5–4.7 and Table 4.2. For both supports, the syngas production was slightly higher during the cooling ramp compared to the same oven temperatures during the heating phase. This hysteresis effect is due to a kinetically suppressed re-oxidation of Rh metal caused by structural changes and/or catalyst overheating because of hot-spot formation [109].

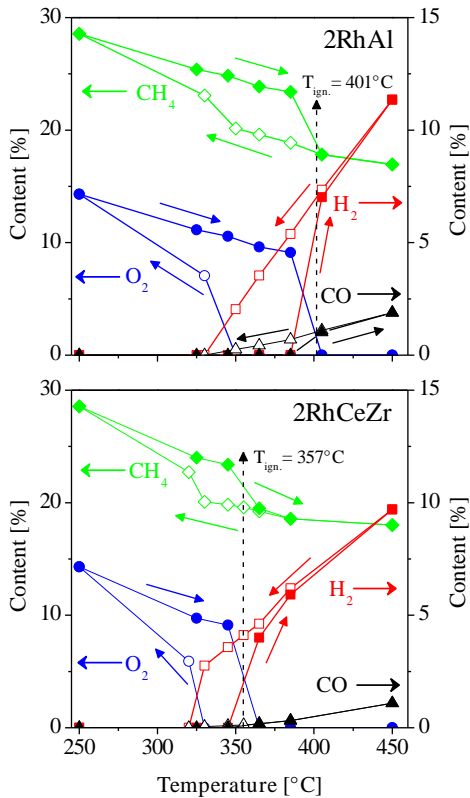


Figure 4.3: The concentrations of CH_4 , O_2 , H_2 and CO are shown for the CPOM reaction during heating (full symbols) and cooling (empty symbols) over 2Rh on either CeZr or Al support.

Temperature dependence of the catalytic activity

Figure 4.4 shows the CPOM performance of 2RhAl at different temperatures and compares it to the calculated equilibrium (dashed line). In general, the catalytic performance was very close to equilibrium. In line with CPOM activity of 2RhAl, higher H_2 and CO molar fractions (x_{H_2} and x_{CO} ,

respectively) and syngas yield (ψ_{syn}) were obtained at higher temperatures for all catalysts, in agreement with calculated equilibrium.

To highlight the differences in performance as a function of the support (Al or CeZr), catalysts with different Rh loadings were tested at selected temperatures. Table 4.3 summarizes the ignition temperatures and the CPOM performance of the different catalysts in terms of the volumetric H₂ content at the exit of the reactor (%H₂). For both supports, ignition temperatures decreased with increasing Rh loading, which is in accordance with pertinent literature [109,139]. Also, at constant Rh loading, CeZr support showed lower ignition temperatures compared to Al.

Despite the absence of a significant difference in CPOM performance above 525°C for catalysts with high Rh loadings (1RhAl, 2RhAl, 2RhCeZr, 5RhCeZr), a difference in reaction performance was discernible for 0.5RhAl and 1RhCeZr: The CPOM performance of 0.5RhAl was not only higher compared to 1RhCeZr, but also close to that of 1RhAl, showing a remarkable improvement in effective Rh usage on Al over CeZr. For constant Rh loadings, the ratio between produced H₂ and CO per converted CH₄ molecule was always higher for Al support compared to CeZr.

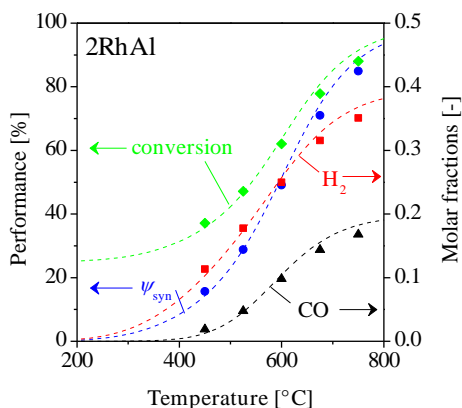


Figure 4.4: Catalytic activity of 2RhAl between 200 and 800°C. The dashed lines represent calculated equilibrium concentrations.

Table 4.3: Ignition temperature and volumetric H₂ content at the exit of the reactor for different Rh loadings on either Al or CeZr support. Stoichiometric condition was used for these experiments.

Catalyst	T _{ign.} ^a [°C]	375°C %H ₂ ^b	450°C %H ₂	525°C %H ₂	600°C %H ₂	675°C %H ₂	750°C %H ₂
2RhAl	401	0.0	11.4	17.8	25.0	31.5	35.1
1RhAl	425	0.0	9.7	17.6	24.4	31.4	34.5
0.5RhAl	517	0.0	0.0	15.5	23.9	30.3	34.5
5RhCeZr	328	5.9	11.7	17.8	25.1	31.5	35.2
2RhCeZr	357	5.5	9.7	16.6	24.9	30.8	34.6
1RhCeZr	412	0.0	4.5	14.4	21.5	29.0	32.9
equilibrium	262 ^c	5.1	10.3	17.4	25.7	32.8	36.8

^a Measured with a thermocouple in the catalysts' bed.

^b xH₂ ·100%.

^c Equilibrium temperature at which %H₂ equals 1.0%.

In Figure 4.5, a sketch of the proposed reaction mechanism is shown. Prior to ignition, the oxidized metallic state (Rh₂O₃) is predominant throughout the entire reactor. After ignition, oxidized Rh is mostly found at the reactor inlet (box A) and the metallic state is predominant further downstream of the reactor (box B) [108].

In RhCeZr samples, CeZr exchanges oxygen ions with Rh metal by means of redox process. Such oxygen ion transport may impede complete reducibility of Rh, causing lower CPOM performance than Rh on Al support (box B). Simultaneously, CeZr lattice oxygen ions may interact with the reactants possibly by means of a spillover effect, promoting CPOM at a lower extent than on Rh containing Al (see Table 4.2). Such a spillover effect was already proposed by Salazar-Villalpando et al. [117], who studied the role of lattice oxygen of Al and CeZr support on the CPOM by means of isotopic studies. They concluded that lattice oxygen ions from the CeZr support selectively oxidized CH₄ to produce CO. In the same study, the addition of Rh clearly catalyzed the oxidation rate, likely due to an oxygen spillover effect from the metal particles to the support, while no such spillover effect was found on the Al support. According to the results shown here, formation of H₂ and CO was enhanced for higher Rh loadings on CeZr suggesting that the spillover effect is weakened and hence more metallic Rh surface is available for H₂ and CO formation. On Al support, metallic Rh is more promoted than

on CeZr, making high production of H₂ and CO viable already at low Rh loadings.

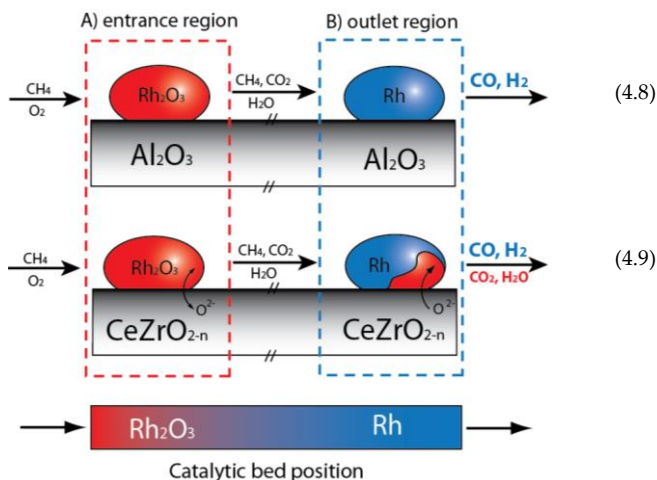


Figure 4.5: Scheme of difference between CeZr and Al support on Rh and CPOM activity. CeZr exchanges oxygen ions with Rh metal by means of a redox process involving Ce components. The reduced form of Ce in the CeZr support is represented by Ce³⁺ ($n = 0.5$) or as mixed oxide as in [60] by Ce³⁺/Ce⁴⁺ ($n < 0.5$).

Stability at constant operation temperatures

Long term stability is a crucial issue of CPOM during reaction conditions and it can only be reached when minimizing the sintering of the noble metals. To investigate the catalytic stability, measurements were performed for all samples for 10 h using stoichiometric CPOM conditions at 600°C. Figure 4.6 depicts the results obtained for the 1RhAl and 1RhCeZr samples. CPOM capability decreased continuously over 1RhCeZr whereas for 1RhAl, activity remained constant throughout the entire testing period. A reason for this behavior could be the permanent oxidation of the active Rh surface driven by the CeZr support. Under the same testing conditions, no drop in CPOM performance was identified for all other samples. Similarly flame-made RhAl showed stable performance also for NO_x reduction [140].

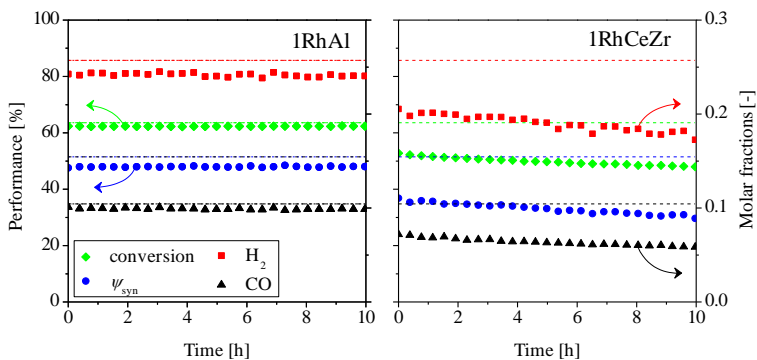


Figure 4.6: Catalytic performance over 1Rh on either CeZr or Al support during a period of 10 h at 600°C and stoichiometric dilution. The dashed lines represent performance at calculated equilibrium.

Effect of fuel dilution on catalytic performance

The effect of varying oxygen concentrations, i.e. fuel dilution, at the reactor inlet on CPOM performance was investigated for Rh on Al or CeZr support. Figure 4.7 shows the results obtained for 2RhCeZr and 2RhAl at C/O from 1.0 to 0.4. Over the entire range, 2RhAl shows a better performance compared to 2RhCeZr. As shown here, x_{H_2} and x_{CO} values for all catalysts decreased with increasing oxygen concentrations whereas CH_4 conversion increased, as expected from thermodynamic equilibrium. The optimal dilution for highest ψ_{syn} was found at C/O = 0.6 for all catalysts and was in close agreement with equilibrium (C/O = 0.5). A higher deviation from the equilibrium can be observed at C/O = 0.6 compared to 1.0, as shown in Figure 4.8. At this optimum C/O value, Rh on Al support showed higher effectiveness compared to Rh on CeZr: 1RhAl and 0.5RhAl showed, respectively, a higher CPOM activity than 2RhCeZr and 1RhCeZr, and the fuel conversion and ψ_{syn} increased in the sequence 1RhCeZr < 0.5RhAl < 2RhCeZr ≤ 1RhAl = 2RhAl = 5RhCeZr.

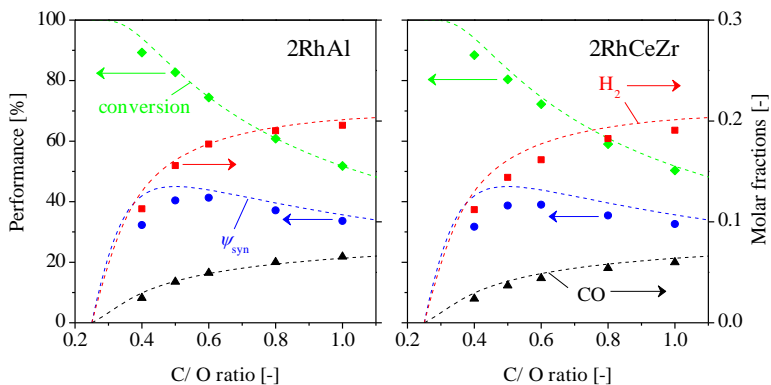


Figure 4.7: CPOM results over 2RhAl and 2RhCeZr for different fuel dilutions. The dashed lines represent calculated equilibrium.

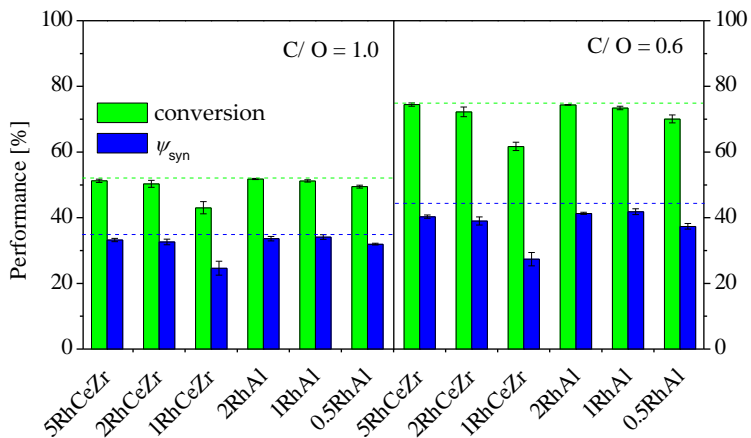


Figure 4.8: Comparison of ψ_{syn} and CH_4 conversion at 550°C for C/O = 1.0 and 0.6 with different Rh loadings on CeZr or Al support. The dashed lines represent calculated equilibrium behavior.

The reason for continuous decrease in syngas production compared to equilibrium for higher oxygen concentrations is twofold: First, mass transfer of CH_4 to catalyst surface becomes limiting at higher fuel dilutions. Such a mass transfer limitation is constant for the experiments, as all samples were tested under equal conditions. Second, the oxidation state or the amount of adsorbed oxygen on the Rh surface can be directly affected by varying oxygen concentration. As demonstrated by Wang et al. [141], high oxygen concentrations increase the amount of adsorbed oxygen on Rh, thus inhibiting CH_4 adsorption. In other words, higher oxygen concentrations at reactor inlet hinder the Rh reducibility and shift the CPOM performance of all samples towards less H_2 and CO production.

The effect of high fuel dilutions on the CPOM on the two supports is depicted in Figure 4.9, where the ψ_{syn} obtained over Al and CeZr supports containing either 1Rh or 2Rh is plotted against the C/O ratio. Here, the difference of the experimental results from equilibrium is plotted for every dilution. For the comparison, all values were corrected by the difference between calculated equilibrium and experimental results at stoichiometric conditions. Therefore, values at C/O = 1.0 are equal zero. A clear decrease in performance is discernible for higher fuel dilutions, especially for the 1RhCeZr sample, caused in part by the decrease in performance over time already shown in Figure 4.6. No significant difference was identified for samples having Al as support, showing that the decrease in performance was almost constant when relativized to stoichiometric results. The decrease in CPOM effectiveness was more pronounced for the CeZr samples. This could derive from excessive oxygen spillover and consequent active site blocking, as proposed in the scheme of Figure 4.5.

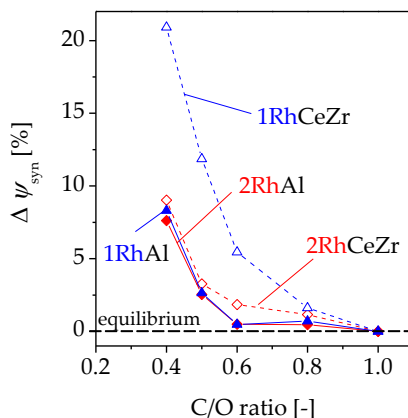


Figure 4.9: Difference of ψ_{syn} to equilibrium for different fuel dilutions at 550°C.

CPOM performance after thermal treatment of catalysts

So far, all catalysts were tested as-prepared without any post-treatment, in contrast to conventional synthesis methods, like impregnation or precipitation synthesis, that require calcination at temperatures as high as 800°C for 4 to 5 hours [103,116,120,142]. In order to intensify sintering effects during reaction conditions and simulate conventional post-treatment steps on our samples, all catalysts were sintered in air at 800°C for 4 h. The resulted ignition temperatures and %H₂ values of the CPOM at different temperatures are listed in Table 4.4 (with the exception of 1RhCeZr¹). All ignition temperatures increased for both supports, especially on Al, when compared to the results listed in Table 4.3. The difference in ignition temperatures from the fresh and the thermally treated samples was higher for increasing Rh loadings e.g. 89°C

¹ We omitted the testing of sintered 1RhCeZr because of the obtained instability over time in previous experiments.

and 67°C for 5RhCeZr and 2RhCeZr, respectively, and the CeZr support remained more active at lower temperatures than Al.

The sintering step led to a substantial performance decrease for all CeZr supported catalysts. CPOM performance decrease by crystal structure changes in the CeZr support can be neglected, as shown in Figure 4.2. As shown in Table 4.1, the decrease in CPOM performance for RhCeZr was likely caused by the higher loss in SSA compared to RhAl catalysts. Compared to the results in Table 4.3, differences between catalytic performance were higher and CPOM performance increased in the order 0.5RhAl < 2RhCeZr < 5RhCeZr < 1RhAl < 2RhAl. In spite of the sintering step, 2RhAl showed performance almost as high as the as-prepared sample. The difference in performance between the 2RhAl and 1RhAl samples became almost negligible at the highest temperature investigated (750°C). Remarkably, the Al sample with only 1 wt% of Rh clearly outperformed the CeZr sample with a 5 times higher Rh loading, emphasizing the performance superiority for Al over CeZr supported Rh for the CPOM reaction.

Table 4.4: Selected catalytic results for different Rh loadings on Al or CeZr support after thermal treatment at 800°C for 4 h (ignition temperature and volumetric H₂ content at the exit of the reactor). Stoichiometric condition was used for these experiments.

Catalyst	T _{ign.} ^a [°C]	525°C %H ₂ ^b	600°C %H ₂	675°C %H ₂	750°C %H ₂
2RhAl	544	0.0	24.4	31.8	34.3
1RhAl	571	0.0	22.7	31.3	34.0
0.5RhAl	617	0.0	0.0	11.1	12.4
5RhCeZr	417	10.0	18.4	28.1	33.4
2RhCeZr	425	8.4	14.1	23.3	32.8
equilibrium	262 ^c	17.4	25.7	32.8	36.8

^a Measured with a thermocouple in the catalysts' bed.

^b xH₂ ·100%.

^c Equilibrium temperature at which %H₂ equals 1.0%.

4.4 Conclusion

The effect of flame-made Al_2O_3 or $\text{Ce}_{0.5}\text{Zr}_{0.5}\text{O}_2$ supports on Rh activity was investigated for the process of catalytic partial oxidation of methane (CPOM).

The performance of Rh catalysts was strongly affected by the support, inlet oxygen concentration and thermal treatment prior to testing. Despite lower CPOM ignition temperatures on Rh/ $\text{Ce}_{0.5}\text{Zr}_{0.5}\text{O}_2$ catalysts at stoichiometric conditions, Rh on Al_2O_3 support showed always higher catalytic activity after ignition at constant Rh loading, also at higher inlet oxygen concentrations. In contrast, we propose that production of syngas on Rh/ $\text{Ce}_{0.5}\text{Zr}_{0.5}\text{O}_2$ was limited because of continuous re-oxidation of metallic Rh by oxygen spillover from the support. Remarkably, CPOM effectiveness was higher for sintered 1 wt% Rh/ Al_2O_3 compared to sintered 5 wt% Rh/ $\text{Ce}_{0.5}\text{Zr}_{0.5}\text{O}_2$, underpinning the superiority in performance and stability of flame-made Al_2O_3 supported Rh.

5 The effect of deposition locality of flame-made Pd on a mixed $\text{Al}_2\text{O}_3\text{-Ce}_{0.5}\text{Zr}_{0.5}\text{O}_2$ support on methane combustion

Parts of this chapter have been submitted for publication:

A. J. Santis-Alvarez, R. Büchel, P. Rüdlinger, F. Krumeich, and D. Poulidakos, "The effect of deposition locality of flame-made Pd on a mixed $\text{Al}_2\text{O}_3\text{-Ce}_{0.5}\text{Zr}_{0.5}\text{O}_2$ support on methane combustion," *submitted for publication*, 2013.

Abstract

The controlled deposition of Pd catalyst on either the Al or the CeZr sites of mixed $\text{Al}_2\text{O}_3\text{-Ce}_{0.5}\text{Zr}_{0.5}\text{O}_2$ supports was possible employing a two-nozzle flame spray pyrolysis (FSP) unit. These catalysts allowed the investigation of the influence of such preferred Pd locality on the catalytic combustion of methane. The performance of the catalysts was indeed dependent on the position of Pd on the supports, strongly affected the oxidation state of the noble metal. During the temperature cycling experiments between 200 and 900°C, Al_2O_3 promoted the stabilization of catalytically active PdO so that Pd on Al_2O_3 exhibited the highest CH_4 conversion. Pd on $\text{Ce}_{0.5}\text{Zr}_{0.5}\text{O}_2$ showed low hysteresis but low activity despite efficient oxygen spill-over from $\text{Ce}_{0.5}\text{Zr}_{0.5}\text{O}_2$ to Pd thus promoting formation, but not stabilization, of highly active PdO. At constant temperatures (450 and 530°C), the best performance was unexpectedly observed if Pd is situated on the Al_2O_3 part of the mixed support. The catalysts were characterized by nitrogen adsorption, X-ray diffraction, and scanning transmission electron microscopy combined with energy-dispersive X-ray spectroscopy.

5.1 Introduction

The catalytic total oxidation process of methane has attracted significant environmental and technological interest due to the combination of high energy content and low CO_2 emissions per mole of fuel (equation 5.1)

[32,33,143,144]. For homogeneous combustion, temperatures above 1100°C are needed, leading to the formation of toxic NO_x and CO as byproducts. Lowering the oxidation temperature using a catalyst can help to avoid the formation of these undesired byproducts [145]. Decrease in temperature is especially interesting for intermediate temperature solid oxide fuel cell (SOFC) systems (< 750°C) [1,16]. In e.g. the so-called ONEBAT system [1], a post-combustor is introduced after the SOFC component to oxidize unused CO, H₂, CH₄ and C₄H₁₀ previously generated by a reformer [146]. Here, CH₄ is the least reactive and thus most stable molecule exiting the SOFC system.



In early studies of low temperature catalytic CH₄ combustion, Pd was reported to be the most active species [147]. The activity of the noble metal, however, is known to decrease during long-term CH₄ combustion [32,148]. Investigations aiming at understanding the behavior of Pd on Al₂O₃ support during oxidation showed that CH₄ combustion activity is maximized on PdO, or coexisting PdO and partially oxidized PdO_x species rather than on metallic Pd [31,149-151]. Van Vegten et al. [149] found that the reduction of active PdO into the less active metallic Pd phase occurred at temperatures as low as 580°C and led to a decrease in CH₄ combustion activity. The re-oxidation process Pd → PdO occurs during cooling, at lower temperatures than those needed for PdO reduction, thus resulting in a hysteresis behavior of the CH₄ conversion. Despite the thermodynamically governed PdO ↔ Pd redox process [152], the stabilization of PdO and the re-oxidation of Pd can be strongly influenced by the support material [32,143].

An addition of metal oxides with high oxygen transport and redox properties such as CeO₂ to Pd supported on Al₂O₃ was linked to formation and stabilization of PdO [153,154]. A recent study by Foulandvand et al. [155] on Pd supported on Al₂O₃, CeO₂ or mixed Al₂O₃-CeO₂ support showed an enhanced CH₄ conversion for the CeO₂ containing catalysts under alternating rich and lean burn conditions. The explanation for such enhancement was the synergistic interaction between CeO₂ and Pd, and the direct oxidation of CH₄ by the support, promoted by the redox pair Ce³⁺ ↔ Ce⁴⁺. A promoting oxygen spill-over effect by ceria for higher CH₄ combustion activity was claimed by Colussi et al. [150,156] for Pd/Al₂O₃-CeO₂ and Zhou et al. [151] for Pd/Al₂O₃-Ce_{0.5}Zr_{0.5}O₂ catalysts. Their studies showed that the formation of PdO is

avored for Pd deposited on CeO₂ or Ce_{0.5}Zr_{0.5}O₂ surface in the mixed support. Therefore, the location of Pd on the mixed systems Al₂O₃-CeO₂ or Al₂O₃-Ce_{0.5}Zr_{0.5}O₂ appears to be crucial for catalytic activity and thermal stability. Thus, the controlled deposition of Pd on a specific site in a mixture of different oxide supports is highly desirable but difficult with conventional synthesis methods like precipitation or impregnation techniques.

Flame spray pyrolysis (FSP) is a powerful technique for the synthesis of nanoparticles and allows the production of high surface area catalysts [133]. Recently, selective deposition of nanoparticles on separate supports was made possible by a two-nozzle FSP setup [140,157]. Büchel et al. [157] reported that selective deposition of Pt on either BaCO₃ or Al₂O₃ in the mixed support BaCO₃-Al₂O₃ exhibited significant differences in catalytic activity caused by interactions between noble metal and support.

Here, the immediate environment of Pd will be controlled by depositing it either on the Al- or on the CeZr-sites in the mixed support Al₂O₃-Ce_{0.5}Zr_{0.5}O₂ in order to obtain a high and stable catalytic CH₄ combustion activity under lean burn conditions. By varying the operation temperatures in the range between 200 and 900°C, the behavior of such catalytic systems is compared to that of Pd on pure Ce_{0.5}Zr_{0.5}O₂ and Al₂O₃ supports.

5.2 Experimental methods

Preparation

Pd/Al₂O₃/Ce_{0.5}Zr_{0.5}O₂ catalysts were prepared with a single or two-nozzle FSP setup [158]. For the two-nozzle setup, an inter nozzle distance and an angle of 6 cm and 160°, respectively, were used to ensure the preferential deposition of Pd on support components [159]. Each nozzle used a premixed CH₄/O₂ flame at a volume ratio of 1/2 and a total gas flow of 3 L min⁻¹ to ignite and sustain the spray [134]. The aluminum-precursor solution consisted of aluminum-tri-sec-butoxide (Fluka, 95%) dissolved in a 2:1 volume ratio of diethylene glycol monobutyl ether (Fluka, 98%) and acetic anhydride (Riedel-de Haën, 99%). The Al-concentration was kept constant at 0.5 mol L⁻¹. The CeZr-precursor solution consisted of Ce 2-ethylhexanoate (Strem, 98%) and Zr 2-ethylhexanoate (Strem, 98%) dissolved in xylene (Riedel-de Haën, 95%). An appropriate amount of Pd(II)-acetylacetonate (Alfa Aesar, 99.99%) was added

either to the CeZr- or Al-solutions. Both precursor solutions were sprayed at 5 mL min^{-1} and were dispersed with 5 L min^{-1} O_2 (Pangas, 99,95%) each. The Al-, CeZr-, Pd- concentration and spray rates were chosen to result in a nominal Pd weight of 2.5 wt% and 4.0 wt% $\text{Ce}_{0.5}\text{Zr}_{0.5}\text{O}_2$ while the Ce to Zr ratio was 1. The flame-made catalysts were not subject to an additional temperature treatment and were tested as collected from the filter.

Here we abbreviate the supports Al_2O_3 and $\text{Ce}_{0.5}\text{Zr}_{0.5}\text{O}_2$ with Al and CeZr, respectively. In the case of 2 FSP setup the Pd is written next to the elements it was mixed in the precursor and we expect preferential precipitation onto it [157]. Some examples; Using the 2 FSP setup with one nozzle producing Pd/ Al_2O_3 and the other $\text{Ce}_{0.5}\text{Zr}_{0.5}\text{O}_2$ is referred to as PdAl-CeZr (note the dash between Al and CeZr) while Pd on pure Al_2O_3 produced in a 1 FSP setup is abbreviated as PdAl.

Characterization

Nitrogen adsorption–desorption isotherms were measured at 77 K using a Micromeritics Tristar instrument. The BET method was used to determine the specific surface area (SSA) by a 5-point nitrogen adsorption isotherm. The estimated accuracy is $\pm 3\%$. X-ray diffraction (XRD) patterns were recorded with a Bruker D8 Advance instrument (40 kV, 40 mA, $\lambda = 0.154 \text{ nm}$).

For scanning transmission electron microscopy (STEM), the catalyst material was dispersed in ethanol and deposited onto a perforated carbon foil supported on a copper grid (Okenshoji Co. Ltd.). The STEM images were obtained with a high-angle annular dark-field (HAADF) detector and thus show sites containing heavy materials with bright contrast (Z contrast). The detector is attached to an aberration-corrected HD2700CS microscope (Hitachi; cold field emission cathode, operated at 200 kV) additionally equipped with an energy-dispersive X-ray detector (EDXS) from EDAX.

Activity measurements

The oxidation of CH_4 was measured in a fixed-bed flow micro-reactor at atmospheric pressure. The reactor, a quartz tube of 5 mm inner diameter, was placed in an electric furnace (MTF 12/38/250, Carbolite). The catalytic bed consisted of 5 mg of catalyst mixed with 200 mg of calcined sand (Riedel-de Haën, average diameter: 200 μm) and was fixed in position with quartz glass

wool. A total gas flow of 100 mL min⁻¹ (1% CH₄, 4% O₂, 16% N₂ in He) was used. The transient activity behavior was measured by cycling the temperature from 200°C to 900°C at a heating respectively cooling rate of 10°C min⁻¹. The effluent gas stream composition was measured by gas chromatograph equipped with a thermal conductivity detector (6890 GC, with a HP-PlotQ column, Agilent). The CH₄ conversion was derived from the corresponding CH₄ outlet concentration according to

$$\text{CH}_4 \text{ conversion} = \frac{\text{CH}_{4,\text{out}} - \text{CH}_{4,\text{in}}}{\text{CH}_{4,\text{in}}} \times 100\% \quad (5.2)$$

The carbon mass balance was always higher than 97%. The standard deviations and errors derived from repeated measurements were less than 4% and therefore not shown in the figures.

The effect of temperature on the structure stability of the catalysts was investigated in four cycles where the temperature in each cycle the temperature was increased from 200 to 900°C and back to 200°C in ambient atmosphere at a heating and respectively cooling rate of 4°C min⁻¹. Before cooling, the samples were hold isothermally for 12 min at 900°C. This procedure was implemented in order to simulate the thermal behavior of the catalysts during cycling.

5.3 Results and discussion

Characterization

The effect of thermal treatment on the structure stability of the samples was investigated by cycling the temperature four times between 200 to 900°C in ambient atmosphere at a heating and respectively cooling rate of 4°C min⁻¹. Before cooling, the samples were hold isothermally for 12 min at 900°C. This procedure was implemented in order to simulate the thermal behavior of the catalysts during cycling.

Results of the measured specific surface area (SSA) of the Pd-free substrates and Pd containing catalysts before and after cycling are summarized in Table 5.1. For the as-prepared catalysts, the SSA for PdAl was the highest at 175 m²g⁻¹, whereas lower values were obtained when CeZr was

added ($161 \text{ m}^2\text{g}^{-1}$ – $164 \text{ m}^2\text{g}^{-1}$ at a nominal CeZr content of 4 wt% and $133 \text{ m}^2\text{g}^{-1}$ for Pd on pure CeZr). Cycling resulted in a decrease of SSA for all samples, especially for those with CeZr in the support. While sintering of PdAl did not show a large loss in SSA, for Pd on the mixed support Al-CeZr, only between 79% and 81% of the initial SSA was retained after sintering. For CeZrPd, only half of the SSA was still present. This means that the addition of CeZr to Al accelerated the loss of SSA during thermal treatment.

Table 5.1: SSA of reference supports and Pd-catalysts after preparation (as-prepared) and thermally aged in air (sintered).

Catalyst or support	BET [m^2g^{-1}] as-prepared	BET [m^2g^{-1}] sintered
Al	183	168
PdAl	175	154
PdAl-CeZr	161	128
Al-CeZrPd	164	133
CeZrPd	133	67
CeZr	132	72

Figure 5.1 depicts STEM images for the as-prepared and sintered PdAl-CeZr nanoparticles along with EDX spectra measured of the marked areas. The Pd particles in the as-prepared samples are discernible as bright dots ($Z_{\text{Pd}} = 46$ vs. $Z_{\text{Al}} = 13$) with a size in the range 1–3 nm. The CeZr appears likewise with bright contrast in the Z-contrast images ($Z_{\text{Ce}} = 58$; $Z_{\text{Zr}} = 40$) and is sometimes concentrated in 5–20 nm large areas. The EDX spectra displayed in Figure 5.1C confirm the preferential deposition of Pd on Al in the Al-CeZr support. In the sintered nanoparticles, some large PdO particles (diameter ca. 20–50 nm) were formed which is consistent with other studies on flame-made Pd catalysts [148,149]. Furthermore, the CeZr oxide has obviously sintered as particles of ca. 5 nm diameter are present.

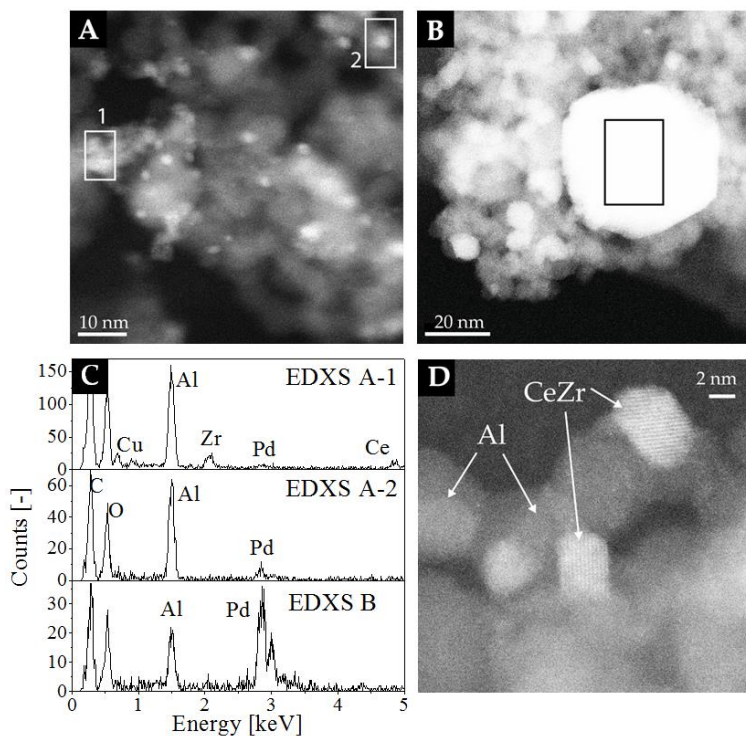


Figure 5.1: Typical STEM images of PdAl-CeZr. A: as-prepared; B and D: after thermal treatment (four cycles from 200–900°C); C: EDX spectra of indicated areas in A and B. The Cu signal in the EDXS is due the support grid.

The XRD pattern of all as-prepared and thermally treated samples catalysts is shown in Figure 5.2. For the as-prepared Pd containing samples, the loading and the cluster size of Pd are too small to be detected and comparable to similar studies [155]. Addition of 2.5 wt% Pd did not change the diffraction pattern of the supports. Samples containing $\text{Al}_2\text{O}_3\text{-Ce}_{0.5}\text{Zr}_{0.5}\text{O}_2$ showed mainly reflections of Al_2O_3 but also an additional peak at $2\theta = 29.5^\circ$ belonging to fluorite type, cubic $\text{Ce}_{0.5}\text{Zr}_{0.5}\text{O}_2$, indicating a very small concentration of the

CeZr- component in the mixed support. For Pd-free supports, the X-ray diffraction patterns looked the same before and after annealing. Addition of the noble metal did not change the characteristics of the supports after thermal treatment. However, presence of Al₂O₃ in supports accelerated formation and agglomeration of PdO (peaks at $2\theta = 34.0^\circ$, $2\theta = 42.1^\circ$ and $2\theta = 54.9^\circ$) compared to pure Ce_{0.5}Zr_{0.5}O₂ support during cycling. The particle size increase of PdO is supported by the STEM and EDXS analysis shown in Figure 5.1. In contrast to the XRD diffraction pattern obtained for the thermally treated CeZrPd sample and [151], addition of Ce_{0.5}Zr_{0.5}O₂ did not suppress bulk PdO agglomeration on Al₂O₃ containing supports probably because of the very low Ce_{0.5}Zr_{0.5}O₂ concentration (4 wt%) used in the present study.

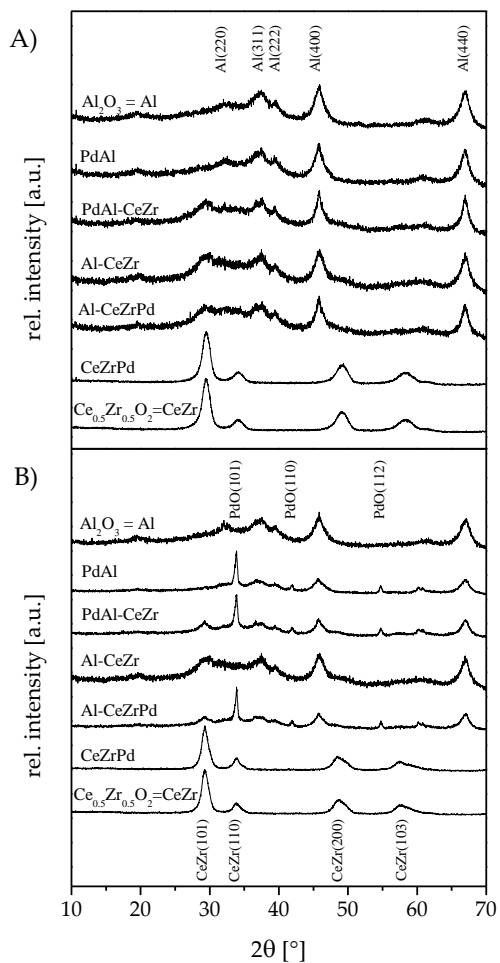


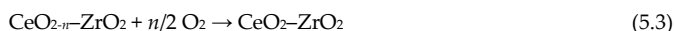
Figure 5.2: XRD pattern of A) as-prepared and B) thermally treated samples. The characteristic reflections of the supports are indicated in A) for Al_2O_3 or Al (ICSD: 39014), B) $\text{Ce}_{0.5}\text{Zr}_{0.5}\text{O}_2$ or CeZr (ICSD: 164608) and PdO (ICSD: 024692).

Catalytic activity during cycling between 200°C and 900°C

The catalytic CH₄ combustion activity was tested during cycling between 200°C and 900°C. For this, the Pd-free support materials and Pd supporting oxides were cycled two and five times, respectively.

The CH₄ conversion of the pure supports (without Pd) for CeZr, Al and Al-CeZr is shown in Figure 5.3. For CeZr, 2% CH₄ conversion was obtained at 600°C and increased to 25% and 87% at 750°C and 900°C, respectively. For Al, enhancement of the activity was negligible compared to homogeneous oxidation (represented as “empty tube” in Figure 5.3) and was 14% at 900°C and 5% higher compared to the homogenous reaction. Therefore, pure Al support was practically inert in the reaction. All supports showed negligible hysteresis and had almost the same activity during the two cycles.

The relatively high degree of CH₄ conversion for CeZr is consistent with [160] and can be explained with equations 5.3 and 5.4, where CH₄ oxidation is promoted by the redox properties of the pair Ce⁴⁺ ↔ Ce³⁺ due to oxygen transfer between support and educts CH₄ and O₂. The reduced form of Ce in the CeZr support is represented by Ce³⁺ at $n = 0.5$ and the mixed oxide as in [60] by Ce^{3+/4+} at $n < 0.5$.



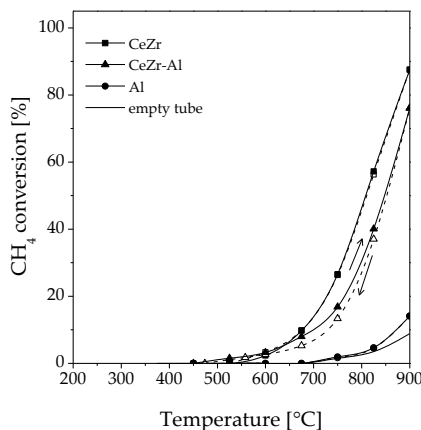


Figure 5.3: CH₄ conversion for pure supports (without Pd) CeZr, Al and Al-CeZr during the second heating (full symbols) and consequent cooling (empty symbols) cycle. Also, the conversion in an empty tube is shown.

In Figure 5.4, the CH₄ conversion of Pd containing samples during the first and fifth cycles are depicted as a function of temperature. Above 275 °C, all catalysts were active for CH₄ oxidation and conversion increased with higher temperatures. At the beginning of the cooling phase (< 900 °C), the conversion rate of CH₄ decreased significantly indicating the presence of metallic Pd. Below 500 °C the CH₄ conversion was higher during cooling compared to during heating, which is related to the kinetically limited re-oxidation of Pd into more active PdO [161]. This conversion hysteresis was present in all catalysts and was dependent on the support characteristics.

As depicted in Figure 5.4A and B, reaction for PdAl started at a lower temperature compared to CeZrPd and complete conversion of CH₄ was possible above 500 °C for all cycles. A clear difference in CH₄ conversion between PdAl and CeZrPd is seen during heating in the temperature range between 600 °C and 900 °C: Whereas complete CH₄ conversion was obtained for PdAl, a decrease in activity was observed for CeZrPd between 600 °C and 700 °C. This phenomenon suggests a change in Pd oxidation state from Pd²⁺ to metallic Pd⁰ on the CeZr support. The increase in CH₄ conversion on CeZrPd support between 700 °C and 900 °C is caused to a high extent from the direct oxidation activity of the CeZr support, as depicted in Figure 5.3. During cooling in the

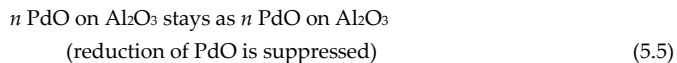
temperature range between 850°C and 550°C, the activity was higher for CeZrPd compared to PdAl: In the first cooling ramp the minimal CH₄ conversion was 43% at 750°C for CeZrPd and 13% at 600°C for PdAl. Therefore, CeZr promoted a much faster Pd re-oxidation and consequently a faster recovery of the catalytic activity compared to Al. The activity behavior for PdAl during the first heating and cooling cycle was very similar to that reported in literature e.g. the PdAl by van Vegten et al. [149], who additionally investigated activity of flame-made Pd/CeO₂. Contrary to the activity obtained for Pd/CeO₂ in [149], the activity of CeZrPd in our study increased significantly after the first cycle, with CH₄ conversion values reaching 100% (Figure 5.4B). This observed difference in performance between Pd/CeO₂ and CeZrPd is presumably caused by the resulted thermal stabilization and enhanced redox behavior by doping CeO₂ with ZrO₂, as reported previously [113-115].

Difference in performance can be observed for Pd deposited preferably on either Al or CeZr in the mixed support Al-CeZr (Figure 5.4C and D). During heating, CH₄ conversion decreased for Al-CeZrPd at around 825°C during the fifth cycle, while no such drop occurred for PdAl-CeZr. Considering the behavior of CeZrPd during heating, we can conclude that the presence of Al in the support suppresses drop of activity in the temperature range of PdO reduction between 600°C and 900°C (Figure 5.4B and D). The reduction of PdO was promoted on CeZr likely due to a reversed oxygen spill-over process from Pd to the support and/or suppressed re-oxidation by gaseous O₂. While oxygen exchange between Pd and Al support was previously observed during combustion of CH₄ at 400°C [162], the oxidized form of Al and Pd (Al₂O₃ and PdO) were preserved. Here, reduction of PdO is triggered by the redox properties of CeZr support (see equations 3 and 4). During the cooling phase, the degree of activity for Al-CeZrPd was higher compared to PdAl-CeZr. In line with the results obtained with CeZrPd and PdAl, CeZr in the Al-CeZrPd sample allowed for sooner recovery, i.e. formation of active PdO, compared to Al in the PdAl-CeZr catalyst.

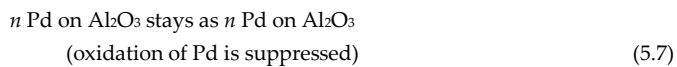
In summary, Ce_{0.5}Zr_{0.5}O₂ showed a remarkably enhanced PdO ↔ Pd redox process, with PdO → Pd occurring at temperatures as low as 600°C. Such PdO reduction is thermodynamically expected and comparable with the behavior of pure Pd in [149]. On the other hand, Al₂O₃ stabilized PdO during heating, thus promoting the catalytic activity for CH₄ combustion. Equations 5.5–5.8

summarize the identified redox behavior for Pd and supports at different stages during cycling according to Figure 5.3 and Figure 5.4A-D.

During heating at high temperatures:



During cooling at high temperatures:



where $n \leq 0.5$.

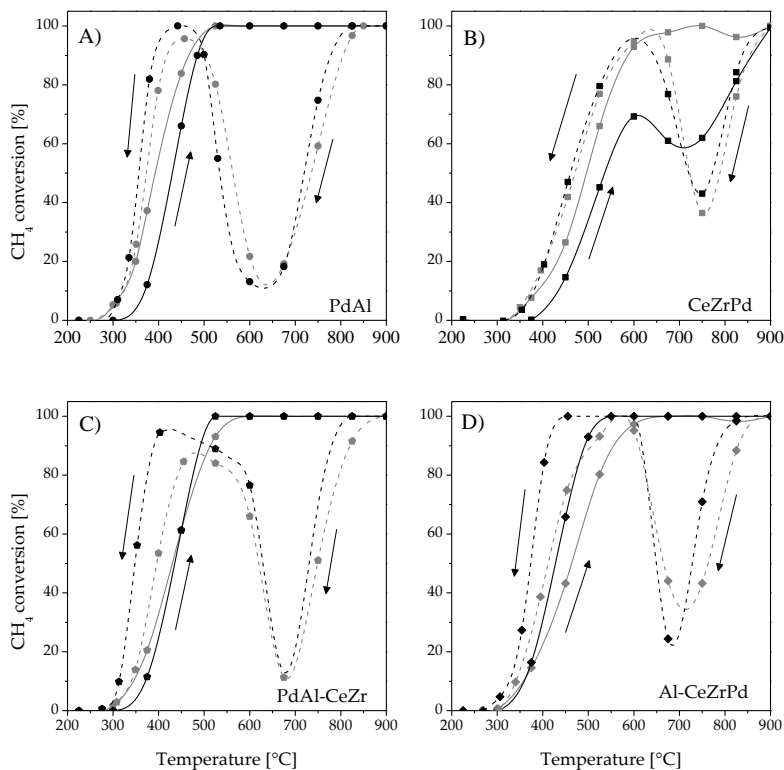


Figure 5.4: Comparison of hysteresis behavior for the first (black) and fifth (grey) cycles of Pd catalysts: lines during heating (solid) and cooling (dashed) are displayed to guide the eye. A) PdAl, B) CeZrPd, C) PdAl-CeZr and D) Al-CeZrPd.

In Figure 5.5, the evolution of the CH_4 conversion at 375°C , 450°C and 525°C is shown as a function of the cycle number. In the first heating ramp (cycle 1), CH_4 conversion was similar for Al containing catalysts (at all three temperatures), with the Al-CeZrPd being slightly more active at 375°C and 450°C . For CeZrPd, higher temperatures were needed to obtain conversion

values above 50% that are comparable to those of Pd on Al containing supports. For the first heating ramp, CH₄ combustion activity increased in the order: CeZrPd < PdAl-CeZr ≤ PdAl ≤ Al-CeZrPd. This shows that activity of Pd on CeZr on the mixed support is highest prior to the cycling treatment.

After the first cycle, activation at lower temperatures and therefore higher CH₄ conversion was obtained for all catalysts. Similar improvement was observed previously on flame-made PdAl systems and is likely caused by restructuring and sintering of Pd on the substrate during reduction and re-oxidation [31,148,163] and higher PdO/Pd ratio after re-oxidation of Pd [149].

For the following cycles, the activity of Pd supported on Al was highest and activity increases in the order CeZrPd < Al-CeZrPd < PdAl-CeZr < PdAl. The decrease in activity of Pd on Al containing supports is steeper than for CeZrPd, in spite of the lower loss in SSA for Al containing catalysts after sintering (see Table 5.1). Decrease of Pd activity on Al supports for CH₄ oxidation was associated to PdO site growth in [31,149]. In the present study, the crystallite size of the PdO also increased for Al containing supports after thermal treatment, as shown in Figure 5.1 and Figure 5.2. During the cycling process, CeZrPd showed the highest stability (from cycles 2 to 5: -1.5% at 375°C and 450°C and -0.5% at 525°C). In spite of this low decrease in activity, CH₄ conversion for CeZrPd in the fifth cycle still remained at 7.7% and 26.4%, meaning between 29.5% and 57.5% below that for PdAl (37.2% and 83.9%) at 375°C and 450°C, respectively. A small hysteresis degree was also observed for CeZrPd from cycles 2 to 5, which is in line with other studies [150,156,164] and regarded to promotion of Pd redox reaction by CeZr (equations 5.6 and 5.8).

In summary, the presence of Al in the support enhanced the activity of Pd during cycling as Al-CeZrPd > PdAl-CeZr > PdAl, while the CeZr support alone stabilized better the Pd activity (Figure 5.5).

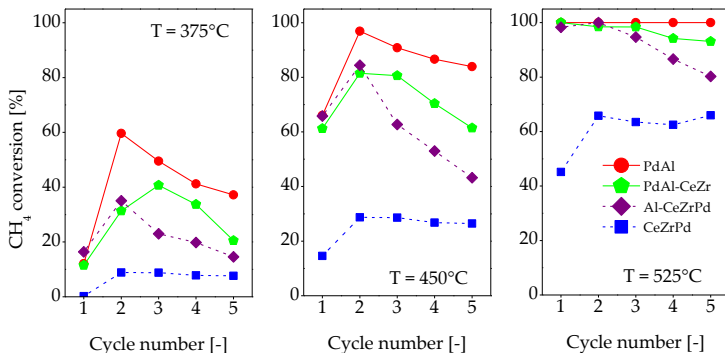


Figure 5.5: CH₄ conversion during heating at 375°C, 450°C and 525°C for cycles between 200°C and 900°C. The CH₄ oxidation activity increased in the order: CeZrPd < PdAl-CeZr ≤ PdAl ≤ Al-CeZrPd (1st cycle), CeZrPd < PdAl-CeZr ≤ Al-CeZrPd < PdAl (2nd cycle) and CeZrPd < Al-CeZrPd < PdAl-CeZr < PdAl (cycles 3-5).

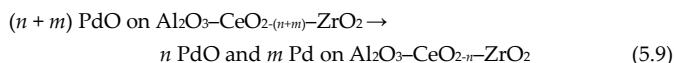
Activity tests at constant temperature

To study the catalytic stability, measurements were performed for as-prepared catalysts without any prior thermal treatment, i.e. cycling, for 10 h–16 h. Figure 5.6 depicts the CH₄ conversion obtained at 450°C and 530°C. Differences in performance can be observed for all catalysts. At 450°C (Figure 5.6A), the initial activity was highest for Pd deposited on CeZr in the Al-CeZr support, followed by PdAl-CeZr and PdAl, and finally CeZrPd. So far, this trend is in line with results obtained during the first heating ramp during the cycling experiments (Figure 5.6A-D). Activity increased for all catalysts during the first hour of testing. Such short term performance improvement was observed previously [149,165,166] and is probably caused by morphological changes e.g. restructuring and sintering of Pd with time on stream and a higher PdO/Pd ratio after cooling.

At the investigated temperatures, the activity of all catalysts decreased consistently with time on stream and the order of activity became: PdAl-CeZr > PdAl > Al-CeZrPd > of Al-CeZrPd > CeZrPd. This trend stands in contrast to results obtained during cycling, where CH₄ conversion for PdAl was highest (Figure 5.4). These results underpin the statement given in the previous

section: at these low temperatures and without exposing Pd to redox cycles by increasing and decreasing temperatures, the activity of Pd is promoted by the presence of CeZr on Al support.

In [31,167,168], a combination of PdO, partially oxidized PdO_x and metallic Pd was beneficial for activity. In the present study we cannot comment conclusively about the ratio between the different Pd-constituents in the catalyst. However, based on the obtained results, we can suggest that in a catalytic system such as PdAl-CeZr, in which Pd is preferably deposited on the Al component and CeZr is in preferred contact with Al, the formation of reduced Pd species is limited by the distance between Pd and CeZr, but still existent. This means that a specific ratio of Pd and PdO is given during reaction, which is favorable towards high activity [31,150]. Equation 5.9 shows the proposed reaction on the variation of Pd oxidation state.



where $n + m \leq 0.5$.

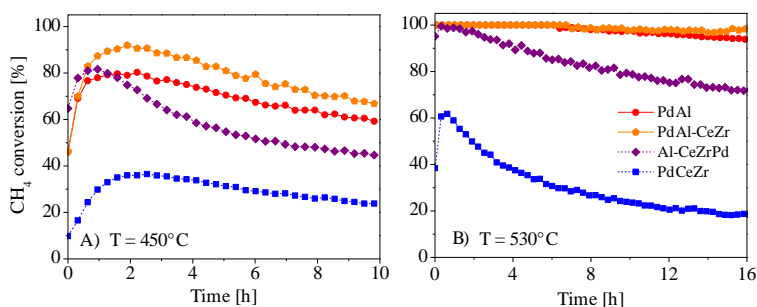


Figure 5.6: CH₄ conversion as a function of time at constant temperatures: A) 450°C and B) 530°C.

Similar to results obtained during cycling (section “Catalytic activity during cycling between 200°C and 900°C”), the fact that Pd is less active when deposited on CeZr (Al-CeZrPd and CeZrPd) than on Al (PdAl-CeZr and PdAl), confirms that direct contact of Pd and CeZr is detrimental for high activity. As discussed earlier, the enhanced redox Pd/PdO behavior promoted

by CeZr, results in less active Pd species and decrease in performance, as shown in equations 5.6 and 5.8.

Other properties such as thermal stability of support and interactions between support and Pd could have contributed to the progressive decrease in performance [143]. Also, progressive formation of PdO_x species could have contributed to destabilization of Pd catalytic properties. Formation of inactive Pd(OH)₂ blocked the access of CH₄ to active PdO sites in [169], while in [170,171], the presence of H₂O, either as a product of CH₄ conversion or as educt in the reaction feed, formed a stable Pd(OH)₂ on the Al support and inhibited catalytic activity and thus stability.

5.4 Conclusion

The significance of Pd location in the mixed support Al₂O₃-Ce_{0.5}Zr_{0.5}O₂ was studied for the catalytic CH₄ combustion reaction under lean burn conditions by employing a two-nozzle flame spray pyrolysis (FSP) unit. The control of locality of Pd on either the Al- or CeZr- sites in the mixed Al₂O₃-Ce_{0.5}Zr_{0.5}O₂ support affected markedly catalytic activity and stability.

Deposition of Pd on Ce_{0.5}Zr_{0.5}O₂ was detrimental to high CH₄ oxidation activity, while the presence of Al₂O₃, and especially deposition of the noble metal on it, clearly enhanced Pd activity: 1) During cycling (200–900°C), Pd supported selectively on Al₂O₃ showed the highest activity due to stabilization of active PdO, but agglomeration of PdO on the support at high temperatures had a negative effect. On the other hand, the less active Pd on Ce_{0.5}Zr_{0.5}O₂ showed the lowest hysteresis, promoted by the redox properties of Ce_{0.5}Zr_{0.5}O₂ support and thus promotion of the PdO ↔ Pd reaction by oxygen spill-over between Ce_{0.5}Zr_{0.5}O₂ and Pd. 2) At constant temperatures of 450°C and 530°C, Pd deposited on Al₂O₃ in the mixed support was unexpectedly the preferred catalyst. This catalyst system was most stable due to a threefold effect caused by oxygen spill-over from the Ce_{0.5}Zr_{0.5}O₂ to the noble metal, direct oxidation of CH₄ by Ce_{0.5}Zr_{0.5}O₂ and simultaneous stabilization of active PdO by Al₂O₃ support.

6 Bibliography

- [1] A. Bieberle-Hutter, D. Beckel, A. Infortuna, U. P. Muecke, J. L. M. Rupp, L. J. Gauckler, S. Rey-Mermet, P. Mural, N. R. Bieri, N. Hotz, M. J. Stutz, D. Poulidakos, P. Heeb, P. Muller, A. Bernard, R. Gmur, and T. Hocker, "A micro-solid oxide fuel cell system as battery replacement," *Journal of Power Sources*, vol. 177, pp. 123-130, 2008.
- [2] E. D. Wachsman, and K. T. Lee, "Lowering the Temperature of Solid Oxide Fuel Cells," *Science*, vol. 334, pp. 935-939, 2011.
- [3] S. Ahmed, and M. Krumpelt, "Hydrogen from hydrocarbon fuels for fuel cells," *International Journal of Hydrogen Energy*, vol. 26, pp. 291-301, 2001.
- [4] R. Tolke, A. Bieberle-Hutter, A. Evans, J. L. M. Rupp, and L. J. Gauckler, "Processing of Foturan glass ceramic substrates for micro-solid oxide fuel cells," *Journal of the European Ceramic Society*, vol. 32, pp. 3229-3238, 2012.
- [5] A. Evans, A. Bieberle-Hutter, H. Galinski, J. L. M. Rupp, T. Ryll, B. Scherrer, R. Tolke, and L. J. Gauckler, "Micro-solid oxide fuel cells: status, challenges, and chances," *Monatshefte Fur Chemie*, vol. 140, pp. 975-983, 2009.
- [6] J. Komadina, Y. B. Kim, J. S. Park, T. M. Gur, S. Kang, and F. B. Prinz, "Low Temperature Direct Methanol Fuel Cell with YSZ Electrolyte," *Solid Oxide Fuel Cells 12 (Sofc Xii)*, vol. 35, pp. 2855-2866, 2011.
- [7] Y. B. Kim, T. P. Holme, T. M. Gur, and F. B. Prinz, "Surface-Modified Low-Temperature Solid Oxide Fuel Cell," *Advanced Functional Materials*, vol. 21, pp. 4684-4690, 2011.
- [8] T. P. Holme, R. Pornprasertsuk, and F. B. Prinz, "Interpretation of Low Temperature Solid Oxide Fuel Cell Electrochemical Impedance Spectra," *Journal of the Electrochemical Society*, vol. 157, pp. B64-B70, 2010.
- [9] C. C. Chao, C. M. Hsu, Y. Cui, and F. B. Prinz, "Improved Solid Oxide Fuel Cell Performance with Nanostructured Electrolytes," *Acs Nano*, vol. 5, pp. 5692-5696, 2011.
- [10] H. Huang, M. Nakamura, P. C. Su, R. Fasching, Y. Saito, and F. B. Prinz, "High-performance ultrathin solid oxide fuel cells for low-temperature operation," *Journal of the Electrochemical Society*, vol. 154, pp. B20-B24, 2007.
- [11] Y. Jiang, and A. V. Virkar, "Fuel composition and diluent effect on gas transport and performance of anode-supported SOFCs," *Journal of the Electrochemical Society*, vol. 150, pp. A942-A951, 2003.

- [12] R. J. Gorte, and J. M. Vohs, "Novel SOFC anodes for the direct electrochemical oxidation of hydrocarbons," *Journal of Catalysis*, vol. 216, pp. 477-486, 2003.
- [13] B. C. H. Steele, "Fuel-cell technology - Running on natural gas," *Nature*, vol. 400, pp. 619, 1999.
- [14] N. Hotz, N. Osterwalder, W. J. Stark, N. R. Bieri, and D. Poulikakos, "Disk-shaped packed bed micro-reactor for butane-to-syngas processing," *Chemical Engineering Science*, vol. 63, pp. 5193-5201, 2008.
- [15] C. Finnerty, G. A. Tompsett, K. Kendall, and R. M. Ormerod, "SOFC system with integrated catalytic fuel processing," *Journal of Power Sources*, vol. 86, pp. 459-463, 2000.
- [16] S. A. Seyed-Reihani, and G. S. Jackson, "Catalytic partial oxidation of n-butane over Rh catalysts for solid oxide fuel cell applications," *Catalysis Today*, vol. 155, pp. 75-83, 2010.
- [17] Z. P. Shao, S. M. Haile, J. Ahn, P. D. Ronney, Z. L. Zhan, and S. A. Barnett, "A thermally self-sustained micro solid-oxide fuel-cell stack with high power density," *Nature*, vol. 435, pp. 795-798, 2005.
- [18] M. J. Moran, and H. N. Shapiro, "Fundamentals of engineering thermodynamics," *John Wiley & Sons Ltd*, vol. 4th ed., pp. 839-847, 2004.
- [19] S. D. Park, J. M. Vohs, and R. J. Gorte, "Direct oxidation of hydrocarbons in a solid-oxide fuel cell," *Nature*, vol. 404, pp. 265-267, 2000.
- [20] R. J. Gorte, S. Park, J. M. Vohs, and C. H. Wang, "Anodes for direct oxidation of dry hydrocarbons in a solid-oxide fuel cell," *Advanced Materials*, vol. 12, pp. 1465-1469, 2000.
- [21] S. McIntosh, and R. J. Gorte, "Direct hydrocarbon solid oxide fuel cells," *Chemical Reviews*, vol. 104, pp. 4845-4865, 2004.
- [22] C. Lu, S. An, W. L. Worrell, J. M. Vohs, and R. J. Gorte, "Development of intermediate-temperature solid oxide fuel cells for direct utilization of hydrocarbon fuels," *Solid State Ionics*, vol. 175, pp. 47-50, 2004.
- [23] S. Park, R. Craciun, J. M. Vohs, and R. J. Gorte, "Direct oxidation of hydrocarbons in a solid oxide fuel cell I. Methane oxidation," *Journal of the Electrochemical Society*, vol. 146, pp. 3603-3605, 1999.
- [24] E. S. Hecht, G. K. Gupta, H. Y. Zhu, A. M. Dean, R. J. Kee, L. Maier, and O. Deutschmann, "Methane reforming kinetics within a Ni-YSZ SOFC anode support," *Applied Catalysis a-General*, vol. 295, pp. 40-51, 2005.
- [25] S. McIntosh, H. P. He, S. I. Lee, O. Costa-Nunes, V. V. Krishnan, J. M. Vohs, and R. J. Gorte, "An examination of carbonaceous deposits

- in direct-utilization SOFC anodes," *Journal of the Electrochemical Society*, vol. 151, pp. A604-A608, 2004.
- [26] Z. L. Zhan, J. Liu, and S. A. Barnett, "Operation of anode-supported solid oxide fuel cells on propane-air fuel mixtures," *Applied Catalysis a-General*, vol. 262, pp. 255-259, 2004.
- [27] M. Horiuchi, F. Katagiri, J. Yoshiike, S. Suganuma, Y. Tokutake, H. Kronemayer, and W. G. Bessler, "Performance of a solid oxide fuel cell couple operated via in situ catalytic partial oxidation of n-butane," *Journal of Power Sources*, vol. 189, pp. 950-957, 2009.
- [28] A. P. E. York, T. C. Xiao, and M. L. H. Green, "Brief overview of the partial oxidation of methane to synthesis gas," *Topics in Catalysis*, vol. 22, pp. 345-358, 2003.
- [29] B. C. Enger, R. Lodeng, and A. Holmen, "A review of catalytic partial oxidation of methane to synthesis gas with emphasis on reaction mechanisms over transition metal catalysts," *Applied Catalysis a-General*, vol. 346, pp. 1-27, 2008.
- [30] N. Hotz, N. Koc, T. Schwamb, N. C. Schirmer, and D. Poulikakos, "Catalytic Porous Ceramic Prepared In-Situ by Sol-Gelation for Butane-to-Syngas Processing in Microreactors," *AIChE Journal*, vol. 55, pp. 1849-1859, 2009.
- [31] N. M. Kinnunen, J. T. Hirvi, T. Venalainen, M. Suvanto, and T. A. Pakkanen, "Procedure to tailor activity of methane combustion catalyst: Relation between Pd/PdO_x active sites and methane oxidation activity," *Applied Catalysis a-General*, vol. 397, pp. 54-61, 2011.
- [32] P. Gelin, and M. Primet, "Complete oxidation of methane at low temperature over noble metal based catalysts: a review," *Applied Catalysis B-Environmental*, vol. 39, pp. 1-37, 2002.
- [33] W. G. Liu, D. Y. Guo, and X. Xu, "Research Progress of Palladium Catalysts for Methane Combustion," *China Petroleum Processing & Petrochemical Technology*, vol. 14, pp. 1-9, 2012.
- [34] M. Lyubovsky, L. L. Smith, M. Castaldi, H. Karim, B. Nentwick, S. Etemad, R. LaPierre, and W. C. Pfefferle, "Catalytic combustion over platinum group catalysts: fuel-lean versus fuel-rich operation," *Catalysis Today*, vol. 83, pp. 71-84, 2003.
- [35] A. Hawkes, I. Staffell, D. Brett, and N. Brandon, "Fuel cells for micro-combined heat and power generation," *Energy & Environmental Science*, vol. 2, pp. 729-744, 2009.
- [36] A. Mitsos, I. Palou-Rivera, and P. I. Barton, "Alternatives for micropower generation processes," *Industrial & Engineering Chemistry Research*, vol. 43, pp. 74-84, 2004.

- [37] S. Tominaka, H. Nishizeko, J. Mizuno, and T. Osaka, "Bendable fuel cells: on-chip fuel cell on a flexible polymer substrate," *Energy & Environmental Science*, vol. 2, pp. 1074-1077, 2009.
- [38] S. Tominaka, S. Ohta, T. Osaka, and R. Alkire, "Prospects of on-chip fuel cell performance: improvement based on numerical simulation," *Energy & Environmental Science*, vol. 4, pp. 162-171, 2011.
- [39] A. Evans, A. Bieberle-Hutter, J. L. M. Rupp, and L. J. Gauckler, "Review on microfabricated micro-solid oxide fuel cell membranes," *Journal of Power Sources*, vol. 194, pp. 119-129, 2009.
- [40] J. C. Ruiz-Morales, D. Marrero-Lopez, M. Galvez-Sanchez, J. Canales-Vazquez, C. Savaniu, and S. N. Savvin, "Engineering of materials for solid oxide fuel cells and other energy and environmental applications," *Energy & Environmental Science*, vol. 3, pp. 1670-1681, 2010.
- [41] H. Y. Qin, Z. G. Zhu, Q. H. Liu, Y. F. Jing, R. Raza, S. Imran, M. Singh, G. Abbas, and B. Zhu, "Direct biofuel low-temperature solid oxide fuel cells," *Energy & Environmental Science*, vol. 4, pp. 1273-1276, 2011.
- [42] E. P. Murray, T. Tsai, and S. A. Barnett, "A direct-methane fuel cell with a ceria-based anode," *Nature*, vol. 400, pp. 649-651, 1999.
- [43] T. Hibino, A. Hashimoto, T. Inoue, J. Tokuno, S. Yoshida, and M. Sano, "A solid oxide fuel cell using an exothermic reaction as the heat source," *Journal of the Electrochemical Society*, vol. 148, pp. A544-A549, 2001.
- [44] T. W. Napporn, F. Morin, and M. Meunier, "Evaluation of the actual working temperature of a single-chamber SOFC," *Electrochemical and Solid State Letters*, vol. 7, pp. A60-A62, 2004.
- [45] D. M. Bierschenk, J. R. Wilson, and S. A. Barnett, "High efficiency electrical energy storage using a methane-oxygen solid oxide cell," *Energy & Environmental Science*, vol. 4, pp. 944-951, 2011.
- [46] C. O. Colpan, F. Hamdullahpur, I. Dincer, and Y. Yoo, "Effect of gasification agent on the performance of solid oxide fuel cell and biomass gasification systems," *International Journal of Hydrogen Energy*, vol. 35, pp. 5001-5009, 2010.
- [47] T. Suzuki, T. Yamaguchi, K. Hamamoto, Y. Fujishiro, M. Awano, and N. Sammes, "A functional layer for direct use of hydrocarbon fuel in low temperature solid-oxide fuel cells," *Energy & Environmental Science*, vol. 4, pp. 940-943, 2011.
- [48] N. Hotz, M. J. Stutz, S. Loher, W. J. Stark, and D. Poulidakos, "Syngas production from butane using a flame-made Rh/Ce_{0.5}Zr_{0.5}O₂ catalyst," *Applied Catalysis B-Environmental*, vol. 73, pp. 336-344, 2007.

- [49] M. Huff, and L. D. Schmidt, "Production of Olefins by Oxidative Dehydrogenation of Propane and Butane over Monoliths at Short-Contact Times," *Journal of Catalysis*, vol. 149, pp. 127-141, 1994.
- [50] L. Basini, A. Guarinoni, and A. Aragno, "Molecular and temperature aspects in catalytic partial oxidation of methane," *Journal of Catalysis*, vol. 190, pp. 284-295, 2000.
- [51] R. J. Bass, T. M. Dunn, Y. C. Lin, and K. L. Hohn, "Syngas production from catalytic partial oxidation of n-butane: Comparison between incipient wetness and sol-gel prepared Pt/Al₂O₃," *Industrial & Engineering Chemistry Research*, vol. 47, pp. 7184-7189, 2008.
- [52] S. A. Seyed-Reihani, and G. S. Jackson, "Influence of thermal conditions on partial oxidation of n-butane over supported Rh catalysts," *Applied Catalysis a-General*, vol. 353, pp. 181-192, 2009.
- [53] C. A. Leclerc, J. M. Redenius, and L. D. Schmidt, "Fast lightoff of millisecond reactors," *Catalysis Letters*, vol. 79, pp. 39-44, 2002.
- [54] L. D. Schmidt, E. J. Klein, C. A. Leclerc, J. J. Krummenacher, and K. N. West, "Syngas in millisecond reactors: higher alkanes and fast lightoff," *Chemical Engineering Science*, vol. 58, pp. 1037-1041, 2003.
- [55] K. Sato, K. Adachi, K. Nagaoka, H. Nishiguchi, and Y. Takita, "Oxidative reforming of n-C₄H₁₀ triggered at ambient temperature over reduced Ni/CeO₂," *Catalysis Communications*, vol. 10, pp. 1478-1481, 2009.
- [56] K. Nagaoka, K. Sato, S. Fukuda, S. Nakashiki, H. Nishiguchi, J. A. Lercher, and Y. Takita, "Oxidative reforming of n-butane triggered by spontaneous oxidation of CeO_{2-x} at ambient temperature," *Chemistry of Materials*, vol. 20, pp. 4176-4178, 2008.
- [57] M. J. Stutz, R. N. Grass, S. Loher, W. J. Stark, and D. Poulikakos, "Fast and exergy efficient start-up of micro-solid oxide fuel cell systems by using the reformer or the post-combustor for start-up heating," *Journal of Power Sources*, vol. 182, pp. 558-564, 2008.
- [58] A. V. Pattekar, and M. V. Kothare, "A radial microfluidic fuel processor," *Journal of Power Sources*, vol. 147, pp. 116-127, 2005.
- [59] N. B. Raberger, M. J. Stutz, N. Hotz, and D. Poulikakos, "Simulation of the Postcombustor for the Treatment of Toxic and Flammable Exhaust Gases of a Micro-Solid Oxide Fuel Cell," *Journal of Fuel Cell Science and Technology*, vol. 6, pp., 2009.
- [60] W. J. Stark, M. Maciejewski, L. Madler, S. E. Pratsinis, and A. Baiker, "Flame-made nanocrystalline ceria/zirconia: structural properties and dynamic oxygen exchange capacity," *Journal of Catalysis*, vol. 220, pp. 35-43, 2003.
- [61] W. J. Stark, L. Madler, M. Maciejewski, S. E. Pratsinis, and A. Baiker, "Flame synthesis of nanocrystalline ceria-zirconia: effect of carrier liquid," *Chemical Communications*, vol., pp. 588-589, 2003.

- [62] A. K. Chaniotis, and D. Poulidakos, "Modeling and optimization of catalytic partial oxidation methane reforming for fuel cells," *Journal of Power Sources*, vol. 142, pp. 184-193, 2005.
- [63] E. J. Klein, S. Tummala, and L. D. Schmidt, "Catalytic partial oxidation of methane to syngas: staged and stratified reactors with steam addition," *Natural Gas Conversion VI*, vol., pp. 245-250, 2000.
- [64] M. Huff, P. M. Torniainen, and L. D. Schmidt, "Partial Oxidation of Alkanes over Noble-Metal Coated Monoliths," *Catalysis Today*, vol. 21, pp. 113-128, 1994.
- [65] R. P. O'Connor, E. J. Klein, and L. D. Schmidt, "High yields of synthesis gas by millisecond partial oxidation of higher hydrocarbons," *Catalysis Letters*, vol. 70, pp. 99-107, 2000.
- [66] C. H. Bartholomew, "Mechanisms of catalyst deactivation," *Applied Catalysis a-General*, vol. 212, pp. 17-60, 2001.
- [67] W. Bujalski, C. A. Dikwal, and K. Kendall, "Cycling of three solid oxide fuel cell types," *Journal of Power Sources*, vol. 171, pp. 96-100, 2007.
- [68] K. L. Hohn, C. C. Huang, and C. Cao, "Catalytic ignition of light hydrocarbons," *Journal of Natural Gas Chemistry*, vol. 18, pp. 115-123, 2009.
- [69] K. B. Min, S. Tanaka, and M. Esashi, "MEMS-based polymer electrolyte fuel cell," *Electrochemistry*, vol. 70, pp. 924-927, 2002.
- [70] T. Yoshitake, H. Kimura, S. Kuroshima, S. Watanabe, Y. Shimakawa, T. Manako, S. Nakamura, and Y. Kubo, "Small direct methanol fuel cell pack for portable applications," *Electrochemistry*, vol. 70, pp. 966-968, 2002.
- [71] Z. Shao, S. M. Haile, J. Ahn, P. D. Ronney, Z. Zhan, and S. A. Barnett, "A thermally self-sustained micro solid-oxide fuel-cell stack with high power density," *Nature*, vol. 435, pp. 795-798, 2005.
- [72] B. Liu, R. Shang, K. L. Hu, Z. M. Wang, and S. Gao, "A New Series of Chiral Metal Formate Frameworks of [HONH3][M-II(HCOO)(3)] (M=Mn, Co, Ni, Zn, and Mg): Synthesis, Structures, and Properties," *Inorganic Chemistry*, vol. 51, pp. 13363-13372, 2012.
- [73] F. M. Liu, Y. Q. Zhang, Y. S. Yu, J. Xu, J. B. Sun, and G. Y. Lu, "Enhanced sensing performance of catalytic combustion methane sensor by using Pd nanorod/gamma-Al₂O₃," *Sensors and Actuators B-Chemical*, vol. 160, pp. 1091-1097, 2011.
- [74] L. Chen, Z. J. Pu, J. Yang, X. L. Yang, and X. B. Liu, "Synthesis and properties of sulfonated polyarylene ether nitrile copolymers for PEM with high thermal stability," *Journal of Polymer Research*, vol. 20, pp., 2013.

- [75] G. S. Jackson, and S. A. Seyed-Reihani, "Catalytic partial oxidation of n-butane over Rh catalysts for solid oxide fuel cell applications," *Catalysis Today*, vol. 155, pp. 75-83, 2010.
- [76] Q. J. Yu, J. M. Xu, J. Liu, B. X. Li, Y. J. Liu, and Y. Y. Han, "Synthesis and properties of PANI/SiO₂ organic-inorganic hybrid films," *Applied Surface Science*, vol. 263, pp. 532-535, 2012.
- [77] W. W. Guo, T. M. Liu, R. Sun, Y. Chen, W. Zeng, and Z. C. Wang, "Synthesis of unique ZnO/SnO₂ core-shell structural microspheres and their gas-sensing properties," *Materials Letters*, vol. 89, pp. 5-8, 2012.
- [78] C. B. Wang, H. G. Lee, T. F. Yeh, S. N. Hsu, and K. S. Chu, "Thermal characterization of titania-modified alumina-supported palladium and catalytic properties for methane combustion," *Thermochimica Acta*, vol. 401, pp. 209-216, 2003.
- [79] X. N. Guo, P. Brault, G. J. Zhi, A. Caillard, G. Q. Jin, and X. Y. Guo, "Structural Evolution of Plasma-Sputtered Core-Shell Nanoparticles for Catalytic Combustion of Methane," *Journal of Physical Chemistry C*, vol. 115, pp. 24164-24171, 2011.
- [80] X. Fan, F. Wang, T. L. Zhu, and H. He, "Effects of Ce on catalytic combustion of methane over Pd-Pt/Al₂O₃ catalyst," *Journal of Environmental Sciences-China*, vol. 24, pp. 507-511, 2012.
- [81] A. V. Pattekar, and M. V. Kothare, "A radial microfluidic fuel processor," *Journal of Power Sources*, vol. 147, pp. 116-127, 2005.
- [82] S. Tanaka, K.-S. Chang, K.-B. Min, D. Satoh, K. Yoshida, and M. Esashi, "MEMS-based components of a miniature fuel cell/fuel reformer system," *Chemical Engineering Journal*, vol. 101, pp. 143-149, 2004.
- [83] R. Horn, K. A. Williams, N. J. Degenstein, A. Bitsch-Larsen, D. D. Nogare, S. A. Tupy, and L. D. Schmidt, "Methane catalytic partial oxidation on autothermal Rh and Pt foam catalysts: Oxidation and reforming zones, transport effects, and approach to thermodynamic equilibrium," *Journal of Catalysis*, vol. 249, pp. 380-393, 2007.
- [84] A. Bitsch-Larsen, R. Horn, and L. D. Schmidt, "Catalytic partial oxidation of methane on rhodium and platinum: Spatial profiles at elevated pressure," *Applied Catalysis a-General*, vol. 348, pp. 165-172, 2008.
- [85] R. Horn, K. A. Williams, N. J. Degenstein, and L. D. Schmidt, "Syngas by catalytic partial oxidation of methane on rhodium: Mechanistic conclusions from spatially resolved measurements and numerical simulations," *Journal of Catalysis*, vol. 242, pp. 92-102, 2006.
- [86] E. Leal, H. M. C. Andrade, and A. C. F. D. Costa, "Influence of the Urea Content in the Combustion Synthesis for Preparation of

- NiAl₂O₄ Support Catalytic to Steam Reforming of Methane," *Advanced Powder Technology VIII, Pts 1 and 2*, vol. 727-728, pp. 1249-1255, 2012.
- [87] H. Pennemann, V. Hessel, G. Kolb, H. Lowe, and R. Zapf, "Partial oxidation of propane using micro structured reactors," *Chemical Engineering Journal*, vol. 135, pp. S66-S73, 2008.
- [88] O. Younes-Metzler, J. Svagin, S. Jensen, C. H. Christensen, O. Hansen, and U. Quaaed, "Microfabricated high-temperature reactor for catalytic partial oxidation of methane," *Applied Catalysis a-General*, vol. 284, pp. 5-10, 2005.
- [89] A. J. Santis-Alvarez, M. Nabavi, N. Hild, D. Poulidakos, and W. J. Stark, "A fast hybrid start-up process for thermally self-sustained catalytic n-butane reforming in micro-SOFC power plants," *Energy & Environmental Science*, vol. 4, pp. 3041-3050, 2011.
- [90] N. Hotz, M. Stutz, S. Loher, W. J. Stark, and D. Poulidakos, "Syngas production from butane using a flame-made Rh/Ce_{0.5}Zr_{0.5}O₂ catalyst," *Applied Catalysis B: Environmental*, vol. 73, pp. 336-344, 2007.
- [91] R. P. O'Connor, E. J. Klein, and L. D. Schmidt, "High yields of synthesis gas by millisecond partial oxidation of higher hydrocarbons," *Catalysis Letters*, vol. 70, pp. 99-107, 2000.
- [92] J. Bassil, A. AlBarazi, P. Da Costa, and M. Boutros, "Catalytic combustion of methane over mesoporous silica supported palladium," *Catalysis Today*, vol. 176, pp. 36-40, 2011.
- [93] A. Bieberle-Hütter, D. Beckel, A. Infortuna, U. P. Muecke, J. L. M. Rupp, L. J. Gauckler, S. Rey-Mermet, P. Murali, N. R. Bieri, N. Hotz, M. J. Stutz, D. Poulidakos, P. Heeb, P. Müller, A. Bernard, R. Gmür, and T. Hocker, "A micro-solid oxide fuel cell system as battery replacement," *Journal of Power Sources*, vol. 177, pp. 123-130, 2008.
- [94] G. Vesper, M. Ziauddin, and L. D. Schmidt, "Ignition in alkane oxidation on noble-metal catalysts," *Catalysis Today*, vol. 47, pp. 219-228, 1999.
- [95] K. H. Shen, Y. Li, G. J. Liu, Y. Li, and X. A. Zhang, "Synthesis and photolytic properties of 1,5-di-N,N'-dialkylaminoanthraquinones containing acryloyl groups," *Progress in Organic Coatings*, vol. 76, pp. 125-130, 2013.
- [96] R. Strobel, J. D. Grunwaldt, A. Camenzind, S. E. Pratsinis, and A. Baiker, "Flame-made alumina supported Pd-Pt nanoparticles: Structural properties and catalytic behavior in methane combustion," *Catalysis Letters*, vol. 104, pp. 9-16, 2005.
- [97] J. L. Zhao, Y. Lv, H. J. Ren, W. Sun, Q. Liu, Y. L. Fu, and L. Y. Wang, "Synthesis, spectral properties of cyanine dyes-beta-cyclodextrin

- and their application as the supramolecular host with spectroscopic probe," *Dyes and Pigments*, vol. 96, pp. 180-188, 2013.
- [98] I. Aartun, T. Gjervan, H. Venvik, O. Gorke, P. Pfeifer, M. Fathi, A. Holmen, and K. Schubert, "Catalytic conversion of propane to hydrogen in microstructured reactors," *Chemical Engineering Journal*, vol. 101, pp. 93-99, 2004.
- [99] I. Aartun, H. J. Venvik, A. Holmen, P. Pfeifer, O. Gorke, and K. Schubert, "Temperature profiles and residence time effects during catalytic partial oxidation and oxidative steam reforming of propane in metallic microchannel reactors," *Catalysis Today*, vol. 110, pp. 98-107, 2005.
- [100] T. Gjervan, H. J. Venvik, I. Aartun, A. Holmen, O. Gorke, P. Pfeifer, and K. Schubert, "Hydrogen production from propane through partial oxidation and autothermal reforming in microstructured reactors.," *Abstracts of Papers of the American Chemical Society*, vol. 225, pp. U866-U866, 2003.
- [101] J. Liu, X. Lu, Z. Xin, and C. L. Zhou, "Synthesis and Surface Properties of Low Surface Free Energy Silane-Functional Polybenzoxazine Films," *Langmuir : the ACS journal of surfaces and colloids*, vol. 29, pp. 411-416, 2013.
- [102] B. L. Liu, Y. X. Wang, G. P. Li, and R. J. Tao, "Synthesis, crystal structures, and magnetic properties of two heterobinuclear complexes with a dissymmetrical oxamidate ligand," *Russian Journal of Coordination Chemistry*, vol. 39, pp. 119-125, 2013.
- [103] P. Pantu, and G. R. Gavalas, "Methane partial oxidation on Pt/CeO₂ and Pt/Al₂O₃ catalysts," *Applied Catalysis a-General*, vol. 223, pp. 253-260, 2002.
- [104] J. J. Zhu, J. G. van Ommen, A. Knoester, and L. Lefferts, "Effect of surface composition of yttrium-stabilized zirconia on partial oxidation of methane to synthesis gas," *Journal of Catalysis*, vol. 230, pp. 291-300, 2005.
- [105] C. Wen, Y. Liu, Y. Guo, Y. Q. Wang, and G. Z. Lu, "Strategy to eliminate catalyst hot-spots in the partial oxidation of methane: enhancing its activity for direct hydrogen production by reducing the reactivity of lattice oxygen," *Chemical Communications*, vol. 46, pp. 880-882, 2010.
- [106] W. Wang, S. M. Stagg-Williams, F. B. Noronha, L. V. Mattos, and F. B. Passos, "Partial oxidation and combined reforming of methane on Ce-promoted catalysts.," *Abstracts of Papers of the American Chemical Society*, vol. 227, pp. U1077-U1077, 2004.
- [107] A. M. Sukeshini, B. Habibzadeh, B. P. Becker, C. A. Stoltz, B. W. Eichhorn, and G. S. Jackson, "Electrochemical oxidation of H₂, CO,

- and CO/H₂ mixtures on patterned Ni anodes on YSZ electrolytes," *Journal of the Electrochemical Society*, vol. 153, pp. A705-A715, 2006.
- [108] J. D. Grunwaldt, S. Hannemann, C. G. Schroer, and A. Baiker, "2D-mapping of the catalyst structure inside a catalytic microreactor at work: Partial oxidation of methane over Rh/Al₂O₃," *Journal of Physical Chemistry B*, vol. 110, pp. 8674-8680, 2006.
- [109] S. Hannemann, J. D. Grunwaldt, P. Lienemann, D. Gunther, F. Krumeich, S. E. Pratsinis, and A. Baiker, "Combination of flame synthesis and high-throughput experimentation: The preparation of alumina-supported noble metal particles and their application in the partial oxidation of methane," *Applied Catalysis a-General*, vol. 316, pp. 226-239, 2007.
- [110] S. Eriksson, S. Rojas, M. Boutonnet, and J. L. G. Fierro, "Effect of Ce-doping on Rh/ZrO₂ catalysts for partial oxidation of methane," *Applied Catalysis a-General*, vol. 326, pp. 8-16, 2007.
- [111] G. N. Vayssilov, Y. Lykhach, A. Migani, T. Staudt, G. P. Petrova, N. Tsud, T. Skala, A. Bruix, F. Illas, K. C. Prince, V. Matolin, K. M. Neyman, and J. Libuda, "Support nanostructure boosts oxygen transfer to catalytically active platinum nanoparticles," *Nature Materials*, vol. 10, pp. 310-315, 2011.
- [112] H. Yoshida, Y. Yazawa, and T. Hattori, "Effects of support and additive on oxidation state and activity of Pt catalyst in propane combustion," *Catalysis Today*, vol. 87, pp. 19-28, 2003.
- [113] W. J. Stark, J. D. Grunwaldt, M. Maciejewski, S. E. Pratsinis, and A. Baiker, "Flame-made Pt/ceria/zirconia for low-temperature oxygen exchange," *Chemistry of Materials*, vol. 17, pp. 3352-3358, 2005.
- [114] A. Trovarelli, M. Boaro, E. Rocchini, C. de Leitenburg, and G. Dolcetti, "Some recent developments in the characterization of ceria-based catalysts," *Journal of Alloys and Compounds*, vol. 323, pp. 584-591, 2001.
- [115] P. Fornasiero, J. Kaspar, V. Sergo, and M. Graziani, "Redox behavior of high-surface-area Rh-, Pt-, and Pd-loaded Ce_{0.5}Zr_{0.5}O₂ mixed oxide," *Journal of Catalysis*, vol. 182, pp. 56-69, 1999.
- [116] E. Ruckenstein, and H. Y. Wang, "Effect of support on partial oxidation of methane to synthesis gas over supported rhodium catalysts," *Journal of Catalysis*, vol. 187, pp. 151-159, 1999.
- [117] M. D. Salazar-Villalpando, D. A. Berry, and A. Cugini, "Role of lattice oxygen in the partial oxidation of methane over Rh/zirconia-doped ceria. Isotopic studies," *International Journal of Hydrogen Energy*, vol. 35, pp. 1998-2003, 2010.
- [118] K. Otsuka, Y. Wang, E. Sunada, and I. Yamanaka, "Direct partial oxidation of methane to synthesis gas by cerium oxide," *Journal of Catalysis*, vol. 175, pp. 152-160, 1998.

- [119] P. Pantu, K. Kim, and G. R. Gavalas, "Methane partial oxidation on Pt/CeO₂-ZrO₂ in the absence of gaseous oxygen," *Applied Catalysis a-General*, vol. 193, pp. 203-214, 2000.
- [120] B. C. Michael, A. Donazzi, and L. D. Schmidt, "Effects of H₂O and CO₂ addition in catalytic partial oxidation of methane on Rh," *Journal of Catalysis*, vol. 265, pp. 117-129, 2009.
- [121] J. P. Breen, R. Burch, and D. Tibiletti, "The effect of preparation variables on Pt and Rh/Ce_xZr_{1-x}O₂ water gas shift catalysts," *Catalysis in Application*, vol., pp. 227-232, 2003.
- [122] B. I. Whittington, C. J. Jiang, and D. L. Trimm, "Vehicle Exhaust Catalysis .1. The Relative Importance of Catalytic-Oxidation, Steam Reforming and Water-Gas Shift Reactions," *Catalysis Today*, vol. 26, pp. 41-45, 1995.
- [123] M. H. Halabi, M. H. J. M. de Croon, J. van der Schaaf, P. D. Cobden, and J. C. Schouten, "Low temperature catalytic methane steam reforming over ceria-zirconia supported rhodium," *Applied Catalysis a-General*, vol. 389, pp. 68-79, 2010.
- [124] D. A. J. M. Lighthart, R. A. van Santen, and E. J. M. Hensen, "Influence of particle size on the activity and stability in steam methane reforming of supported Rh nanoparticles," *Journal of Catalysis*, vol. 280, pp. 206-220, 2011.
- [125] K. Kusakabe, K. I. Sotowa, T. Eda, and Y. Iwamoto, "Methane steam reforming over Ce-ZrO₂-supported noble metal catalysts at low temperature," *Fuel Processing Technology*, vol. 86, pp. 319-326, 2004.
- [126] N. Laosiripojana, and S. Assabumrungrat, "Catalytic dry reforming of methane over high surface area ceria," *Applied Catalysis B-Environmental*, vol. 60, pp. 107-116, 2005.
- [127] S. Damyanova, B. Pawelec, K. Arishtirova, M. V. M. Huerta, and J. L. G. Fierro, "The effect of CeO₂ on the surface and catalytic properties of Pt/CeO₂-ZrO₂ catalysts for methane dry reforming," *Applied Catalysis B-Environmental*, vol. 89, pp. 149-159, 2009.
- [128] M. Fathi, E. Bjorgum, T. Viig, and O. A. Rokstad, "Partial oxidation of methane to synthesis gas: Elimination of gas phase oxygen," *Catalysis Today*, vol. 63, pp. 489-497, 2000.
- [129] S. Boulloussa-Eiras, T. J. Zhao, D. Chen, and A. Holmen, "Effect of the preparation methods and alumina nanoparticles on the catalytic performance of Rh/Zr_xCe_{1-x}O₂-Al₂O₃ in methane partial oxidation," *Catalysis Today*, vol. 171, pp. 104-115, 2011.
- [130] S. Eriksson, M. Wolf, A. Schneider, J. Mantzaras, F. Raimondi, M. Boutonnet, and S. Jaras, "Fuel-rich catalytic combustion of methane in zero emissions power generation processes," *Catalysis Today*, vol. 117, pp. 447-453, 2006.

- [131] M. D. Salazar-Villalpando, D. A. Berry, and T. H. Gardner, "Partial oxidation of methane over Rh/supported-ceria catalysts: Effect of catalyst reducibility and redox cycles," *International Journal of Hydrogen Energy*, vol. 33, pp. 2695-2703, 2008.
- [132] R. Strobel, A. Baiker, and S. E. Pratsinis, "Aerosol flame synthesis of catalysts," *Advanced Powder Technology*, vol. 17, pp. 457-480, 2006.
- [133] W. J. Stark, and S. E. Pratsinis, "Aerosol flame reactors for manufacture of nanoparticles," *Powder Technology*, vol. 126, pp. 103-108, 2002.
- [134] L. Madler, H. K. Kammler, R. Mueller, and S. E. Pratsinis, "Controlled synthesis of nanostructured particles by flame spray pyrolysis," *Journal of Aerosol Science*, vol. 33, pp. 369-389, 2002.
- [135] R. W. Cheary, and A. A. Coelho, "Axial divergence in a conventional X-ray powder diffractometer. I. Theoretical foundations," *Journal of Applied Crystallography*, vol. 31, pp. 851-861, 1998.
- [136] R. Buchel, R. Strobel, A. Baiker, and S. E. Pratsinis, "Effect of the Proximity of Pt to Ce or Ba in Pt/Ba/CeO₂ Catalysts on NO_x Storage-Reduction Performance," *Topics in Catalysis*, vol. 52, pp. 1709-1712, 2009.
- [137] X. Wang, and R. J. Gorte, "A study of steam reforming of hydrocarbon fuels on Pd/ceria," *Applied Catalysis a-General*, vol. 224, pp. 209-218, 2002.
- [138] W. S. Dong, K. W. Jun, H. S. Roh, Z. W. Liu, and S. E. Park, "Comparative study on partial oxidation of methane over Ni/ZrO₂, Ni/CeO₂ and Ni/Ce-ZrO₂ catalysts," *Catalysis Letters*, vol. 78, pp. 215-222, 2002.
- [139] S. Eriksson, M. Nilsson, M. Boutonnet, and S. Jaras, "Partial oxidation of methane over rhodium catalysts for power generation applications," *Catalysis Today*, vol. 100, pp. 447-451, 2005.
- [140] R. Buchel, S. E. Pratsinis, and A. Baiker, "Mono- and bimetallic Rh and Pt NSR-catalysts prepared by controlled deposition of noble metals on support or storage component," *Applied Catalysis B-Environmental*, vol. 113, pp. 160-171, 2012.
- [141] D. Z. Wang, O. Dewaele, A. M. DeGroot, and G. F. Froment, "Reaction mechanism and role of the support in the partial oxidation of methane on Rh/Al₂O₃," *Journal of Catalysis*, vol. 159, pp. 418-426, 1996.
- [142] P. P. Silva, F. A. Silva, H. P. Souza, A. G. Lobo, L. V. Mattos, F. B. Noronha, and C. E. Hori, "Partial oxidation of methane using Pt/CeZrO₂/Al₂O₃ catalysts - effect of preparation methods," *Catalysis Today*, vol. 101, pp. 31-37, 2005.

- [143] J. H. Lee, and D. L. Trimm, "Catalytic Combustion of Methane," *Fuel Processing Technology*, vol. 42, pp. 339-359, 1995.
- [144] D. Ciuparu, M. R. Lyubovsky, E. Altman, L. D. Pfefferle, and A. Datye, "Catalytic combustion of methane over palladium-based catalysts," *Catalysis Reviews-Science and Engineering*, vol. 44, pp. 593-649, 2002.
- [145] K. Eguchi, and H. Arai, "Recent advances in high temperature catalytic combustion," *Catalysis Today*, vol. 29, pp. 379-386, 1996.
- [146] A. J. Santis-Alvarez, M. Nabavi, B. Jiang, T. Maeder, P. Murali, and D. Poulikakos, "A nanoparticle bed micro-reactor with high syngas yield for moderate temperature micro-scale SOFC power plants," *Chemical Engineering Science*, vol. 84, pp. 469-478, 2012.
- [147] R. B. Anderson, K. C. Stein, J. J. Feenan, and L. J. E. Hofer, "Catalytic Oxidation of Methane," *Industrial and Engineering Chemistry*, vol. 53, pp. 809-812, 1961.
- [148] R. Strobel, S. E. Pratsinis, and A. Baiker, "Flame-made Pd/La₂O₃/Al₂O₃ nanoparticles: thermal stability and catalytic behavior in methane combustion," *Journal of Materials Chemistry*, vol. 15, pp. 605-610, 2005.
- [149] N. van Vegten, M. Maciejewski, F. Krumeich, and A. Baiker, "Structural properties, redox behaviour and methane combustion activity of differently supported flame-made Pd catalysts," *Applied Catalysis B-Environmental*, vol. 93, pp. 38-49, 2009.
- [150] S. Colussi, A. Trovarelli, E. Vesselli, A. Baraldi, G. Comelli, G. Groppi, and J. Llorca, "Structure and morphology of Pd/Al₂O₃ and Pd/CeO₂/Al₂O₃ combustion catalysts in Pd-PdO transformation hysteresis," *Applied Catalysis a-General*, vol. 390, pp. 1-10, 2010.
- [151] R. X. Zhou, B. Zhao, and B. H. Yue, "Effects of CeO₂-ZrO₂ present in Pd/Al₂O₃ catalysts on the redox behavior of PdO_x and their combustion activity," *Applied Surface Science*, vol. 254, pp. 4701-4707, 2008.
- [152] A. Trovarelli, "Catalytic properties of ceria and CeO₂-containing materials," *Catalysis Reviews-Science and Engineering*, vol. 38, pp. 439-520, 1996.
- [153] F. Arosio, S. Colussi, A. Trovarelli, and G. Groppi, "Effect of alternate CH₄-reducing/lean combustion treatments on the reactivity of fresh and S-poisoned Pd/CeO₂/Al₂O₃ catalysts," *Applied Catalysis B-Environmental*, vol. 80, pp. 335-342, 2008.
- [154] F. Arosio, S. Colussi, G. Groppi, and A. Trovarelli, "Regeneration of S-poisoned Pd/Al₂O₃ and Pd/CeO₂/Al₂O₃ catalysts for the combustion of methane," *Topics in Catalysis*, vol. 42-43, pp. 405-408, 2007.

- [155] S. Fouladvand, S. Schernich, J. Libuda, H. Gronbeck, T. Pingel, E. Olsson, M. Skoglundh, and P. Carlsson, "Methane oxidation over Pd supported on ceria–alumina under rich/lean cycling conditions," *Topics in Catalysis*, vol. DOI 10.1007/s11244-013-9988-2, pp., 2013.
- [156] S. Colussi, A. Trovarelli, G. Groppi, and J. Llorca, "The effect of CeO₂ on the dynamics of Pd-PdO transformation over Pd/Al₂O₃ combustion catalysts," *Catalysis Communications*, vol. 8, pp. 1263-1266, 2007.
- [157] R. Buchel, R. Strobel, F. Krumeich, A. Baiker, and S. E. Pratsinis, "Influence of Pt location on BaCO₃ or Al₂O₃ during NO_x storage reduction," *Journal of Catalysis*, vol. 261, pp. 201-207, 2009.
- [158] R. Strobel, L. Madler, M. Piacentini, M. Maciejewski, A. Baiker, and S. E. Pratsinis, "Two-nozzle flame synthesis of Pt/Ba/Al₂O₃ for NO_x storage," *Chemistry of Materials*, vol. 18, pp. 2532-2537, 2006.
- [159] R. Büchel, R. Strobel, A. Baiker, and S. E. Pratsinis, "Effect of the Proximity of Pt to Ce or Ba in Pt/Ba/CeO₂ Catalysts on NO_x Storage–Reduction Performance.," *Topics in Catalysis*, vol. 52, pp. 1709-1712, 2009.
- [160] C. Bozo, N. Guilhaume, E. Garbowski, and M. Primet, "Combustion of methane on CeO₂-ZrO₂ based catalysts," *Catalysis Today*, vol. 59, pp. 33-45, 2000.
- [161] A. K. Datye, J. Bravo, T. R. Nelson, P. Atanasova, M. Lyubovsky, and L. Pfefferle, "Catalyst microstructure and methane oxidation reactivity during the Pd ↔ PdO transformation on alumina supports," *Applied Catalysis a-General*, vol. 198, pp. 179-196, 2000.
- [162] W. R. Schwartz, and L. D. Pfefferle, "Combustion of Methane over Palladium-Based Catalysts: Support Interactions," *Journal of Physical Chemistry C*, vol. 116, pp. 8571-8578, 2012.
- [163] K. Narui, H. Yata, K. Furuta, A. Nishida, Y. Kohtoku, and T. Matsuzaki, "Effects of addition of Pt to PdO/Al₂O₃ catalyst on catalytic activity for methane combustion and TEM observations of supported particles," *Applied Catalysis a-General*, vol. 179, pp. 165-173, 1999.
- [164] X. N. Guo, G. J. Zhi, X. Y. Yan, G. Q. Jin, X. Y. Guo, and P. Brault, "Methane combustion over Pd/ZrO₂/SiC, Pd/CeO₂/SiC, and Pd/Zr_{0.5}Ce_{0.5}O₂/SiC catalysts," *Catalysis Communications*, vol. 12, pp. 870-874, 2011.
- [165] T. R. Baldwin, and R. Burch, "Catalytic Combustion of Methane over Supported Palladium Catalysts .1. Alumina Supported Catalysts," *Applied Catalysis*, vol. 66, pp. 337-358, 1990.
- [166] W. S. Epling, and G. B. Hoflund, "Catalytic oxidation of methane over ZrO₂-supported Pd catalysts," *Journal of Catalysis*, vol. 182, pp. 5-12, 1999.

- [167] Y. Yazawa, H. Yoshida, N. Takagi, S. Komai, A. Satsuma, and T. Hattori, "Acid strength of support materials as a factor controlling oxidation state of palladium catalyst for propane combustion," *Journal of Catalysis*, vol. 187, pp. 15-23, 1999.
- [168] T. V. Choudhary, S. Banerjee, and V. R. Choudhary, "Catalysts for combustion of methane and lower alkanes," *Applied Catalysis a-General*, vol. 234, pp. 1-23, 2002.
- [169] C. F. Cullis, D. L. Trimm, and T. G. Nevell, "Role of Catalyst Support in Oxidation of Methane over Palladium," *Journal of the Chemical Society-Faraday Transactions I*, vol. 68, pp. 1406-&, 1972.
- [170] C. F. Cullis, and B. M. Willatt, "The Inhibition of Hydrocarbon Oxidation over Supported Precious Metal-Catalysts," *Journal of Catalysis*, vol. 86, pp. 187-200, 1984.
- [171] R. Burch, F. J. Urbano, and P. K. Loader, "Methane Combustion over Palladium Catalysts - the Effect of Carbon-Dioxide and Water on Activity," *Applied Catalysis a-General*, vol. 123, pp. 173-184, 1995.

List of Publications

Journal Publications

7. **A. J. Santis-Alvarez**, R. Büchel, P. Rüdlinger, F. Krumeich, and D. Poulidakos, "The effect of deposition locality of flame-made Pd on a mixed $\text{Al}_2\text{O}_3\text{-Ce}_{0.5}\text{Zr}_{0.5}\text{O}_2$ support on methane combustion," *submitted for publication*, 2013.
6. **A. J. Santis-Alvarez**, R. Büchel, N. Hild, W. Stark, and D. Poulidakos, "Comparison of flame-made rhodium on Al_2O_3 or $\text{Ce}_{0.5}\text{Zr}_{0.5}\text{O}_2$ supports for the partial oxidation of methane," *submitted for publication*, 2013.
5. A. Bieberle-Hütter, **A. J. Santis-Alvarez**, B. Jiang, P. Heeb, T. Maeder, M. Nabavi, D. Poulidakos, P. Niedermann, A. Dommann, P. Muralt, A. Bernard, and L. J. Gauckler, "Syngas generation from n-butane with an integrated MEMS assembly for gas processing in micro-solid oxide fuel cell systems," *Lab on a Chip*, vol. 12, pp. 4894-4902, 2012.
4. B. Jiang, P. Muralt, P. Heeb, **A. J. Santis-Alvarez**, M. Nabavi, D. Poulidakos, P. Niedermann, and T. Maeder, "A micro heater platform with fluid channels for testing micro-solid oxide fuel cell components," *Sensors and Actuators B: Chemical*, vol. 175, pp. 218-224, 2012.
3. **A. J. Santis-Alvarez**, M. Nabavi, B. Jiang, T. Maeder, P. Muralt, and D. Poulidakos, "A nanoparticle bed micro-reactor with high syngas yield for moderate temperature micro-scale SOFC power plants," *Chemical Engineering Science*, vol. 84, pp. 469-478, 2012.
2. M. Nabavi, Y. Yan, **A. J. Santis-Alvarez**, and D. Poulidakos, "A spatially-resolved temperature-dependent model for butane reforming over rhodium catalyst," *International Journal of Hydrogen Energy*, vol. 37, pp. 9067-9075, 2012.
1. **A. J. Santis-Alvarez**, M. Nabavi, N. Hild, D. Poulidakos, and W. J. Stark, "A fast hybrid start-up process for thermally self-sustained catalytic n-

butane reforming in micro-SOFC power plants," *Energy & Environmental Science*, vol. 4, pp. 3041-3050, 2011.

Conference Publications

5. B. Jiang, **A. J. Santis-Alvarez**, P. Mural, D. Poulikakos, and T. Maeder, "Development of low temperature co-fired ceramic fuel processor for micro-scale solid oxide fuel cell system," in *9th European Congress of Chemical Engineering*, 2013.
4. B. Jiang, P. Mural, **A. J. Santis-Alvarez**, M. Nabavi, D. Poulikakos, and T. Maeder, "The development of fuel processor platform for micro-scale solid oxide fuel cells," in *The Energy & Materials Research Conference*, 2012.
3. B. Jiang, P. Mural, T. Maeder, P. Heeb, **A. J. Santis-Alvarez**, M. Nabavi, D. Poulikakos, and P. Niedermann, "Design, Fabrication and Characterization of a Gas Processing Unit Testing Platform for Micro-Solid Oxide Fuel Cells," *Procedia Engineering*, vol. 25, pp. 811–814, 2011.
2. **A. J. Santis-Alvarez**, M. Nabavi, and D. Poulikakos, "Self-sustained partial oxidation of n-butane triggered by a hybrid start-up process for micro-SOFC devices," *ASME International Mechanical Engineering Congress and Exposition*, Denver, Colorado, USA, 2011.
1. E. Maier, W. Haas, **A. J. Santis-Alvarez**, T. Rath, F. Hofer, F. Stelzer, and G. Trimmel, "Polymer - CuInS₂ hybrid solar cells obtained by an in-situ formation route," *35th IEEE Photovoltaic Specialists Conference*, pp. 3365-3368, 2010.

Curriculum Vitae

Name: **SANTIS ALVAREZ, Alejandro Javier**

Date of Birth: February 16th, 1983

Place of Birth: Guatemala City

Nationality: Guatemala

04/2010 - 06/2013 **Doctoral Student** at the Laboratory of Thermodynamics in Emerging Technology, Institute of Energy Technology, Department of Mechanical and Process Engineering, **ETH Zurich**, Switzerland
Supervisor: Prof. Dimos Poulikakos

11/2008 - 08/2009 **Diploma Thesis in Technical Chemistry**
Institute for Chemistry and Technology of Materials,
Graz University of Technology, Austria

10/2002 - 08/2009 **University Studies in Technical Chemistry**
Technical Chemistry,
Graduated with honours,
Graz University of Technology, Austria

01/1987 - 09/2001 Kindergarten to **Austrian Matura** (Austrian High School diploma)
Austrian School, Guatemala

